

Investigation of microwave heating scenarios in the magnetically confined low-temperature plasma of the stellarator TJ-K

Von der Fakultät Mathematik und Physik der Universität Stuttgart
zur Erlangung der Würde eines Doktors der
Naturwissenschaftlichen (Dr. rer. nat) genehmigte Abhandlung

Vorgelegt von

Alf Köhn

aus Preetz

Hauptberichter:

Prof. Dr. U. Stroth

Mitberichter:

Prof. Dr. M. Dressel

Tag der mündlichen Prüfung:

20.05.2010

Institut für Plasmaforschung der Universität Stuttgart

2010

*Savoir s'étonner à propos de tout est le
premier pas fait sur la route de la découverte.*
– Louis Pasteur

Zusammenfassung

Die Erzeugung und Heizung von Plasmen mittels Mikrowellen stellt eine weit verbreitete Methode dar. Dieses gilt sowohl für Hochtemperatur-Fusionsplasmen als auch für Niedertemperaturplasmen. In Fusionsplasmen ist die Absorption der Mikrowelle gut verstanden: Die Welle koppelt resonant an die Zyklotronbewegung der Elektronen um die Magnetfeldlinien an. Die Effizienz dieser Heizung hängt stark von der Temperatur der Elektronen ab. In Niedertemperaturplasmen haben die Elektronen Temperaturen im Bereich von 1 – 10 eV. Bei diesen, im Vergleich zu Fusionsplasmen, niedrigen Temperaturen, spielt die Zyklotronresonanz nur für die Zündung eine Rolle. Für die Heizung des Plasmas müssen daher andere Prozesse genutzt werden. Eine Möglichkeit stellt dabei die Heizung durch Elektron-Bernstein-Wellen dar. Diese müssen durch Modenkonzversionsprozesse im Plasma angeregt werden, da sie im Vakuum nicht propagieren können. Eine weitere Möglichkeit ist die Heizung an der oberen Hybridresonanz.

Bei dem Stellarator TJ-K handelt es sich um ein Niedertemperaturplasmaexperiment, an welchem Mikrowellenheizung bei zwei verschiedenen Frequenzen durchgeführt werden kann: bei 2,45 GHz und in dem Bereich um 8 GHz. Die vorliegende Arbeit untersucht die möglichen Heizszenarien in TJ-K. Um die Wechselwirkung der Mikrowelle mit dem Plasma numerisch studieren zu können, wurde der Wellencode IPF-FDMC entwickelt. Damit konnte der Konversionsprozess einer elektromagnetischen Welle in die elektrostatische Elektron-Bernstein-Welle genau untersucht und die Konversionseffizienz für verschiedene, fusionsrelevante Experimente in Europa optimiert werden. Sowohl die experimentellen also auch die numerischen Untersuchungen zeigen, dass in TJ-K der Hauptanteil der Mikrowellenleistung an der oberen Hybridresonanz absorbiert wird. Zum Verständnis des hohen Absorptionskoeffizienten ist die reflektierende Wand des Vakuumgefäßes von entscheidender Bedeutung. In der aktuellen Konfiguration von TJ-K spielt die Heizung durch Bernstein-Wellen keine entscheidene Rolle. Im Verlaufe dieser Untersuchungen wurde ein neuer Operationsbereich entdeckt, in welchem es möglich ist, Plasmen effizient zu heizen, obwohl sich keine Resonanz für die eingestrahelte Mikrowelle im Plasma befindet.

Abstract

The generation and heating of plasmas by means of microwaves is a widely-used method. This is the case for high-temperature fusion plasmas as well as for low-temperature plasmas. In fusion plasmas, the absorption of the microwave is well understood: The wave couples resonantly to the cyclotron motion of electrons around the magnetic field lines. The efficiency of the heating depends strongly on the temperature of the electrons. In low-temperature plasmas, the electrons have temperatures in the range of 1 – 10 eV. At these temperatures, which are low compared to those in fusion plasmas, the cyclotron resonance only plays a role for the plasma breakdown. Hence, other mechanisms must be used for plasma heating. One possibility is heating by electron Bernstein waves. They must be excited by mode conversion processes in the plasma, because they cannot propagate in vacuum. Another candidate is heating at the upper-hybrid resonance.

The stellarator TJ-K is a low-temperature experiment at which microwave heating can be carried out at two different frequencies: at 2.45 GHz and in the range around 8 GHz. The thesis presented here, investigates the possible heating scenarios in TJ-K. To numerically study the interaction of the microwave with the plasma, the full-wave code IPF-FDMC was developed. With this code, the efficiency of the conversion process of an electromagnetic wave into the electrostatic electron Bernstein wave could be investigated in detail for different fusion-relevant experiments in Europe. Both the experimental and the numerical results show that, in TJ-K, most of the microwave power is absorbed at the upper-hybrid resonance. To understand the high absorption coefficient, the reflecting vacuum vessel walls are of vital importance. In the present experimental configuration of TJ-K, heating by Bernstein waves does not play an important role. In the course of these investigations, a new operational regime was discovered in which it is possible to efficiently heat plasmas, albeit there is no resonance for the injected microwave in the plasma.

Contents

1	Introduction	11
2	Waves in plasmas	13
2.1	Introduction	13
2.2	Waves in cold plasmas	13
2.2.1	Propagation parallel to \mathbf{B}_0	17
2.2.2	Propagation perpendicular to \mathbf{B}_0	18
2.2.3	Effect of increasing plasma temperature	19
2.3	Bernstein waves	20
2.4	Excitation of EBW	23
2.4.1	O–X–B mode conversion	23
2.4.2	Direct X–B conversion	27
3	The full-wave code IPF-FDMC	31
3.1	Ray tracing	31
3.2	Principles of the full-wave code IPF-FDMC	32
3.2.1	The Yee algorithm	32
3.2.2	The plasma response	35
3.2.3	The source	36
3.2.4	Boundary conditions	36
3.2.5	The code IPF-FDMC	37
3.3	Application of the code IPF-FDMC	39
3.3.1	1D simulations: O–X mode conversion	39
3.3.2	1D simulations: X–B mode conversion	42
3.3.3	Deterioration of the conversion efficiency in 2D	45
3.3.4	Simulations of the O–X–B mode conversion in 2D	48
3.4	Summary	51
4	The stellarator TJ-K	53
4.1	TJ-K	53
4.1.1	Geometric configuration	53
4.1.2	Magnetic configuration	54
4.2	Plasma heating	56

4.2.1	2.45 GHz microwave system	56
4.2.2	8 GHz microwave system	57
4.3	Diagnostics	59
4.3.1	Langmuir probes	59
4.3.2	Monopole antennas	62
4.3.3	Microwave interferometry	63
4.3.4	Laser-induced fluorescence	64
5	Heating plasmas at low magnetic field	65
5.1	Plasma breakdown	65
5.2	Equilibrium profiles	67
5.3	Achieved plasma parameters	71
5.4	Estimation of the heating efficiency	75
5.5	Full-wave simulations	78
5.5.1	Simulations in the poloidal plane	78
5.5.2	Simulations in the toroidal plane	82
5.6	Measurement of the wave electric field of the incident microwave	84
5.7	Fast power modulation studies	85
5.8	Parametric instabilities	85
5.8.1	Measurements in TJ-K	87
5.9	Summary	93
6	Heating plasmas at high magnetic field	97
6.1	Resonant heating	97
6.1.1	Plasma breakdown	97
6.1.2	Equilibrium profiles	98
6.1.3	Scaling of plasma parameters	101
6.1.4	Estimation of the heating efficiency	104
6.1.5	Full-wave simulations	106
6.1.6	Summary	108
6.2	Non-resonant heating	108
6.2.1	Plasma breakdown	109
6.2.2	Scaling of plasma parameters	110
6.2.3	Power deposition studies	112
6.2.4	Toroidal currents	113
6.2.5	Discussion of possible heating mechanisms	116
7	Summary	119
A	The 8 GHz microwave system	123
A.1	The different operational modes	123
A.2	The vacuum window	123
	Literaturverzeichnis	127

Danksagung	138
Curriculum Vitae	140
Eidesstattliche Versicherung	143

Chapter 1

Introduction

First experiments to generate and heat plasmas by means of microwaves date back to the year 1951 [1]. Since then microwave heating has become a standard technique to heat plasmas over a wide range of parameters from high-temperature fusion plasmas with electron temperatures up to 10 keV to low-temperature plasmas around 1 eV. The interaction of microwaves with magnetized plasmas is related to a wide field of physical processes. The properties of propagation, cutoffs and resonances depend on the wave polarization and the angle of incidence with respect to the magnetic field. Furthermore, the intricate phenomenon of mode conversion can occur. Heating of fusion plasmas is well understood [2]: the microwave can propagate perpendicular to the magnetic field up to the cyclotron resonance where it is effectively absorbed by the electrons when the gyro frequency matches the wave frequency. In unmagnetized low-temperature plasmas the wave absorption can be explained by taking electron-neutral collisions into account [3].

High-temperature fusion devices are operated with the goal to achieve nuclear fusion as a source of energy. Two concepts have been proposed to confine the hot plasma in a magnetic field: the tokamak [4] and the stellarator [5]. In a tokamak, the poloidal magnetic field, necessary for confinement, is created by an inductively driven current, whereas in a stellarator the entire magnetic field is created by sophisticatedly shaped field coils. The frequency of the microwave used for plasma heating is chosen to couple to the electron cyclotron resonance frequency defined by the magnetic field of the device. This heating mechanism is referred to as *electron cyclotron resonance heating* (ECRH) and constitutes a vital heating mechanism for fusion plasmas which can also be used to drive significant currents in the plasma, referred to as *electron cyclotron current drive* (ECCD) [6, 7]. The continuous progress in the development of powerful microwave sources at high frequencies has recently resulted in a gyrotron capable of an output power of 1 MW at a frequency of 170 GHz [8]. This development is mandatory for the next-generation tokamaks and stellarators, such as ITER [9] and W7-X [10], both currently under construction.

An important topic of present-day research in high-temperature devices is the heating of so-called *overdense* plasmas, i. e. plasmas where the cyclotron reso-

nance is shielded from the incident microwave by the cutoff layer. The physics of overdense plasmas can also be studied in toroidally confined low-temperature plasmas as the one in the stellarator TJ-K [11, 12] which is operated at *Institut für Plasmaforschung, Universität Stuttgart*. It is dedicated mainly to the research of turbulent transport [13, 14, 15].

In overdense plasmas, the wave can no longer reach the cyclotron resonance and, hence, ECRH cannot take place any longer. A solution to overcome this problem is the excitation of electron Bernstein waves (EBW). For these waves there exists no density cutoff. Furthermore, they are very well absorbed at the cyclotron resonance and its harmonics. The EBW is an electrostatic wave that does not exist in vacuum but can be excited by the electromagnetic waves inside the plasma [16]. The main challenge is their excitation, which involves one or two mode conversion processes that are efficient only in a narrow window of the following parameters: frequency, polarization and angle of incidence. The optimum values for these quantities depend on the plasma discharge parameters. This demands numerical modeling of the process. In order to study the conversion in detail, the full-wave code IPF-FDMC was developed in the frame of this thesis and applied to different experiments in Europe. In addition, the simulations revealed details of the intricate conversion process and allowed the visual representation of its temporal and spatial development.

In magnetized low-temperature plasmas, heating at the cyclotron resonance can be neglected. Nevertheless, microwaves are often used as the heating source in this type of experiment which produces generally overdense plasmas. Again, the EBW is a candidate for the heating process since it is very well absorbed at the cyclotron resonance even at low temperatures. Another candidate is heating at the so-called *upper-hybrid resonance* (UHR). The low-temperature plasma in the stellarator TJ-K can be generated using two different microwave systems: one operates at 2.45 GHz and the other around 8 GHz. In both cases the resulting plasma is overdense. Hence, it is ideally suited for experimental studies of the heating process in an overdense plasma. The present work deals with the experimental investigation of the heating physics supported by numerical studies with the code IPF-FDMC. In the course of this study, a novel heating scheme has been discovered where the microwave is effectively absorbed in the absence of any resonances.

This thesis is organized as follows: in chapter 2, waves in plasmas are described in general and with the EBW in more detail. A comprehensive description of the full-wave code is given in chapter 3. Chapter 4 describes the device TJ-K and the diagnostics attached to it. The generation and heating of plasmas in TJ-K with 2.45 GHz at the corresponding resonant magnetic field is explained in chapter 5. The case of resonant heating with 8 GHz is discussed in chapter 6. This section finally contains the description of the new operational regime, where the plasma is heated non-resonantly at high magnetic field strengths. A summary concludes this thesis.

Chapter 2

Waves in plasmas

2.1 Introduction

The investigation of waves in plasmas is an important research topic since the very beginning of plasma physics. During the First World War, many radio operators were puzzled by a sustained whistle, which they heard from time to time. This whistle was first reported in the literature by Barkhausen in 1919 [17]. Motivated by this phenomenon, Hartree investigated in 1931 the propagation of electromagnetic waves in a diffractive and magnetized medium [18]. Appleton considered in 1932 the wave propagation in the earth's ionosphere [19]. Nevertheless, it took some years to explain the source of the whistling sound in detail [20]: It originates from lightning flashes, which excite waves in the ionosphere. These waves then are guided along the magnetic field lines of the earth between the two magnetic poles. During their propagation they experience dispersion and, hence, a whistling tone is produced. Today, these waves are denoted as *whistler waves*.

A considerable number of textbooks deal with the description of the interaction of electromagnetic waves with plasma. One of the first comprehensive books has been written by Stix in 1962 [21]. In general, one can distinguish between waves in cold and hot plasmas. In the cold plasma approximation, the plasma is described as a fluid. Many types of waves and physical effects can be described with this model, as will be shown in Sec. 2.2. In the hot plasma description, the different species of plasma particles are each described by a distribution function. Some new and important effects will come into play that are not described by the cold plasma approximation. This topic will be addressed in Sec. 2.3.

2.2 Waves in cold plasmas

Electromagnetic waves, which are incident onto a plasma experience dispersion. Depending on their frequency, the waves can give rise to a variety of phenomena, of which the whistler wave, mentioned above, is only one. The reason for this is the

collective behavior of the plasma particles, which can have significant influence on propagating electromagnetic waves. Here, the plasma will be described as a cold fluid, an approximation usually used to describe waves in plasmas.

The zero-order quantities, background magnetic field and density, are taken to be uniform in space and time, whereas the first-order quantities are assumed to vary as $\exp[i(\mathbf{k} \cdot \mathbf{r} - \omega t)]$ with ω the wave angular frequency and \mathbf{k} the wave vector. This leads to the Maxwell equations in the form:

$$\mathbf{k} \times \mathbf{E} = \omega \mathbf{B} \quad (2.1)$$

$$\mathbf{k} \times \mathbf{B} = -\mu_0 \epsilon_0 \omega \mathbf{E} - i\mu_0 \mathbf{J}, \quad (2.2)$$

where \mathbf{J} is the current density in the plasma. Combining Faraday's law of induction (2.1) and Ampère's law (2.2) results in the wave equation

$$\mathbf{k} \times (\mathbf{k} \times \mathbf{E}) + \omega (i\mu_0 \mathbf{J} + \mu_0 \epsilon_0 \omega \mathbf{E}) = 0. \quad (2.3)$$

Rearranging the wave equation, it reads

$$\mathbf{k} \times (\mathbf{k} \times \mathbf{E}) + \frac{\omega^2}{c^2} \left(\mathbf{E} + \frac{i}{\omega \epsilon_0} \mathbf{J} \right) = 0. \quad (2.4)$$

Making use of the dielectric tensor $\boldsymbol{\varepsilon}$, which is defined by $\boldsymbol{\varepsilon} \cdot \mathbf{E} = \mathbf{E} + i/(\epsilon_0 \omega) \mathbf{J}$, leads then to

$$\mathbf{k} \times (\mathbf{k} \times \mathbf{E}) + \frac{\omega^2}{c^2} \boldsymbol{\varepsilon} \cdot \mathbf{E} = 0. \quad (2.5)$$

With the introduction of the refractive index

$$\mathbf{N} = \frac{\mathbf{k}c}{\omega} \quad (2.6)$$

the wave equation can be simplified to the following form:

$$(\mathbf{N} \times \mathbf{N} \times \mathbf{1} + \boldsymbol{\varepsilon}) \cdot \mathbf{E} = 0, \quad (2.7)$$

with $\mathbf{1}$ being the unit matrix. Non-trivial solutions of this equation are obtained by setting the determinant to zero:

$$\det(\mathbf{N} \times \mathbf{N} \times \mathbf{1} + \boldsymbol{\varepsilon}) = 0. \quad (2.8)$$

Equation (2.8) represents the general dispersion relation for waves in an homogenous, anisotropic plasma. To solve this equation, the dielectric tensor $\boldsymbol{\varepsilon}$ must be known.

The dielectric tensor $\boldsymbol{\varepsilon}(\omega, \mathbf{k})$ can be expressed as the sum of the susceptibilities $\boldsymbol{\chi}(\omega, \mathbf{k})$ of the particles α :

$$\boldsymbol{\varepsilon}(\omega, \mathbf{k}) = \mathbf{1} + \sum_{\alpha} \boldsymbol{\chi}_{\alpha}(\omega, \mathbf{k}). \quad (2.9)$$

Ohm's law then gives the connection between the plasma current \mathbf{J} and the electric field \mathbf{E} :

$$\mathbf{J}_\alpha = \boldsymbol{\sigma}_\alpha \cdot \mathbf{E} = -\frac{i\omega}{4\pi} \boldsymbol{\chi}_\alpha \cdot \mathbf{E}, \quad (2.10)$$

with the conductivity $\boldsymbol{\sigma}_\alpha$ of the particles of type α .

The plasma current density represents the response of the particles to the electromagnetic perturbation. It is given as the sum of its components,

$$\mathbf{J} = \sum_\alpha \mathbf{J}_\alpha = \sum_\alpha n_\alpha q_\alpha \mathbf{v}_\alpha, \quad (2.11)$$

with the number density n_α of the particle of type α , the charge q_α and the fluid velocity \mathbf{v}_α .

Hence, the equation of motion of the particles is needed. In an electric and magnetic field the linearized equation of motion reads

$$m_\alpha \frac{\partial}{\partial t} \mathbf{v}_\alpha = q_\alpha (\mathbf{E} + \mathbf{v}_\alpha \times \mathbf{B}_0). \quad (2.12)$$

After Fourier transformation in time, and combining it with Eqs. (2.10) and (2.9), the dielectric tensor can be deduced [22]. The result reads

$$\boldsymbol{\varepsilon} = \begin{pmatrix} S & -iD & 0 \\ iD & S & 0 \\ 0 & 0 & P \end{pmatrix}, \quad (2.13)$$

with the parameters S , D and P , introduced by T. Stix in 1962 [21]. The parameters, S (**sum**), D (**difference**), P (**plasma**), R (**right**) and L (**left**) are also referred to as *Stix parameters*. They are defined as follows:

$$S = \frac{1}{2}(R + L) = 1 - \sum_\alpha \frac{\omega_{p\alpha}^2}{\omega^2 - \omega_{c\alpha}^2} \quad (2.14)$$

$$D = \frac{1}{2}(R - L) = \sum_\alpha \frac{\text{sgn}(q_\alpha) \omega_{c\alpha} \omega_{p\alpha}^2}{\omega(\omega^2 - \omega_{c\alpha}^2)} \quad (2.15)$$

$$P = 1 - \sum_\alpha \frac{\omega_{p\alpha}^2}{\omega^2} \quad (2.16)$$

$$R = S + D = 1 - \sum_\alpha \frac{\omega_{p\alpha}^2}{\omega(\omega + \text{sgn}(q_\alpha) \omega_{c\alpha})} \quad (2.17)$$

$$L = S - D = 1 - \sum_\alpha \frac{\omega_{p\alpha}^2}{\omega(\omega - \text{sgn}(q_\alpha) \omega_{c\alpha})}, \quad (2.18)$$

where $\omega_{p\alpha}$ and $\omega_{c\alpha}$ are the plasma and cyclotron frequency, respectively, of the particle species α .

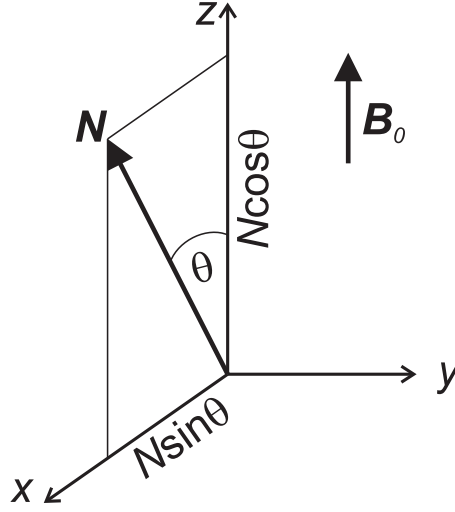


Figure 2.1: Coordinate system used for the description of waves in cold plasmas. The background magnetic field \mathbf{B}_0 is directed parallel to the z -axis and the wave propagation lies in the xz -plane.

Assuming wave propagation to lie in the xz -plane as depicted in Fig. 2.1, and letting θ be the angle between \mathbf{B}_0 and \mathbf{N} , so that $\mathbf{N} = (N \sin \theta, 0, N \cos \theta)$, the wave equation (2.7) becomes

$$\begin{pmatrix} S - N^2 \cos^2 \theta & -iD & N^2 \cos \theta \sin \theta \\ iD & S - N^2 & 0 \\ N^2 \cos \theta \sin \theta & 0 & P - N^2 \sin^2 \theta \end{pmatrix} \begin{pmatrix} E_x \\ E_y \\ E_z \end{pmatrix} = 0. \quad (2.19)$$

The condition, that the determinant of Eq. (2.19) vanishes, leads to the dispersion relation [23]

$$AN^4 - BN^2 + C = 0, \quad (2.20)$$

where the parameters A , B and C read

$$A = S \sin^2 \theta + P \cos^2 \theta \quad (2.21)$$

$$B = RL \sin^2 \theta + PS(1 + \cos^2 \theta) \quad (2.22)$$

$$C = PRL. \quad (2.23)$$

Åstrom [24] and Allis [23] gave the dispersion relation in a different form:

$$\tan^2 \theta = \frac{-P(N^2 - R)(N^2 - L)}{(SN^2 - RL)(N^2 - P)}. \quad (2.24)$$

Distinguished points in a dispersion relation are the cutoffs ($k \rightarrow 0$), where the wave is reflected and the resonances ($k \rightarrow \infty$), where absorption occurs.

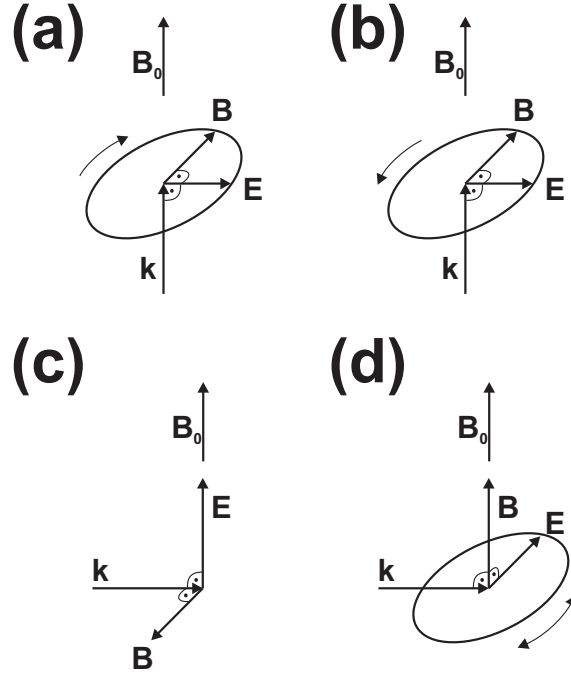


Figure 2.2: Polarization of the so-called principal waves [23]: (a) L-wave, (b) R-wave, (c) O-wave, (d) X-wave.

From Eq. (2.24), the dispersion relations for propagation parallel ($\theta = 0^\circ$) and perpendicular ($\theta = 90^\circ$) to the background magnetic field \mathbf{B}_0 , can be easily obtained:

$$\theta = 0^\circ : \quad P = 0, \quad N^2 = R, \quad N^2 = L \quad (2.25)$$

$$\theta = 90^\circ : \quad N^2 = P, \quad N^2 = RL/S \quad (2.26)$$

2.2.1 Propagation parallel to \mathbf{B}_0

The solutions of Eq. (2.24) for parallel propagation were given in Eq. (2.25). The first solution, $P = 0$, represents the so called *plasma oscillations*, where the plasma particles simply oscillate around their equilibrium position. Since the corresponding group velocity, $v_g = \partial\omega/\partial k = 0$, turns out to be zero, these oscillations do not propagate in the plasma.

The two other solutions are referred to as R- and L-wave, because these waves are circularly polarized in either clockwise (R-wave) or counterclockwise (L-wave) direction. This is illustrated in Fig. 2.2a for the L-wave and in Fig. 2.2b for the R-wave. Hence, these waves can be absorbed by particles that have the same direction of rotation, which means electrons for the R-wave and ions for the L-wave. To be absorbed the frequency of the wave must equal the cyclotron frequency of the particles.

To obtain the cutoffs of the waves, the dispersion relations have to be solved in the limit $k \rightarrow 0$. It turns out that the R-wave has a cutoff at ω_R and the L-wave at

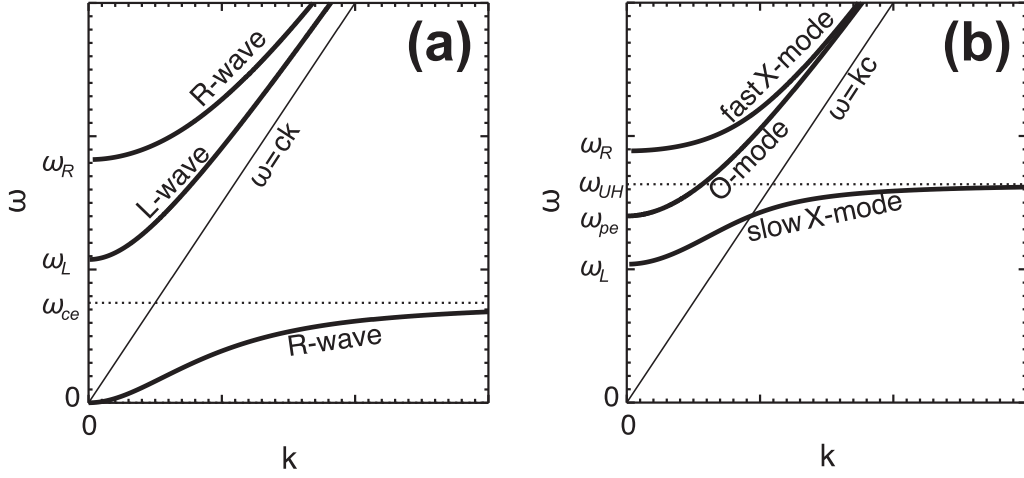


Figure 2.3: Dispersion relation for waves in a cold plasma with (a) $\mathbf{k} \parallel \mathbf{B}_0$ and (b) $\mathbf{k} \perp \mathbf{B}_0$. The resonances, cutoffs and type of waves are labeled in the graphs.

ω_L . Making use of the fact that $\omega_{pe}^2 \gg \omega_{pi}^2$ and $\omega_{ce} \gg \omega_{ci}$, the cutoffs are:

$$\omega_R = \sqrt{\frac{1}{4}\omega_{ce}^2 + \omega_{pe}^2} + \frac{1}{2}\omega_{ce} \quad (2.27)$$

$$\omega_L = \sqrt{\frac{1}{4}\omega_{ce}^2 + \omega_{pe}^2} - \frac{1}{2}\omega_{ce}. \quad (2.28)$$

In Fig. 2.3a, the dispersion relations of both the R- and the L-wave are depicted. Due to $\omega_{ce} \gg \omega_{ci}$, the branch of the L-wave going into resonance at the ion cyclotron frequency ω_{ci} is not given in the graph.

2.2.2 Propagation perpendicular to \mathbf{B}_0

The solutions of the general dispersion relation for perpendicular propagation are given in Eq. (2.26). The first solution describes a wave where the electric field vector is directed parallel to \mathbf{B}_0 . Hence, the wave is not influenced by it. According to Allis [23], it is referred to as O-wave (**ordinary**). It only has a cutoff at the plasma frequency and cannot be absorbed by the plasma in this approximation.

The second solution given in Eq. (2.26) is referred to as X-wave (**extraordinary**). It is extraordinary in the sense that it is elliptically polarized, either clockwise or counterclockwise with respect to \mathbf{B}_0 (see Fig. 2.2d). The X-wave experience two cutoffs, one at ω_R and the other at ω_L , given in Eqs. (2.27) and (2.28), respectively. The X-wave can be absorbed at two resonances, the *upper-hybrid resonance*

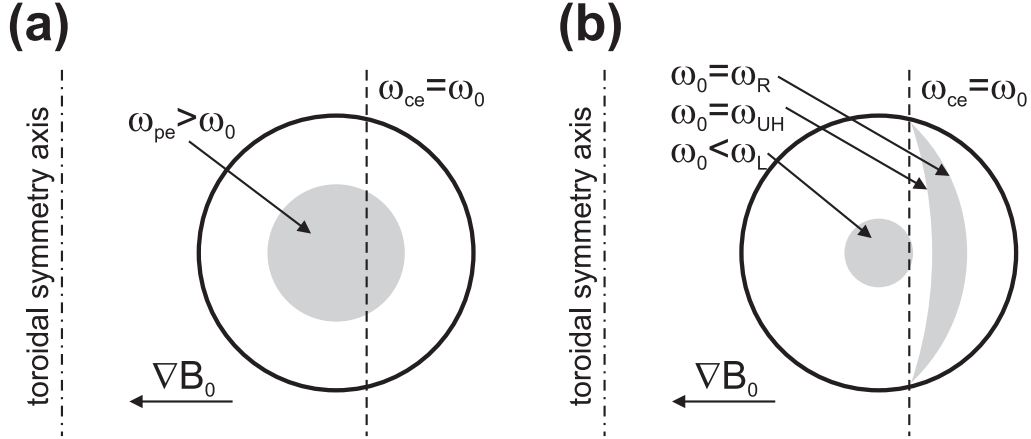


Figure 2.4: Cutoffs and resonances in a poloidal cross section assuming a parabolic density profile and a $1/R$ dependence of the background magnetic field for (a) O-wave and (b) X-wave injection. The filled grey areas mark evanescent regions for the waves.

ω_{UH} (UHR) and the lower-hybrid resonance ω_{LH} (LHR). They read as follows:

$$\omega_{UH} = \sqrt{\omega_{pe}^2 + \omega_{ce}^2}, \quad (2.29)$$

$$\omega_{LH} = \sqrt{\omega_{ci}\omega_{ce}} \left(\frac{\omega_{pe}^2 + \omega_{ci}\omega_{ce}}{\omega_{pe}^2 + \omega_{ce}^2} \right)^{1/2}. \quad (2.30)$$

The dispersion relations of both the O-wave and the X-wave are plotted in Fig. 2.3b. Due to its low frequency values the branch corresponding to the lower-hybrid wave is not given in the graph.

In Figs. 2.4a and 2.4b, the cutoffs and resonances for O- and X-wave injection are depicted, respectively, in a poloidal cross section of a typical fusion plasma with a $1/R$ dependence of the background magnetic field, where R is the major radius of the torus, and a parabolic density profile. The filled grey areas denote regions where the incident wave is *evanescent*. One can see that the X-wave can only reach the UHR from the high-field side. For higher densities the cutoffs and the UHR move to the plasma edge.

2.2.3 Effect of increasing plasma temperature

If the energy of the particle species α increases, its average Larmor radius, given by

$$\rho_{L,\alpha} = \frac{\sqrt{2m_\alpha T_\alpha}}{q_\alpha B_0}, \quad (2.31)$$

also increases. This results in effects that are not present in the cold plasma approximation. These *finite Larmor radius effects* are important for plasma heating:

The absorption of the O- and X-wave at the cyclotron resonance and its harmonics becomes now possible. If the Larmor radius is on the order of the wavelength of the incident wave or larger, absorption becomes important. In Ref. [2] a detailed description of the absorption of the O- and X-wave at the cyclotron harmonics is given. One of the main results are equations, which allow the calculation of the optical depths at the resonances and, hence, the amount of absorbed power in the plasma. Here, the results of Ref. [2] will be briefly presented.

For the O-wave, the absorption coefficient $\alpha^{(O)}$ at the first harmonic of the electron cyclotron frequency, $n = 1$, is approximately the same as the absorption coefficient for the X-wave of the second harmonic $n = 2$:

$$\alpha_{n=1}^{(O)} \approx \alpha_{n=2}^{(X)} \approx \left(\frac{\omega_{pe}}{\omega_{ce}} \right)^2 \frac{\omega_{ce}}{c}. \quad (2.32)$$

The absorption at the fundamental cyclotron resonance of the X-wave is only slightly larger than that of the third-harmonic of the X-wave and that of the second-harmonic of the O-wave:

$$\alpha_{n=1}^{(X)} \approx \left(\frac{\omega_{ce}}{\omega_{pe}} \right)^2 \left(\frac{v_{th,e}}{c} \right)^2 \frac{\omega_{ce}}{c} \quad (2.33)$$

$$\alpha_{n=2}^{(O)} \approx \alpha_{n=3}^{(X)} \approx \left(\frac{\omega_{pe}}{\omega_{ce}} \right)^2 \left(\frac{v_{th,e}}{c} \right)^2 \frac{\omega_{ce}}{c}, \quad (2.34)$$

with $v_{th,e} = \sqrt{2T_e/m_e}$ the thermal velocity of the electrons. The absorption coefficient for higher harmonics is of the order of $(v_{th,e}/c)^4$, which is usually very small and therefore negligible.

Heating at the electron cyclotron resonance layer is referred to as *electron cyclotron resonance heating* (ECRH). It is a well proven heating method in hot fusion plasmas. Review articles on this topic can be found for example in Refs. [6, 7].

Another finite temperature effect is the occurrence of new types of waves, which are not included in the cold plasma description. One of these, the electron Bernstein wave, will be described in the following section.

2.3 Bernstein waves

In 1958, I. Bernstein dealt with theoretical investigations of wave propagation in hot magnetized plasmas [25]. He found a new type of waves, which are absorbed at the cyclotron resonance and have no density cutoff. In honor of his work, these waves are referred to as *electron Bernstein waves* (EBW). The experimental demonstration of the Bernstein waves was performed by Crawford *et al.* six years later [26]. Preinhaelter *et al.* proposed in 1973 a mode conversion process to excite these waves with electromagnetic waves injected from vacuum with the prospect of applying them to plasma heating [27]. The feasibility of heating fusion plasmas with Bernstein waves

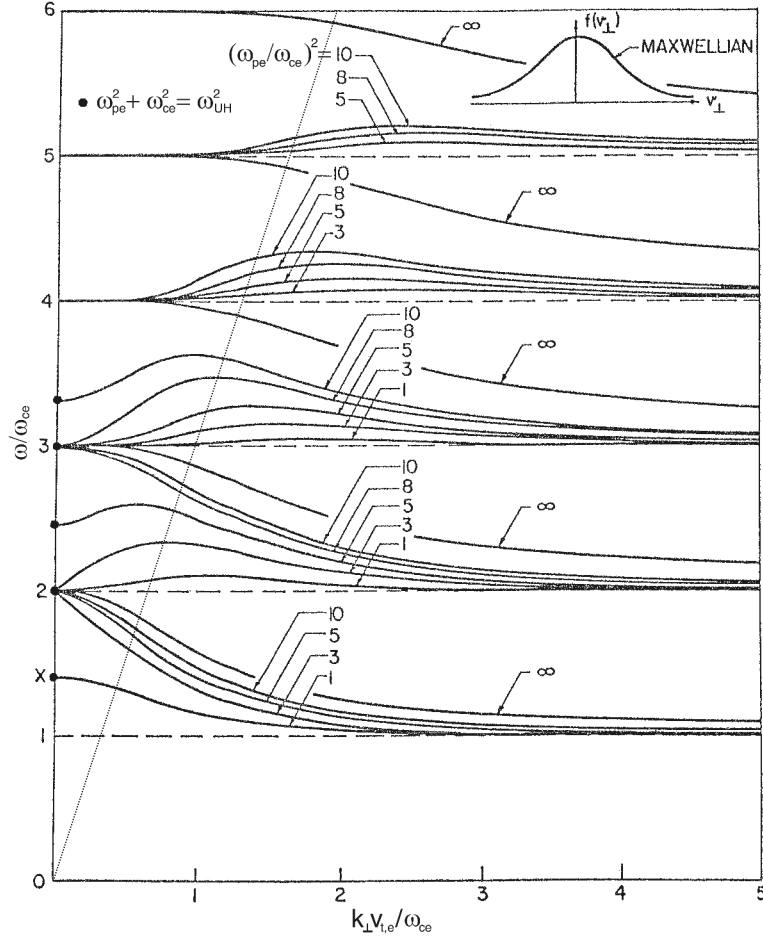


Figure 2.5: Dispersion relation of the electrostatic EBW for perpendicular propagation at different values of the parameter $\omega_{pe}^2/\omega_{ce}^2$. The scope of application is indicated by the dotted line: left of it, the electrostatic approximation is no longer valid and coupling with electromagnetic modes occur. Figure is taken and adapted from Crawford *et al.* [31].

was successfully demonstrated by Laqua *et al.* at the Wendelstein 7-AS stellarator [28]. Laqua *et al.* also showed the possibility of using EBW as a diagnostics in fusion plasmas [29]. Bernstein waves are not only a research topic in fusion related plasma physics, but also in extraterrestrial physics [30]. In this section, the basic properties the EBW are presented.

In the cold plasma approximation, described in Sec. 2.2, the currents are described by the sum of the electron and ion fluid motion. In the kinetic approach the particle species are described by distribution functions. If collisions are neglected and only electromagnetic interactions with the plasma particles are taken into account, the Vlasov equation [32] can be applied:

$$\frac{\partial f_{\alpha}}{\partial t} + \mathbf{v} \cdot \frac{\partial f_{\alpha}}{\partial \mathbf{r}} + \frac{q_{\alpha}}{m_{\alpha}} \left(E + \frac{1}{c} \mathbf{v} \times \mathbf{B} \right) \cdot \frac{\partial f_{\alpha}}{\partial \mathbf{v}} = 0, \quad (2.35)$$

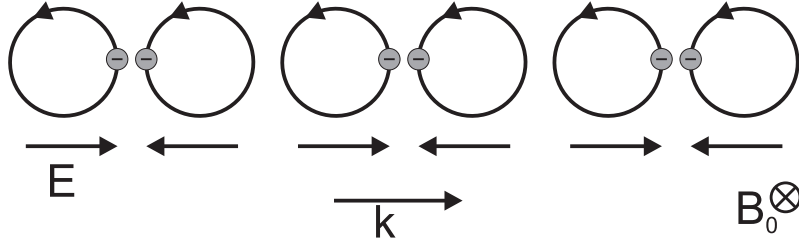


Figure 2.6: Sketch to illustrate the EBW propagation mechanism: The EBW propagates as charge density perturbations created by a collective gyration of the electrons. The wavelength of the EBW is on the order of the electron gyroradius.

with $f_\alpha(\mathbf{r}, \mathbf{v}, t)$ the distribution function of the particles of type α .

The kinetic description of the plasma response allows new types of waves. For perpendicular propagation and in the limit of sufficiently large k_\perp (reduction to the electrostatic solution), the xx -component of the *hot* dielectric tensor is given by [22]

$$\varepsilon_{xx} = 1 - \frac{\omega_{pe}^2}{\omega_{ce}^2} \sum_{n=1}^{\infty} \frac{e^{-\lambda} I_n(\lambda)}{\frac{\lambda}{2} \left[\left(\frac{\omega}{n\omega_{ce}} \right)^2 - 1 \right]}, \quad (2.36)$$

where n denotes the harmonics, $\lambda = (k_\perp \rho_{L,e})^2$ and I_n the modified Bessel function [33]. The dispersion relation, resulting from $\varepsilon_{xx} = 0$, was first derived by Bernstein [25]. Hence, the new type of waves found, are referred to as *electron Bernstein waves* (EBW).

Figure 2.5, taken from Ref. [31], shows the solutions of the EBW dispersion relation for values of $1 \leq \omega_{pe}^2/\omega_{ce}^2 \leq 10$. The diagram is only valid for $k_\perp \rho_{L,e} \geq n/3$ [34]. This threshold is depicted in Fig. 2.5 by a dotted line. On its left side, the electrons are no longer capable to sustain the propagation of the EBW, and a transition to the X-mode occurs in this region. A discussion of the effect including electromagnetic contributions can be found in Ref. [35].

The sum over the Bessel functions gives rise to a number of possible roots in ω for fixed k , which is equivalent to a number of possible waves, termed the EBW or cyclotron harmonic waves. No cutoffs are found for EBW. Hence, the waves can propagate into high density plasma without being reflected until they have reached a cyclotron resonance, where the EBW is absorbed, even at high harmonics. The EBW provides a tool to heat overdense plasmas, with densities exceeding the cutoff density of usual electromagnetic waves.

From Fig. 2.5 it can also be deduced that the EBW can be a *backward wave*: the phase velocity, $v_{ph} = \omega/k$, and the group velocity, $v_{gr} = \partial\omega/\partial k$, have opposite signs.

The EBW is an electrostatic wave that propagates predominantly perpendicular to the background magnetic field. Typical wavelengths are on the order of four

times the electron Larmor radius ρ_{Le} [16, 34]. They are sustained by a coherent gyro motion of the electrons and propagate as electron density accumulation and rarefaction, see Fig. 2.6. Due to their electrostatic nature, they cannot propagate in vacuum. Hence, the problem to be solved with the EBW is their excitation, which is realized by coupling to electromagnetic waves inside the plasma. These coupling scenarios are described in the next section.

For a comprehensive overview on EBW see the review by Laqua [16] and the references cited therein.

2.4 Excitation of EBW

In the following sections, the two possibilities to excite EBW by coupling to electromagnetic waves will be described: one is the O–X–B, the other the direct X–B mode conversion scheme. The conversion efficiency of the two schemes can be optimized in different parameter regions.

2.4.1 O–X–B mode conversion

In 1973, Preinhaelter and Kopecký [27] suggested a new method to heat overdense plasmas. To this end, an O-mode¹ is injected into the plasma from the low-field side, as shown in Fig. 2.7. At the optimum angle between the wave vector and the background magnetic field, the O-mode is converted to an X-mode at the O-mode cutoff-layer. The X-mode then propagates outwards until it reaches the upper-hybrid resonance layer, where it is converted into an EBW propagating again inwards. This mode conversion scheme was first experimentally verified for stellarators in 1997 by Laqua *et al.* [28] and for tokamaks in 2007 by Mueck *et al.* [36].

We consider a slab model, with a homogenous background magnetic field \mathbf{B}_0 directed along the z -axis and the density gradient ∇n directed along the x -axis. For shallow density gradients, $N_x \gg (k_0 L_n)^{-1}$ with $L_n = n/\nabla n$ the density scale length and k_0 the vacuum wavenumber, and with ion dynamics neglected, the dispersion relation has the following form:

$$N_x^2 + N_y^2 + N_z^2 = 1 - \frac{2X(1-X)}{2(1-X) - Y^2 \sin^2 \theta \pm \Gamma}, \quad (2.37)$$

with $\Gamma = (Y^4 \sin^4 \theta + 4(1-X)^2 Y^2 \cos^2 \theta)^{1/2}$. Here, the widespread abbreviations

$$X = \omega_{pe}^2 / \omega_0^2 \quad \text{and} \quad Y = \omega_{ce} / \omega_0 \quad (2.38)$$

are used. The + and the – signs correspond to the O- and the X-mode, respectively [37]. The dispersion relation in the form in Eq. (2.37) is also referred to as

¹Here, the terms O- and X-wave are used only for perpendicular injection (see Fig. 2.2), otherwise the terms O- and X-mode are used.

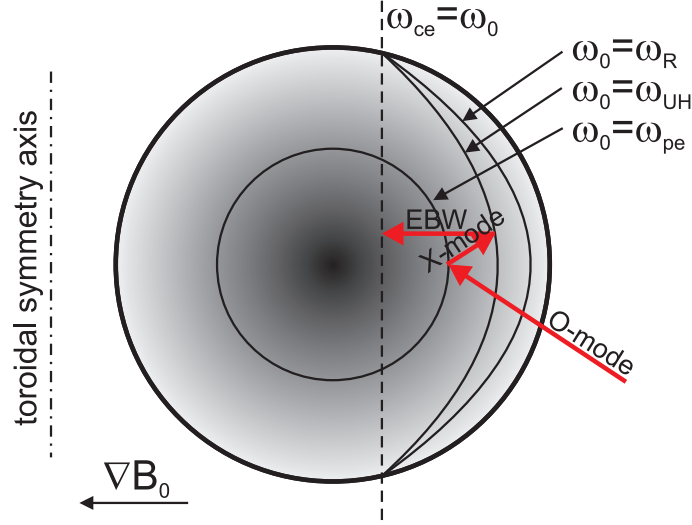


Figure 2.7: Sketch of the O-X-B mode conversion process in a poloidal cross section for a typical fusion plasma with a parabolic density profile and a $1/R$ dependence of the background magnetic field.

Appleton-Hartree dispersion relation in honor of their fundamental work in the field of waves in magnetized plasmas [23].

For $\Gamma = 0$, which occurs for $X = 1$ and $\theta = 0$, the O- and the X-mode coalesce. To investigate this overlap, the case of $\theta = 0$ ($N_x = N_y = 0$) is first considered. Equation (2.37) then reads:

$$N_z^2 = \frac{1 - X \pm Y}{1 \pm Y}. \quad (2.39)$$

In Eq. (2.39) only the + sign is meaningful, otherwise $0 < N_z^2 < 1$ would not be fulfilled. Consider an O-mode approaching the cutoff at ω_{pe} . The value of X then approaches 1 and at the cutoff N_z^2 reads

$$N_{z,opt}^2 = \frac{Y}{1 + Y}. \quad (2.40)$$

This value is approached for X *increasing* from lower values to $X \rightarrow 1$, i. e. a wave propagating into direction of increasing density, and for X *decreasing* from higher values to $X \rightarrow 1$, which is a wave propagating into direction of decreasing density. Hence, $N_{z,opt}$ connects both branches and gives the optimum value for mode conversion.

Figure 2.8 shows the results of Eq. (2.37) for three values of $\theta \neq 0$ with $Y = 0.85$ and $N_y = 0$. When the X-mode enters the plasma, which corresponds to a wave coming from $X = 0$, it gets reflected after a short distance. This version of the X-mode is also referred to as FX-mode (*fast*). The O-mode propagates up to its cutoff density, also known as *critical density*, where it encounters a region of evanescence

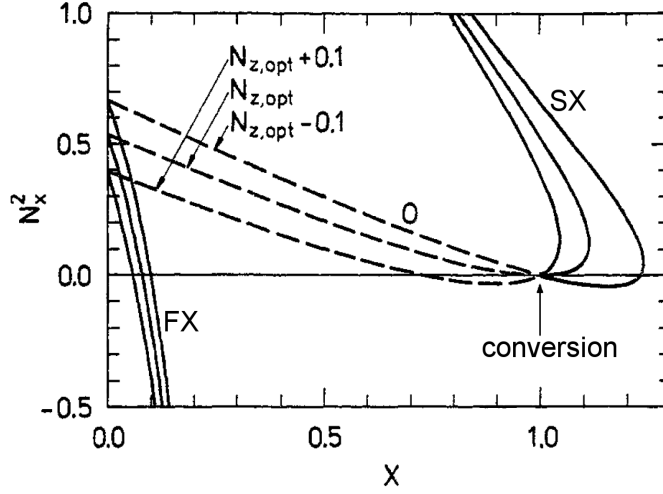


Figure 2.8: N_x^2 as function of X for $Y = 0.85$ and $N_y = 0$, dashed curves represents the O-mode, solid curve the X-mode (adapted from Ref. [38]).

if $N_z \neq N_{z,opt}$, which is characterized by $N_x^2 < 0$. Close to the cutoff density, the branch of the O-mode is connected with a branch of the X-mode, which is referred to as SX-mode (slow). Only for $N_z = N_{z,opt}$ this connection is realized without passing an evanescent region. According to Ref. [27] this is equivalent to perfect conversion from the O-mode to the SX-mode. If an evanescent region is traversed, only a part of the incident power is transmitted and reaches the conversion point, marked in Fig. 2.8. This part is then converted into the SX-mode. The other part is reflected and propagates as O-mode outwards, leaving the plasma without further interactions and does not contribute to mode conversion.

In the literature exist some slightly different formulas to calculate the efficiency of the O–SX mode conversion in the limit of slowly varying plasma densities [27, 37, 39], that is in the WKB limit of $k_0 L_n \gg 1$. In Ref. [40], Hansen showed in a numerical study the following formula (the one from Mjølhus [39]) to be the best approximation to the exact result of the conversion efficiency:

$$\eta_M = \exp \left\{ -\pi k_0 L_n \sqrt{Y/2} \left[2(1+Y)(N_z - N_{z,opt})^2 + N_y^2 \right] \right\}, \quad (2.41)$$

where N_z and N_y are the components of the refractive index in the z - (along \mathbf{B}_0) and the y -direction (perpendicular to \mathbf{B}_0 and ∇n), respectively. For L_n and Y the respective values at the conversion point need to be inserted. Obviously, the conversion efficiency is described by a 2D Gaussian in the N_z – N_y space. The width of the Gaussian scales inversely with the normalized density gradient length $k_0 L_n$ and the magnetic field in Y .

After the O–SX conversion, also named O–X conversion, the X-mode propagates outwards, as can be seen from Fig. 2.8. In contrast to the O-mode, the generated X-mode has a longitudinal component of the electric field. When the X-mode

approaches the UHR, its wavelength becomes shorter, the refractive index goes to infinity and, hence, the phase velocity goes to zero (see Fig. 2.3b). When the phase velocity becomes comparable to the electron thermal velocity, the cold plasma model is no longer sufficient and kinetic effects have to be taken into account. The X-mode can now, finally, be converted into a backwards propagating EBW [35]. The verification of the conversion process is complicated by the fact that part of the energy can go into collisional damping around the UHR, parametric decay processes or second harmonic generation processes [16, 38].

Due to the simplified slab geometry assumed (N_z is conserved), the optimum angle of incidence at the plasma boundary, with respect to \mathbf{B}_0 , can be calculated from Eq. (2.40):

$$\theta_{opt} = \arccos \left\{ \left(\frac{Y}{1+Y} \right)^{1/2} \right\}. \quad (2.42)$$

However, it is not only the optimum angle of incidence, which is required to get maximum conversion efficiency. To ensure that a pure O-mode is excited in the plasma, the wave must have the correct polarization at the plasma boundary. From the wave equation, Eq. (2.19), the polarization of the wave in the plasma can be calculated as

$$i \frac{E_x}{E_y} = \frac{S - N^2}{D} \quad (2.43)$$

$$\frac{E_x}{E_z} = \frac{P - N^2 \sin^2 \theta}{N^2 \cos \theta \sin \theta}, \quad (2.44)$$

or, in terms of the abbreviations X and Y :

$$i \frac{E_x}{E_y} = \frac{1}{Y} \left[\frac{(1 - Y^2)(1 - N^2)}{X} - 1 \right] \quad (2.45)$$

$$\frac{E_x}{E_z} = - \frac{1 - X - N^2 \sin^2 \theta}{N^2 \cos \theta \sin \theta}. \quad (2.46)$$

Obviously, if incident at an oblique angle θ , the waves must be elliptically polarized.

From the Appleton-Hartree dispersion relation, Eq. (2.37), an expression for $(1 - N^2)/X$ is obtained, which can be inserted into Eq. (2.45). The wave polarization in vacuum ($X \rightarrow 0$), has then the following form:

$$i \frac{E_x}{E_y} = - \frac{Y \sin^2 \theta \pm \sqrt{Y^2 \sin^4 \theta + 4 \cos^2 \theta}}{2} \quad (2.47)$$

$$\frac{E_x}{E_z} = - \frac{1}{\tan \theta}. \quad (2.48)$$

If the wave is incident in the xz -plane and \mathbf{B}_0 is directed along the z -axis, one gets for the polarization of the wave in the coordinate system of the incident wave (x', y') [38]

$$\frac{E_{x'}}{E_{y'}} = \frac{\mp Y \sin^2 \theta + \sqrt{Y^2 \sin^4 \theta + 4 \cos^2 \theta}}{2 \cos \theta}. \quad (2.49)$$

If a wave is injected at the optimum angle θ_{opt} , Eq. (2.49) gives the polarization that is needed to get optimum conversion efficiency.

In vacuum, the O- and X-mode are degenerate. As soon as the wave enters a magnetized plasma with finite density, both modes will generally be excited [7]. As an example, for an injection perpendicular to \mathbf{B}_0 , the incident wave needs to be linearly polarized to excite either the O- or the X-mode [38]. A numerical study, surveying the influence of the polarization of the incident wave on the conversion efficiency, has been performed by Igami *et al.* [41]. It illustrates how the polarization for optimum mode conversion efficiency starts to deviate from the approximate one given by Eq. (2.49) with increasing steepness of the density profile.

The SX–B conversion at the UHR is usually assumed to be complete. If, however, the density gradient is very steep, the distance between the R-cutoff and the UHR becomes smaller and the SX-mode can tunnel through this evanescent region and leave the plasma as FX-mode. This tunneling has been analyzed in ionospheric research in the past [42] and recently also for fusion plasmas [34, 43]. Here, the formula given in Ref. [34] is applied to estimate the SX–FX conversion efficiency:

$$\eta_{SX-FX} = \exp \left\{ -\pi k_0 L_n Y^2 \sqrt{\frac{\omega_{UH}/\omega_{ce} - 1}{X}} \right\}. \quad (2.50)$$

The tunneling efficiency is plotted in Fig. 2.9 as a function of $k_0 L_n$ for $Y = 0.6$, $X = 0.8$ and $\omega_{UH}/\omega_{ce} = 1.67$, which correspond to typical values at the UHR in the poloidal cross section in TJ-K, where the 2.45 GHz antenna is located (see Sec. 5 for details). Obviously, the tunneling and, hence, the degradation to the SX–B conversion becomes important only for very small values of $k_0 L_n < 2$. Nevertheless, if steep density profiles and a large vacuum wavelength are present, the exact shape of the profiles can become a decisive factor for the heating efficiency.

2.4.2 Direct X–B conversion

Another method to generate EBW, is the direct X-B conversion. Here, the fast X-mode (FX-mode), incident from vacuum tunnels through the evanescent region between the R-cutoff and the UHR and couples to the SX-mode. The SX-mode is reflected at the L-cutoff and then, when approaching the UHR, mode-converted to an EBW. This triplet of cutoff–resonance–cutoff forms a *mode conversion resonator* [43], namely a resonator in which the conversion to EBW is the effective dissipation mechanism. The theory of the direct X–B conversion was presented by Ram *et al.* [43], who derived the conversion efficiency and showed that efficient mode conversion is possible over a broad range of frequencies and launch angles.

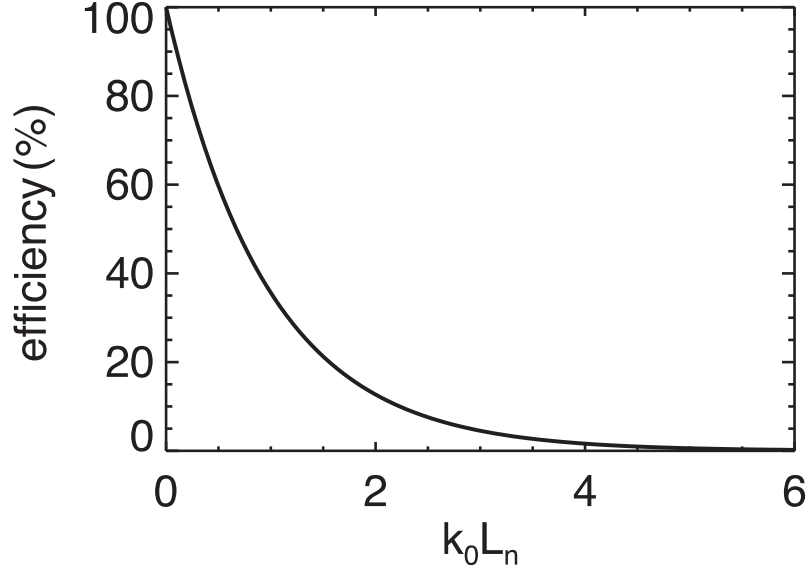


Figure 2.9: Tunneling efficiency of the SX-mode to the FX-mode through the evanescent region defined by the R-cutoff and the UHR as a function of the normalized density gradient length $k_0 L_n$ (evaluated at the UHR for typical values of a low field discharge in TJ-K).

According to Ref. [43] the conversion efficiency for the direct X–B conversion is:

$$C = 4e^{-\pi\eta_B} (1 - e^{-\pi\eta_B}) \cos^2(\gamma + \phi/2), \quad (2.51)$$

where γ is the phase of the gamma function $\Gamma(-i\eta_B/2)$, ϕ the phase between the SX-mode propagating towards the L-cutoff and the reflecting component propagating towards the UHR. η_B is the *Budden parameter* [42], which is obtained by expanding the wave potential around the UHR, to find the position of the R-cutoff. In the limit of $L_B \gg L_n$, where L_B is the scale length of the magnetic field, the Budden parameters reads

$$\eta_B \approx \frac{\omega_{ce} L_n}{c\alpha} \left(\sqrt{1 + \alpha^2} - 1 \right)^{1/2}, \quad \alpha = \left. \frac{\omega_{pe}}{\omega_{ce}} \right|_{\text{UHR}}. \quad (2.52)$$

The phase factors γ and ϕ in Eq. (2.51) can significantly modulate the conversion efficiency C . They result from the phasing of the waves in the cavity [16]. Due to its sensitivity to the phase, the conversion efficiency becomes also sensitive to density fluctuations, which may be due to turbulence.

An upper limit of the conversion efficiency is given by the envelope of C , which is the phase independent part of Eq. (2.51):

$$C_{\max} = 4e^{-\pi\eta_B} (1 - e^{-\pi\eta_B}). \quad (2.53)$$

In Fig. 2.10, the envelope of the conversion efficiency, Eq. (2.53), is plotted for typical values of a low-field discharge in TJ-K, that is $\alpha|_{\text{UHR}} \approx 1.4$ and $L_n|_{\text{UHR}} \approx$

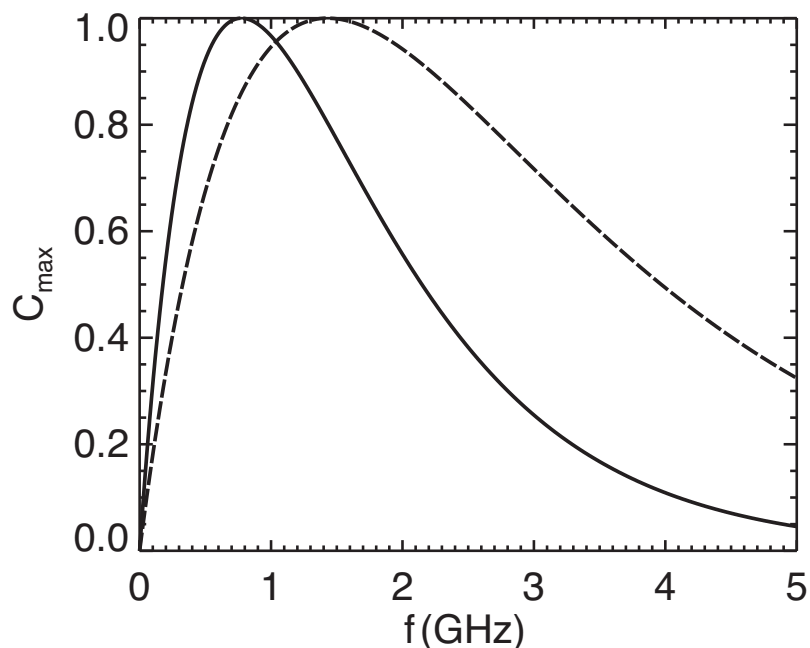


Figure 2.10: Envelope of conversion efficiency of direct X-B conversion, calculated with Eq. (2.53). Solid line corresponds to standard discharge and plasma parameters in TJ-K at low magnetic field (see Sec. 5), dashed line corresponds to a discharge with 10 times higher plasma density.

0.02 m. A graph corresponding to 10 times higher density is also shown. Note that perfect conversion efficiency can be achieved at $f \approx 800$ MHz. At $f = 2450$ MHz, the microwave heating frequency in TJ-K, the efficiency has decreased to 40 %. Despite this promising high value one has to keep in mind that these efficiencies are maximum values that can decrease significantly through phase variations, caused by density fluctuations. Furthermore, one cannot expect the power, which is stored in the resonator, to be completely mode-converted into EBW, since other dissipation mechanisms, e. g. collision or parametric decay, may also be present [43].

Chapter 3

The full-wave code IPF-FDMC

In order to describe electromagnetic wave propagation in plasmas there exist basically two different approaches. One is the geometrical optical approximation, where the wave is described as a ray, known as *ray tracing*. The second approach is referred to as *full-wave* solution, since Maxwell's equations are exactly solved. This chapter will mainly deal with the full-wave code IPF-FDMC, which has been developed in the course of this thesis. It is applied to wave propagation and heating in TJ-K. Furthermore, the code has been successfully used to optimize O-X-B heating schemes for larger scale fusion devices [44, 45].

First, the principle of ray tracing will be described briefly. Then the full-wave code and its applications are presented.

3.1 Ray tracing

If the refractive index changes only slowly over a distance that is comparable to the wavelength of the incident wave, geometrical optics can be used to calculate the wave trajectory [22, 46, 47].

The group velocity $\mathbf{v}_g = \partial\omega/\partial\mathbf{k}$ indicates the direction of the energy flow. Consider a dispersion relation,

$$D(\omega, \mathbf{r}, \mathbf{k}, t) = 0, \quad (3.1)$$

where D is varying slowly as a function of \mathbf{r} and t and no losses are included. Then ω can be expressed as $\omega = \omega(\mathbf{r}, \mathbf{k}, t)$. According to Ref. [47] the ray trajectories are then given by

$$\frac{d\mathbf{r}}{dt} = -\frac{\partial D/\partial\mathbf{k}}{\partial D/\partial\omega} \quad \frac{d\mathbf{k}}{dt} = \frac{\partial D/\partial\mathbf{r}}{\partial D/\partial\omega} \quad \frac{d\omega}{dt} = \frac{\partial D/\partial t}{\partial D/\partial\omega}. \quad (3.2)$$

Starting at the plasma boundary with a single ray or a bundle of rays, corresponding to an incident beam of finite width, Eqs. (3.2) can be integrated to get the characteristics of the ray.

As noted above, geometrical optics is applicable only in media, where the refractive index varies slowly along the ray trajectory. At cutoffs or resonances, this assumption breaks down. In plasmas the size on the order of the wavelength, which is the case for TJ-K, the assumption breaks down, too. Hence, wave propagation in TJ-K cannot be investigated with a ray tracing code. A full-wave solution is necessary, which directly solves Maxwell's equations.

3.2 Principles of the full-wave code IPF-FDMC

Here, the basic elements of the full-wave code IPF-FDMC (*Institut für Plasmaforschung - Finite Difference code for Mode Conversion*) will be presented. It is a time-dependent code which solves Maxwell's equations and the fluid equation of motion for the electrons by replacing the derivatives by finite differences. A brief overview of the general calculation scheme will be given including some remarks on the boundary conditions and the implementation of the microwave antenna in the algorithm. A comprehensive overview of the FDTD technique can be found in the textbook by Taflove and Hagness [48].

3.2.1 The Yee algorithm

To describe propagation of electromagnetic waves in inhomogeneous media, in which typical scale lengths are of the order of the wavelength, the approximation of geometrical optics is no longer valid. It is necessary to solve Maxwell's equations:

$$\frac{\partial}{\partial t} \mathbf{B} = -\nabla \times \mathbf{E} \quad (3.3)$$

$$\frac{\partial}{\partial t} \mathbf{E} = c^2 \nabla \times \mathbf{B} - \frac{1}{\epsilon_0} \mathbf{J}. \quad (3.4)$$

The response of the plasma electrons is included in the current density \mathbf{J} and will be described in detail in Sec. 3.2.2. The ions are taken to be fixed due to their large mass. Several methods exist to solve Eqs. (3.3) and (3.4) numerically. We decided on the finite-difference time-domain (FDTD) technique. It was first described in 1966 by Yee [49], therefore it is sometimes referred to as *Yee algorithm*.

In a Cartesian coordinate system, Eqs. (3.3) and (3.4) can be written as the

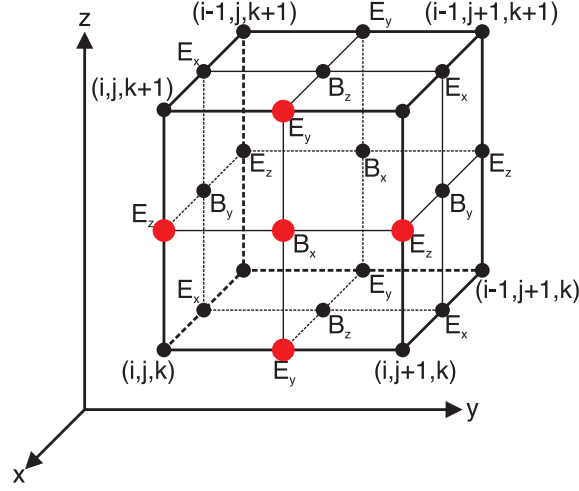


Figure 3.1: Illustration of a Yee cell, where the E -components are located in the middle of the edges of the cell and the B -components are in the center of the faces. One B_x component and the E components necessary to calculate it are marked by filled red circles.

following system of six scalar equations:

$$-\frac{\partial B_x}{\partial t} = \frac{\partial E_z}{\partial y} - \frac{\partial E_y}{\partial z} \quad (3.5)$$

$$-\frac{\partial B_y}{\partial t} = \frac{\partial E_x}{\partial z} - \frac{\partial E_z}{\partial x} \quad (3.6)$$

$$-\frac{\partial B_z}{\partial t} = \frac{\partial E_y}{\partial x} - \frac{\partial E_x}{\partial y} \quad (3.7)$$

$$\frac{\partial E_x}{\partial t} = c^2 \left(\frac{\partial B_z}{\partial y} - \frac{\partial B_y}{\partial z} \right) - \frac{1}{\epsilon_0} J_x \quad (3.8)$$

$$\frac{\partial E_y}{\partial t} = c^2 \left(\frac{\partial B_x}{\partial z} - \frac{\partial B_z}{\partial x} \right) - \frac{1}{\epsilon_0} J_y \quad (3.9)$$

$$\frac{\partial E_z}{\partial t} = c^2 \left(\frac{\partial B_y}{\partial x} - \frac{\partial B_x}{\partial y} \right) - \frac{1}{\epsilon_0} J_z. \quad (3.10)$$

The grid coordinates (i, j, k) are defined as

$$(i, j, k) = (i\Delta x, j\Delta y, k\Delta z) = (i\delta, j\delta, k\delta), \quad (3.11)$$

where δ is the spatial grid size. An arbitrary function of space and time can then be written as

$$F(i\delta, j\delta, k\delta, n\Delta t) = F^n(i, j, k), \quad (3.12)$$

with Δt the time increment and n the time index.

The three dimensional coordinate system and the grid positions of the E and B components are shown in Fig. 3.1. The cell, drawn in the figure, is referred to as the

Yee cell. One can see that each B component is located between a pair of E -field components and vice versa.

Replacing the spatial and temporal derivatives of F by finite differences results in the following equations:

$$\left. \frac{\partial F^n}{\partial x} \right|_{i,j,k} = \frac{F^n(i + \frac{1}{2}, j, k) - F^n(i - \frac{1}{2}, j, k)}{\delta} \quad (3.13)$$

$$\left. \frac{\partial F^n}{\partial t} \right|_{i,j,k} = \frac{F^{n+1/2}(i, j, k) - F^{n-1/2}(i, j, k)}{\Delta t}. \quad (3.14)$$

The equations for y and z follow accordingly.

Equations (3.13) and (3.14) can now be applied to the system of the six scalar Eqs. (3.5)–(3.10). For Eq. (3.5) the result reads

$$\begin{aligned} & \frac{B_x^{n+1/2}(i, j + \frac{1}{2}, k + \frac{1}{2}) - B_x^{n-1/2}(i, j + \frac{1}{2}, k + \frac{1}{2})}{\Delta t} \\ &= \frac{E_y^n(i, j + \frac{1}{2}, k + 1) - E_y^n(i, j + \frac{1}{2}, k)}{\delta} \\ & \quad - \frac{E_z^n(i, j + 1, k + \frac{1}{2}) - E_z^n(i, j, k + \frac{1}{2})}{\delta}. \end{aligned} \quad (3.15)$$

Hence, the B_x component at the time $t = (n + 1/2)\Delta t$ is calculated from the value of B_x at $t = (n - 1/2)\Delta t$ and from the corresponding E components at $t = n\Delta t$:

$$\begin{aligned} B_x^{n+1/2}\left(i, j + \frac{1}{2}, k + \frac{1}{2}\right) &= B_x^{n-1/2}\left(i, j + \frac{1}{2}, k + \frac{1}{2}\right) \\ &+ \frac{\Delta t}{\delta} \left[E_y^n\left(i, j + \frac{1}{2}, k + 1\right) - E_y^n\left(i, j + \frac{1}{2}, k\right) \right. \\ & \quad \left. - E_z^n\left(i, j + 1, k + \frac{1}{2}\right) + E_z^n\left(i, j, k + \frac{1}{2}\right) \right] \end{aligned} \quad (3.16)$$

In Fig. 3.1, the B_x component and the E components necessary to calculate B_x are marked by filled red circles. One can clearly recognize that this calculation scheme uses centered differences in space. The equations for the y and z components, Eqs. (3.6) and (3.7), respectively, can be constructed accordingly.

For the x component of the E -field, one gets

$$\begin{aligned} E_x^n\left(i + \frac{1}{2}, j, k\right) &= E_x^{n-1}\left(i + \frac{1}{2}, j, k\right) \\ &+ \frac{\Delta t}{\delta} \left[B_z^{n-1/2}\left(i + \frac{1}{2}, j + \frac{1}{2}, k\right) - B_z^{n-1/2}\left(i + \frac{1}{2}, j - \frac{1}{2}, k\right) \right. \\ & \quad \left. - B_y^{n-1/2}\left(i + \frac{1}{2}, j, k + \frac{1}{2}\right) + B_y^{n-1/2}\left(i + \frac{1}{2}, j, k - \frac{1}{2}\right) \right] \\ &+ \Delta t J_x^{n-1/2}\left(i + \frac{1}{2}, j, k\right) \end{aligned} \quad (3.17)$$

Again, the other components can be constructed accordingly.

A leapfrog scheme is used, where the E - and B -fields are calculated at alternating half time steps. Since the E - and B -field calculation uses centered differences not only in space but also in time, the Yee algorithm is second-order accurate.

There was only little interest in the FDTD technique in the first years after publication [50]. With the availability of low-cost but powerful computational resources, it has become a very popular technique for dealing with electromagnetic issues in general. Since the 1990s [51, 52], the application of FDTD-codes to fusion related plasma physics has started to become more and more widespread. An important application is reflectometry, which is used to measure electron density profiles and turbulent fluctuations [53, 54, 55, 56].

3.2.2 The plasma response

As mentioned in Sec. 3.2.1, the plasma effects are included in the current density \mathbf{J} , which is, according to Ref. [51], obtained by solving the equation of motion for the electrons. For the electron fluid, the linearized equation of motion reads [57]

$$m_e n_e \frac{\partial}{\partial t} \mathbf{v} = -en_e (\mathbf{E} + \mathbf{v} \times \mathbf{B}_0), \quad (3.18)$$

with \mathbf{v} the electron fluid velocity and \mathbf{E} the wave electric field. Collisions are neglected in Eq. (3.18). The current density \mathbf{J} is given by $\mathbf{J} = -en_e \mathbf{v}$. With the equations for the electron plasma frequency and the electron cyclotron frequency, $\omega_{pe} = \sqrt{e^2 n_e / (\epsilon_0 m_e)}$ and $\omega_{ce} = eB_0 / m_e$, respectively, the current density reads

$$\frac{\partial}{\partial t} \mathbf{J} = \epsilon_0 \omega_{pe}^2 \mathbf{E} - \omega_{ce} \mathbf{J} \times \hat{\mathbf{B}}_0, \quad (3.19)$$

with $\hat{\mathbf{B}}_0$ the unit vector in the direction of \mathbf{B}_0 . \mathbf{J} has to be calculated on the same grid as \mathbf{E} and in phase with \mathbf{B} . According to the calculation of \mathbf{E} and \mathbf{B} (see Sec. 3.2.1), for the x -component of \mathbf{J} one gets:

$$\begin{aligned} J_x^{n+1/2} \left(i + \frac{1}{2}, j, k \right) &= J_x^{n-1/2} \left(i + \frac{1}{2}, j, k \right) \\ &+ \Delta t \left[\epsilon_0 \omega_{pe}^2 E_x^n \left(i + \frac{1}{2}, j, k \right) \right. \\ &\left. - \omega_{ce} \left(\hat{B}_{0z} J_y^{n+1/2} \left(i, j + \frac{1}{2}, k \right) - \hat{B}_{0y} J_z^{n+1/2} \left(i, j, k + \frac{1}{2} \right) \right) \right]. \end{aligned} \quad (3.20)$$

The plasma density profile and background magnetic field, included via ω_{pe} and ω_{ce} in Eq. (3.19), respectively, can be of arbitrary shape on the grid.

3.2.3 The source

To excite a wave on the FDTD lattice, different methods are available in the code IPF-FDMC. One may distinguish between the case where only the field in the antenna plane is given and the case where the geometry of the antenna structure is given. Without an antenna structure, the microwave beam is created by adding a time-harmonic field to the corresponding components of the wave fields. This source is usually located along one line in the grid, referred to as *antenna aperture* in the following. A Gaussian beam, for example, along a single line with $y = z = \text{const}$ can be added to the z -component of the electric field on a 2D grid in the following manner:

$$E_z(x) = A(t)E_0 \exp \left\{ - \left(\frac{x - x_0}{w_{\text{gauss}}} \right)^2 \right\}, \quad (3.21)$$

with x_0 the center of the gaussian beam, w_{gauss} the beam waist and E_0 a constant defining the amplitude of the wave. The function $A(t)$ is slowly rising from 0 to 1 during several periods of oscillation, since a rapid turn-on of the source would result in the generation of a broad spectrum around the desired frequency. Tilting and focussing of the antenna beam can be realized by appropriate variation of the phase over the antenna aperture.

When the structure of the antenna is included in the simulations, the excitation of a wave is slightly different. Assume as an example a rectangular waveguide, with a horn antenna at its end. To excite the fundamental mode, the corresponding field distribution of this mode needs to be excited in the waveguide. It is also possible to excite a sinusoidal wave in one grid point, which would then be similar to a coax-waveguide coupler in a 2D geometry.

3.2.4 Boundary conditions

An important issue in full-wave simulations is the interaction of an electromagnetic wave with an obstacle. To treat this interaction rigorously, the obstacle needs to be placed in an open geometry, where no boundaries exist from which distorting reflections could occur. In a real experiment, the obstacle is surrounded by an absorbing material, from which no reflections occur. The same can be done in the full-wave code, if one is only interested in *single pass* interactions of the wave with the obstacle. An absorber located at the boundaries of the calculation grid is used which ensures that the wave fields are damped sufficiently for reflections from the absorber to be neglected. These type of absorbers are referred to as *non-radiating* or *non-reflective boundary conditions* [48].

To this end, a numerical absorber is used: If the wave enters the absorber region, its electric field is damped with a small damping coefficient ε that increases exponentially when the wave penetrates deeper into the absorber. With a thickness

of the absorber on the order of one to two times the vacuum wavelength, the waves are damped very well and reflections at the absorber can be neglected.

Other, numerically more sophisticated techniques for realizing absorbing boundaries, which need less grid points [58, 59, 60] can be in principle implemented. For the calculations presented in the thesis, the exponential method was sufficient.

To realistically model wave propagation in TJ-K, the modeling of metal walls (e. g. torus vessel, waveguides, horn antennas) is necessary. Taking the metal walls to be perfectly conducting and, hence, perfectly reflecting, allows to implement them in a simple way: The wave electric field parallel to the metal surface needs to be set to zero at the grid points, where the walls are located.

3.2.5 The code IPF-FDMC

The full-wave code IPF-FDMC uses the Yee algorithm, described in Sec. 3.2.1, to solve the following equations on a 2D Cartesian grid:

$$\frac{\partial}{\partial t} \mathbf{B} = -\nabla \times \mathbf{E} \quad (3.22)$$

$$\frac{\partial}{\partial t} \mathbf{E} = c^2 \nabla \times \mathbf{B} - \frac{1}{\epsilon_0} \mathbf{J} \quad (3.23)$$

$$\frac{\partial}{\partial t} \mathbf{J} = \epsilon_0 \omega_{pe}^2 \mathbf{E} - \omega_{ce} \mathbf{J} \times \hat{\mathbf{B}}_0 - \nu \mathbf{J}. \quad (3.24)$$

The electron collision frequency ν is introduced in Eq. (3.24) to represent a damping mechanism. A plasma slab model is assumed in which variations are allowed only along the density gradient, i. e. along the radial coordinate. All three components of \mathbf{B} , \mathbf{E} and \mathbf{J} are calculated but, since only 2D variations of the background parameters are allowed, the corresponding derivatives in the third dimension vanish.

The code is implemented in the programming language C. It is possible to use shared memory multiprocessing [61, 62], which can significantly speed-up the calculations, especially for large grids. It is possible to perform the simulations on a 1D- or 2D-grid, on which the background parameters can be of arbitrary shape.

The grid size δ has to be chosen with care. Obviously, it has to be a fraction of the vacuum wavelength λ_0 , and it must be small enough to ensure that the wave fields do not change significantly between two neighboring grid points. Hence, the grid size depends on the size of the smallest structure which needs to be resolved. Steeper profiles of the plasma density for example, require smaller grid sizes. Depending on the problem given, the grid size typically ranges from $\lambda_0/64 \geq \delta \geq \lambda_0/1500$. According to Ref. [63], errors occurring due to numerical dispersion are on order of 0.3 % for a grid size of $\delta = \lambda_0/20$ and decreases further with decreasing grid size. Thus, these errors can be neglected here.

To ensure the stability of the time-stepping algorithm, the choice of Δt is subject to some restrictions. Yee stated already a criterion to ensure numerical stability [49], but this statement was wrong, as was first pointed out by Taflové [64]. The correct

requirement that needs to be fulfilled is the following:

$$c\Delta t \leq \left(\frac{1}{\Delta x^2} + \frac{1}{\Delta y^2} + \frac{1}{\Delta z^2} \right)^{-1/2}, \quad (3.25)$$

with c the speed of light. On a 2D grid with equal grid sizes $\Delta x = \Delta y = \delta$, the requirement given in Eq. (3.25) reduces to

$$\frac{\Delta t}{\delta} \leq \frac{1}{c\sqrt{2}}. \quad (3.26)$$

In the code IPF-FDMC, the stability is assured by setting $\Delta t/\delta = 0.5/c$. This value is commonly used in FDTD codes [63].

The code will be mainly used to investigate coupling between different types of waves and the subsequent power deposition in the plasma, where collisions act usually as a damping mechanism. These applications of the code necessitate a method to measure the deposited power. To this end, a second calculation grid, referred to as *reference grid*, is added to which the same antenna field is applied as to the first grid. The reference wave encounters no obstacle on its grid, corresponding to propagation in vacuum, and is absorbed shortly after leaving the antenna plane. The reference grid can be kept small, usually the size of one wavelength is used in each dimension (plus the appropriate size of the absorbers). It is now possible to compare the power deposited in the absorbers on both grids. From the difference of these two power values, the exact value of the dissipated power on the main grid can be calculated.

Furthermore, the code allows the distinguish between ingoing and outgoing wave, which is equivalent to a directional coupler. A second calculation grid is necessary, on which no reflection of the ingoing wave is allowed to occur. By calculating the difference between the main grid and the second grid, the outgoing wave can then be obtained.

So far, only the modeling of a cold plasma has been introduced. The O–X mode conversion is correctly described in this approximation, as will be shown in Sec. 3.3.1. To successfully describe the X–B mode conversion, the cold plasma approximation needs to be modified to include warm plasma corrections. This has been done first in the ion frequency range in order to describe the linear mode conversion taking place at the so-called ion-ion hybrid resonances [65, 66]. This approach has then been transferred to the electron cyclotron frequency range to remove the singularity at the UHR and in order to describe the X–B conversion. In the code IPF-FDMC, the approach of Ram *et al.* [43] is used if the X–B conversion needs to be taken into account. This method is briefly described in the following paragraph.

Assuming \mathbf{B}_0 to be directed along the z -axis, and the density gradient along the x -axis, then, according to Ref. [43], an additional term in the x -component of the plasma current, Eq. (3.24), can be introduced:

$$J_x \rightarrow J_x - \frac{d}{d\xi} \left(\sigma_{\text{Ram}} \frac{dE_x}{d\xi} \right), \quad (3.27)$$

with $\xi = \omega x/c$ and

$$\sigma_{\text{Ram}} = \frac{-3X}{(1-Y^2)(1-4Y^2)} \left(\frac{v_{th,e}}{c} \right)^2, \quad (3.28)$$

$v_{th,e} = \sqrt{k_B T_e / m_e}$ is the electron thermal velocity and X, Y are defined in Eq. (2.38).

This approximation correctly describes the X–B mode conversion and the propagation of the EBW in the vicinity of the UHR. However, as the EBW propagates away from the UHR towards the cyclotron harmonics, this approximation breaks down, since only the dominant first-order term in the Larmor radius expansion is considered.

Another FDTD code, similar to IPF-FDMC, has been developed by C. Lechte at IPF. It is called IPF-FD3D and deals with the simulation of reflectometry in fusion plasmas [67].

3.3 Application of the code IPF-FDMC

3.3.1 1D simulations: O–X mode conversion

As a first check of the code’s reliability, the O–X conversion efficiency is calculated for a 1D geometry and compared with the approximation given in Eq. (2.41) that is valid within the limits of geometrical optics.

The simulation is carried out for TJ-II parameters. TJ-II is a medium size stellarator in Spain [68], where the O–X–B heating scheme was optimized using IPF-FDMC [44]. A constant background magnetic field of $B_0 = 0.87$ T points into the z -direction, and the density variation is along the x -axis with a density gradient length of $L_n = 4\lambda_0$. In order to achieve maximum conversion efficiency, the incident beam needs to have the optimum value of N_z , see Eq. (2.40), and, furthermore, the elliptical polarization as described in Eq. (2.49). In this experiment, the condition for the normalized density gradient length, $k_0 L_n \gg 2\pi$, is fulfilled and corrections to Eq. (2.49) need not be considered [40, 69].

An obliquely incident beam in a 1D coordinate system is realized making use of Snellius’ law (e. g. [70]), which states that the N_z component is conserved since there is no variation in this direction. Obviously, the k_z component is also conserved, which can then be introduced as a constant in the FDTD scheme.

Figure 3.2a shows a comparison of the conversion efficiency η obtained from full-wave calculations on the one hand and results from Eq. (2.41) on the other hand. The parallel refractive index N_z has been varied keeping $N_y = 0$. For the simulation, the grid size has been set to $\delta = \lambda_0/64$. As one can clearly see, excellent agreement is found, confirming earlier results obtained with the full-wave code COLSYS [40].

Figure 3.2b shows the dependence of the conversion efficiency on N_y with $N_z = N_{z,opt}$. Again, excellent agreement is found between the simulations and the formula from Mjølhus.

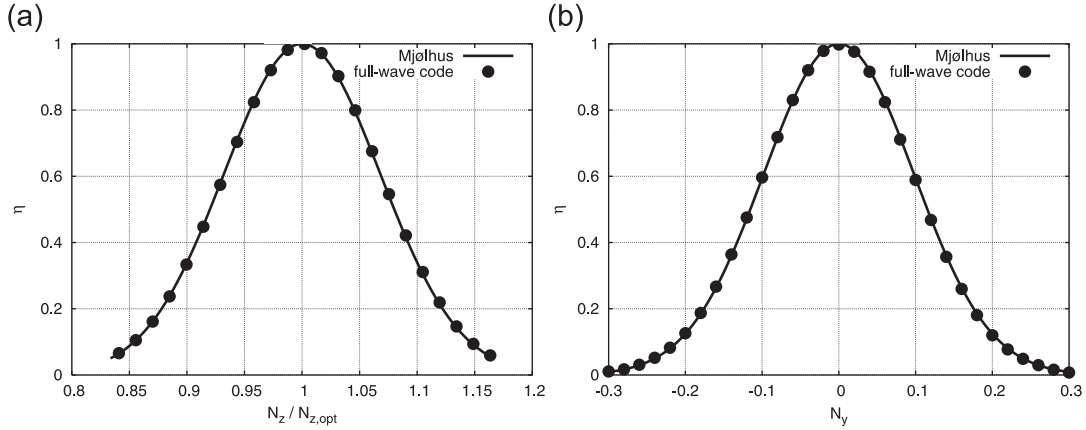


Figure 3.2: (a) O–X conversion efficiency as a function of the normalized refractive index $N_z/N_{z,opt}$ at $N_y = 0$. Solid line corresponds to Eq. (2.41), circles from simulations with IPF-FDMC. (b) O–X conversion efficiency as a function of N_y at $N_z = N_{z,opt}$, the same notation as in (a). (The figure is also published in Ref. [44].)

It is an inherent feature of the FDTD code that it describes the temporal evolution of the wave field. This allows for the instructive possibility to monitor the temporal development of the O–X mode conversion process. For demonstration purposes, a simulation has been carried out with a very shallow density profile, so that the distance between the O–X conversion layer and the UHR is about 20 vacuum wavelengths. Furthermore, the grid resolution has been increased by a factor of 2 and the constant magnetic field has been set to $Y = 0.67$. Figure 3.3 shows the temporal development of an O-mode that is incident from vacuum with $N_z = N_{z,opt}$. Hence, perfect conversion efficiency is achieved in this simulation. Shown are four snapshots of the wave electric field, where the time is given in the lower left side of each graph. The upper curve in each graph represents the wave electric field while for the lower curve in each graph the numerical directional coupler is used, to extract the outgoing wave, only. The positions of the UHR and the conversion layer ($X = 1$) are depicted by dashed lines in the graphs.

In the first snapshot, taken after 100 oscillation periods T_{wave} , the wave has not yet reached the O-mode cutoff. No outgoing wave is detected on the directional coupler at this time. In the second snapshot, taken after 200 oscillation periods, the wave has reached the cutoff, and the increase in the wavelength close to the cutoff is clearly visible. There is also a first indication of the generated SX-mode behind the cutoff layer. This can be seen more clearly in the next snapshot, taken after 250 oscillation periods. Here, a short-wavelength structure can be recognized that propagates to the left. This is the SX-mode. On the numerical directional coupler, only the short-wavelength SX-mode is visible. At the last snapshot, taken after 350 oscillation periods, the interference pattern between the ingoing O-mode and the outgoing SX-mode can be seen in the wave electric field. The numerical directional coupler shows only the outgoing SX-mode, demonstrating perfect conversion effi-

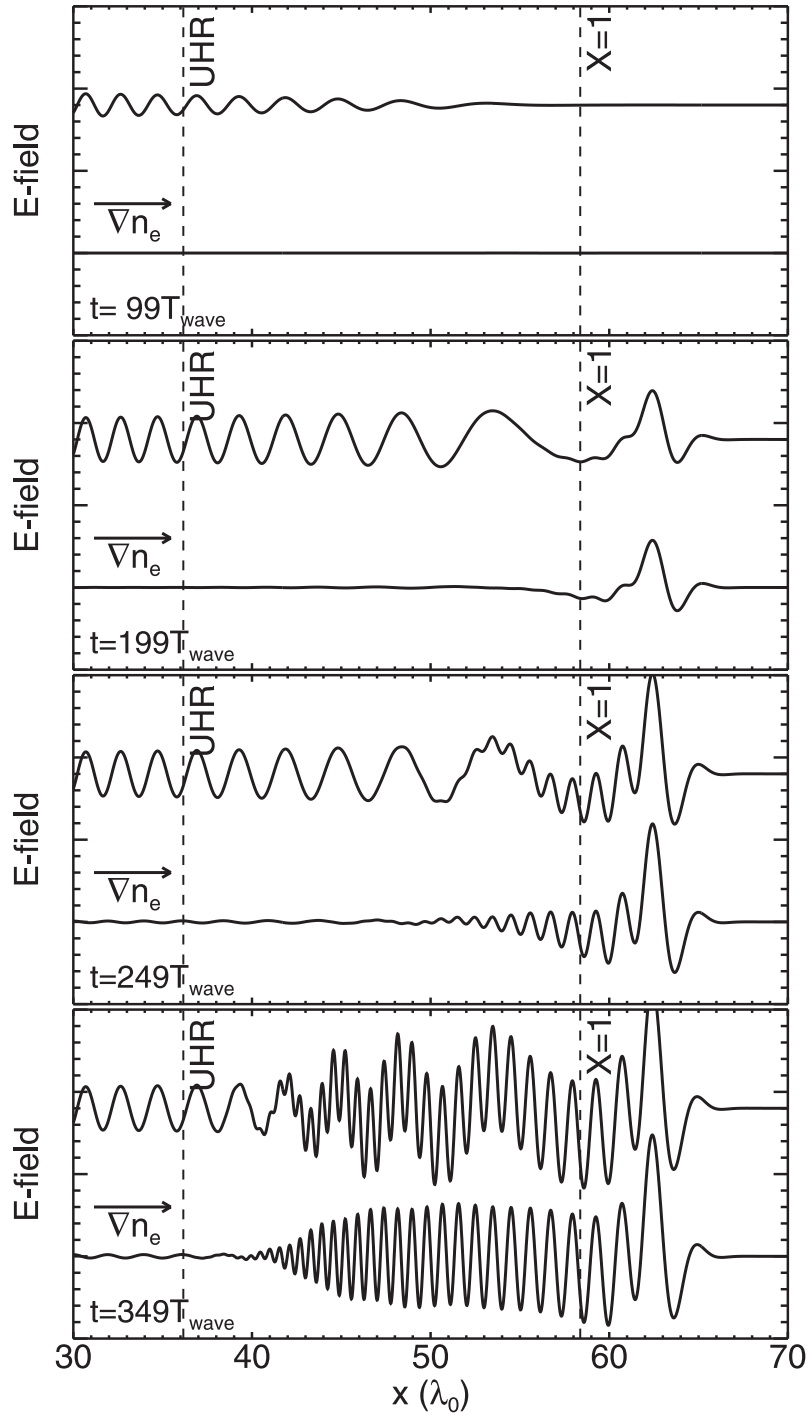


Figure 3.3: 1D simulation with IPF-FDMC of the O–X mode conversion process, where an O-mode with $N_z = N_{z,opt}$ is incident onto a plasma. The process is illustrated at four different stages, where the respective time is given in the lower left of each graph. The upper curve represents E_x , while the lower curve shows the output of the numerical directional coupler that shows only the outgoing E_x . One can clearly see, how the mode conversion process happens over a finite space and a finite time and that the generated SX-mode has a shorter wavelength than the incident O-mode.

ciency. In the vicinity of the UHR the electric field of the SX-mode would increase without limit if no dissipation takes place. In practise, damping of the resonance will occur through collisions, linear mode conversion or parametric decay [16]. To resolve the singularity at the UHR, in the code two types of loss mechanisms were tested, firstly, the collision term in Eq. (3.24) and secondly an artificial viscosity. The latter acts preferentially on the short-wavelength components. It is implemented as being proportional to the second derivative of the electric field. For example, for the E_x component at the position x_1 the damping term reads

$$\nu_{\text{visc}} = \alpha_{\text{visc}} \frac{1}{\delta} \left(\frac{E_x(x_1 + 1) - E_x(x_1)}{\delta} - \frac{E_x(x_1) - E_x(x_1 - 1)}{\delta} \right), \quad (3.29)$$

where α_{visc} is a constant, defining the strength of the damping. Hence, the viscosity scales as

$$\nu_{\text{visc}} \sim E_x(x_1 + 1) + E_x(x_1 - 1) - 2E_x(x_1). \quad (3.30)$$

For short wavelengths, ν_{visc} has a much higher value than for long wavelengths, as can be deduced from Eq. (3.30). Hence, the numerical viscosity acts predominantly close to the UHR, where it is needed to resolve the singularity with $k \rightarrow \infty$ and $\lambda \rightarrow 0$.

As stated in the context of simulations for the TJ-II stellarator [44], both dissipation mechanisms lead to the same results: Within a realistic parameter range for both damping mechanisms the dissipated energy and the concomitant energy transfer converge. This agrees with theoretical expectations stating that the details of the dissipation mechanisms are not important to calculate the value of the resulting loss [42]. In the code IPF-FDMC, both loss mechanisms can indeed be varied over several orders of magnitude without influencing the conversion efficiency. Only if the normalized collision frequency exceeds values of $\nu/\omega_0 \geq 10^{-3}$ or if the normalized numerical viscosity exceeds values of $\alpha_{\text{visc}}/\omega_0 \geq 10^{-2}$, damping along the propagation path becomes non-negligible.

Three important facts concerning the O–X mode conversion and the concomitant transfer of energy are illustrated by the simulation results shown in Fig. 3.3:

- The O–X conversion takes a finite time to develop.
- The O–X conversion takes place over a finite region behind the O-mode cutoff.
- The wavelength of the resulting SX-mode is shorter than the vacuum wavelength ($v_{\text{phase},SX} < v_{\text{vacuum}}$).

3.3.2 1D simulations: X–B mode conversion

In the simulations shown in Fig. 3.3, the SX-mode needed a dissipation term when it approaches the UHR. If the warm plasma correction to the cold plasma approx-

imation is included, as discussed in Sec. 3.2.5, the singularity at the UHR is automatically resolved by mode conversion and thus energy transfer of the SX-mode into the EBW.

For demonstration purposes the code allows to separate the X–B mode conversion from the O–X mode conversion. The simulation is started with a SX-mode, which is now excited close to the conversion layer, where it is supposed to have been generated by an O-mode. Due to the expected short wavelength of the EBW (see Sec. 2.3 for details) the resolution of the simulation grid needs to be strongly increased: the grid size is set to $\delta = \lambda_0/1000$.

For steep density gradients the distance between the UHR and the R-cutoff can get short enough that the wave can tunnel through this evanescent layer (see Fig. 2.7). This leads to a direct coupling of the SX-mode to the FX-mode, which then leaves the plasma without contributing to the desired heating process. According to Budden’s analysis [42], this mechanism can become important, if the width of the evanescent region is on the order of 10 % of the wavelength and below. For an evanescent layer wider than this value, complete conversion into EBW can be assumed, neglecting other loss mechanisms (see also Sec. 2.4.1). Here, the density profile is set to be sufficiently shallow to suppress this effect.

The full-wave code IPF-FDMC is used to illustrate the temporal development of the X–B mode conversion process. Figure 3.4 shows four snapshots of the X–B mode conversion process. The time is given in units of oscillation periods in the upper left corner of each graph. In each snapshot, the upper and the lower curves represent the longitudinal and transversal components of the wave electric field, respectively. The large longitudinal component, which characterizes the EBW, is scaled down by a factor of 40 as compared with the transversal component.

In the first snapshot, taken after 150 oscillation periods, the SX-wave has reached the UHR layer. At the UHR the wavelength gets shorter and a longitudinal electric field component develops. In the second snapshot, taken after 500 oscillation periods, a strong amplification of the longitudinal component can be seen (notice the different scaling by a factor of 40). The longitudinal component is seen to have a shorter wavelength. After 1000 oscillation periods, corresponding to the next snapshot, a new wave with a very short wavelength can be clearly seen. This is the EBW. The next snapshot, taken after 1500 oscillation periods, corresponds to the time, where the viscous damping mechanism starts to act on the EBW, which now has a short enough wavelength. One can see that the EBW has no noticeable transverse component and is, thus, an electrostatic wave. Obviously, with the modification of the cold plasma model, described in Sec. 3.2.5, the X–B mode conversion can be successfully modeled with the FDTD code.

The main conclusions drawn from the illustration of the X–B mode conversion process in Fig. 3.4 are the following:

- The X–B conversion takes several hundreds of oscillation periods to develop.
- The resulting EBW has a very short wavelength.

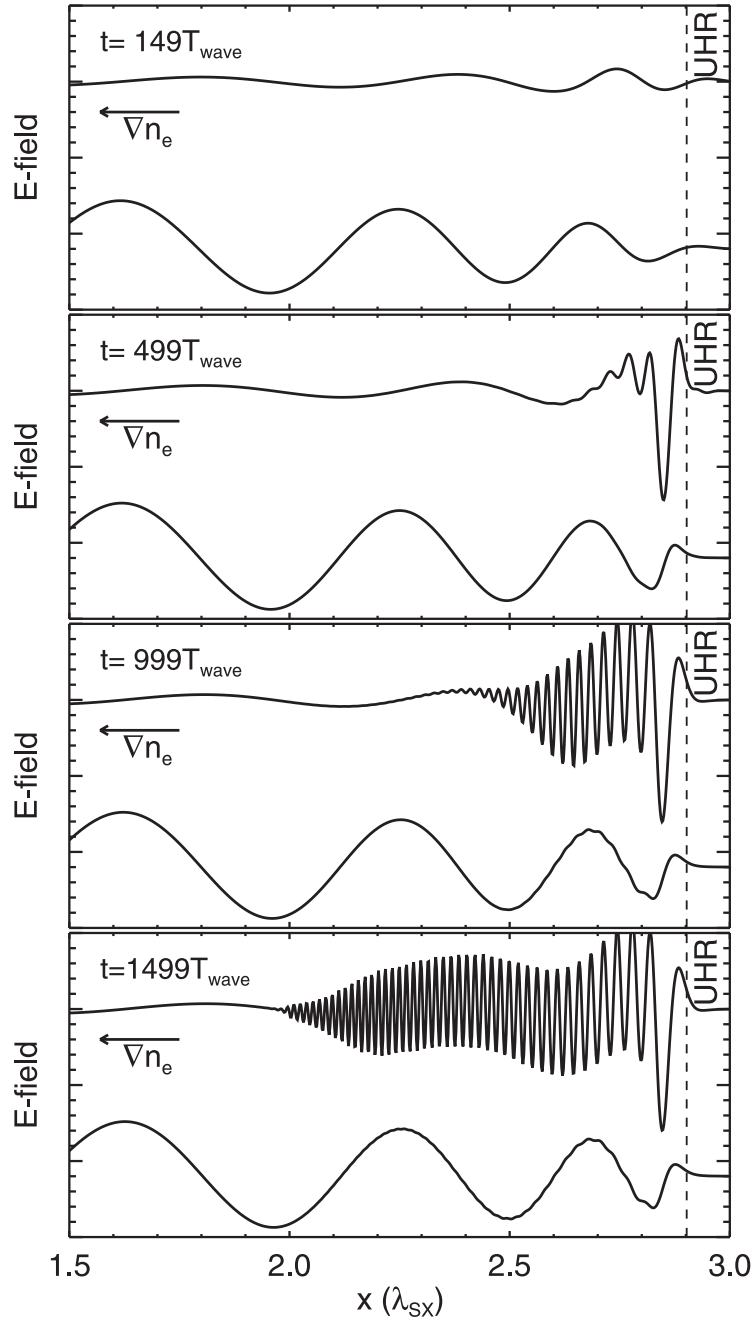


Figure 3.4: 1D simulation with IPF-FDMC of the SX-B mode conversion process, where an SX-mode is incident from the high density region onto the UHR. The process is illustrated at four different stages, where the respective time is given in the upper left of each graph. The lower curve represents the transversal wave electric field E_y , while the upper curve represents the longitudinal wave electric field E_x . One can see, how the short-wavelength EBW takes almost 1000 oscillation periods to develop.

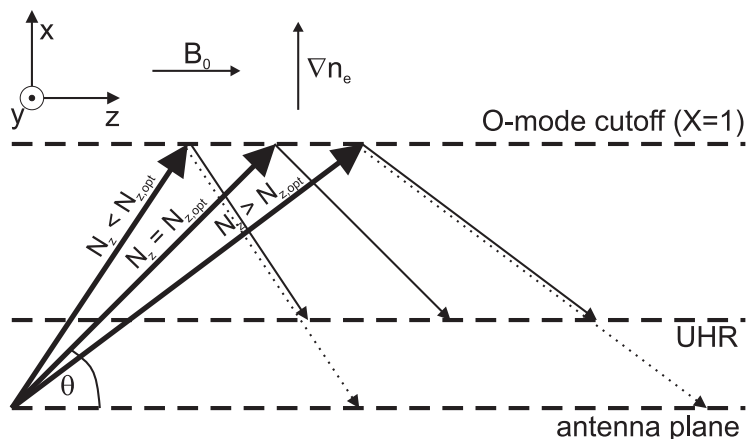


Figure 3.5: Slab geometry used in the calculations discussed in Sec. 3.3.3. Shown are one ray with the optimum value $N_z = N_{z,opt}$ and two rays with non-optimum values of N_z ; thick line depicts the launched ray, thin line depicts the mode-converted ray, dotted line depicts the unconverted ray. (The figure is also published in Ref. [44].)

- The resulting EBW is an electrostatic wave.

3.3.3 Deterioration of the conversion efficiency in 2D

By extending the simulation to a 2D grid, effects of the plasma geometry and the antenna become important. To illustrate the 2D effects, the results from an optimization study [44] of the O–X–B heating scenario for the stellarator TJ-II, which were done with the code IPF-FDMC, will be presented here. First, the effect of finite beam size, i. e. “non-plane” waves, will be discussed. Then, the effect of curved conversion layers will be illustrated.

Effect of finite beam size

Figure 3.5 shows a sketch of the geometry used in the simulations in this section, where the coordinate system, the direction of \mathbf{B}_0 and of the density gradient are defined. In the antenna plane, the ingoing and outgoing powers, P_{in} and P_{out} are detected. Note that the unconverted power arrives at different positions in the antenna plane, depending on the value of N_z . The ratio of P_{in} and P_{out} defines the conversion efficiency. Care has been taken that no power can reach the other boundaries of the calculation grid. Three rays are plotted in graph, each representing an O-mode with a different value for N_z . The ray with $N_z = N_{z,opt}$ is fully converted into an X-mode, which is then, at the UHR, absorbed without reaching the antenna plane. Note that for $N_z < N_{z,opt}$ and $N_z > N_{z,opt}$ both the partially converted component of the incident power (absorbed at the UHR) and the unconverted component (reaching the antenna plane) are shown.

Figures 3.6 and 3.7 show examples of the 2D simulations for Gaussian beams with

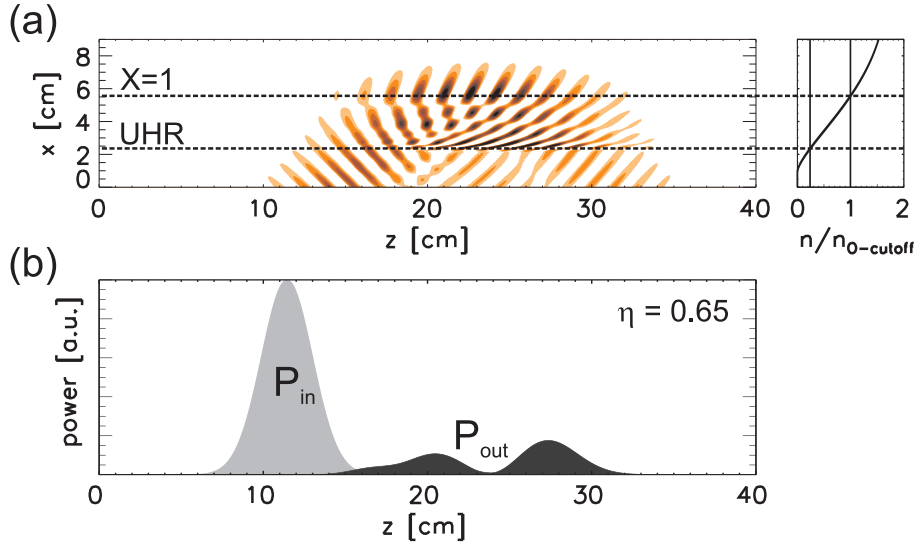


Figure 3.6: (a) Radial E -field distribution (E_x) for a Gaussian beam with a beam size of $w_0 = 2\lambda_0$. For clarity, only $E_x > 0$ is shown. The normalized density profile is shown on the right side, the positions of the O–X conversion layer and the UHR layer are indicated with dashed lines. (b) Envelope of incident antenna power P_{in} and outgoing (non-converted) power P_{out} in the antenna plane. (The figure is also published in Ref. [44].)

beam sizes $w_0 = 2\lambda_0$ and $w_0 = 4\lambda_0$, respectively. The beams are incident with the angles corresponding to optimum conversion efficiency. Similar to the 1D simulations shown in Fig. 3.3, one can see the O–X conversion occurring over a *finite* radial region close the cutoff layer at $X = 1$. The wavelength of the generated X-mode becomes shorter as it approaches the UHR and the direction of propagation turns continuously into the direction perpendicular to \mathbf{B}_0 . Simultaneously, the electric field component E_x increases.

At the bottom of the figures are shown the envelopes of the ingoing and outgoing power distributions in the antenna plane. P_{out} has a double-hump distribution in the toroidal direction. For $N_z \neq N_{z,opt}$ the incident power is only partially converted. The minimum in the reflected power, situated between the two humps, indicates that the power fraction of the incoming Gaussian beam with the optimum value of $N_z = N_{z,opt}$ is almost perfectly converted at the O–X conversion layer and consequently absorbed at the UHR layer.

Obviously, the wider beam shown in Fig. 3.7 has the narrower spectrum in N_z (see e.g. Ref. [71] for a comprehensive overview on Gaussian beam properties) and therefore the non-converted components, i. e. the two humps, are less pronounced. Note that the measurement of the spatial distribution of the outgoing power can serve to diagnose the details of the conversion process in an actual experiment. For the wider beam the conversion efficiency has increased from $\eta = 0.65$ (at $w_0 = 2\lambda_0$) to $\eta = 0.86$ (at $w_0 = 4\lambda_0$). This is due to the smaller beam divergence for the wider beam.

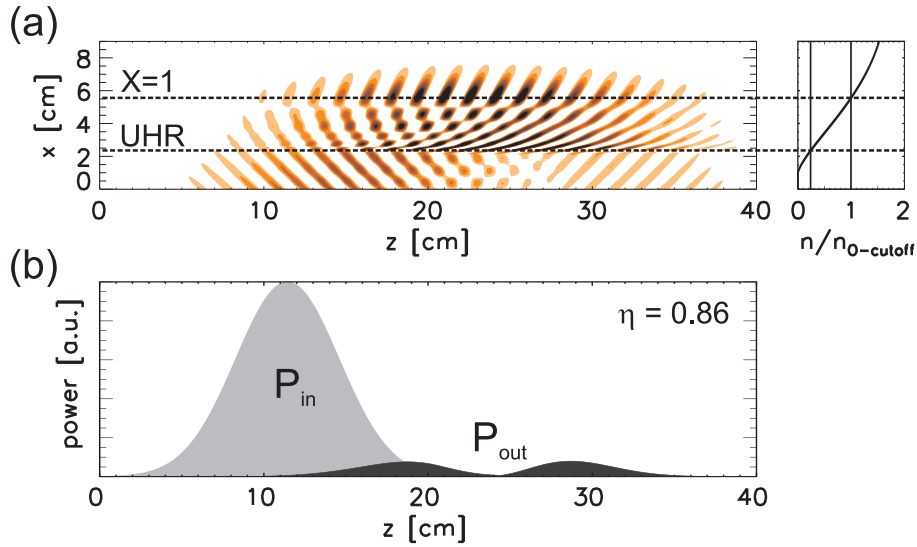


Figure 3.7: Same as Fig. 3.6, but for a broader beam, $w_0 = 4\lambda_0$. (The figure is also published in Ref. [44].)

In Ref. [44], the influence of the beam size on the conversion efficiency was scanned over a wide range, and it was found, as expected, that in the limit of $w_0 \rightarrow \infty$ the beam becomes a plane wave with $\eta = 1$.

Effect of curved conversion layers

Clearly, in a toroidal plasma experiment, the consequences of curved conversion layers on the conversion process need to be considered. As a first step in the simulations, both magnetic field lines and surfaces of constant density are taken to be curved in the xz -plane, while there is still no variation in the y -direction. See Fig. 3.5 for the definition of the coordinate system. Fig. 3.8 shows the electric field distribution for the same incident beam as in Fig. 3.7. Due to the curvature, the conversion efficiency now drops from $\eta = 0.86$ to $\eta = 0.52$.

To restore a high conversion efficiency, the case of a focussed beam is considered, with its beam waist outside the antenna plane. Moving the waist away from the antenna plane into the plasma results in a converging beam whose phase fronts, also denoted as wavefronts, are curved at the antenna plane. Numerically, focussing of the antenna beam is realized by a parabolic phase variation at the antenna. Optimum conversion efficiency is found if the wavefront perfectly matches the curvature of the O–X conversion layer. In general, it is found that wavefront matching is less effective for smaller beams, because it cannot fully compensate the effect of the corresponding larger divergence [44]. As a consequence, the beam size should always be made as large as possible within the given technical constraints.

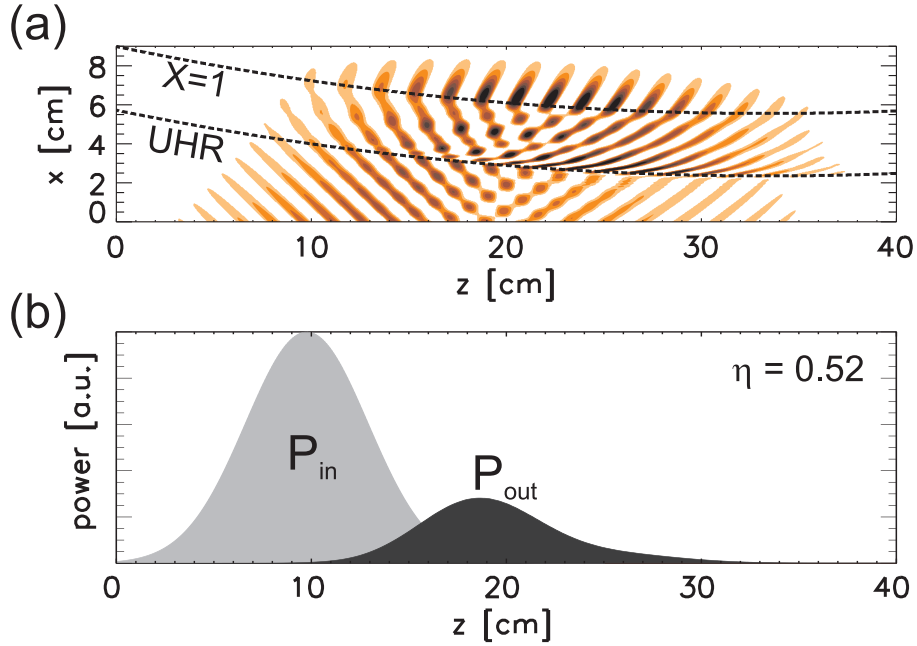


Figure 3.8: Same as Fig. 3.7, but for the slab with finite curvature. (The figure is also published in Ref. [44].)

3.3.4 Simulations of the O–X–B mode conversion in 2D

In Secs. 3.3.1 and 3.3.2, the O–X–B mode conversion process has been divided into the O–X and the X–B parts and both processes have been treated separately in a 1D geometry. Here, the complete O–X–B conversion process is illustrated in a 2D geometry.

The background parameters correspond to the geometry of the TJ-II plasma, where an O–X–B heating system is currently being installed [44]. The background magnetic field is aligned to the x -axis with a value of $B_0 = 0.87$ T and the density gradient is aligned to the y -axis, as shown in Fig. 3.5. These values correspond to the finite spatial region in TJ-II, where the mode conversion is expected to occur. A Gaussian beam is injected with a beam size of $w_0 = 4\lambda_0$; the frequency of the microwave is 28 GHz.

Figure 3.9 shows a closeup of the conversion region at three different moments, with the time indicated in terms of oscillation periods in the upper left corner of each graph. The positions of the UHR and the O-mode cutoff are indicated by dashed lines. For clarity, only positive values of the wave electric field component E_x are plotted, negative values are suppressed. In the first snapshot, Fig. 3.9a, one can see the O-mode, which is incident from the lower left side at the optimum angle. In the second snapshot, taken after 40 oscillation periods, the O–X conversion has already started. It can be clearly seen that the conversion happens over a finite region around the O-mode cutoff. The X-mode then reaches the UHR, and its wavelength shortens. In the third snapshot, taken after 195 oscillation periods, the

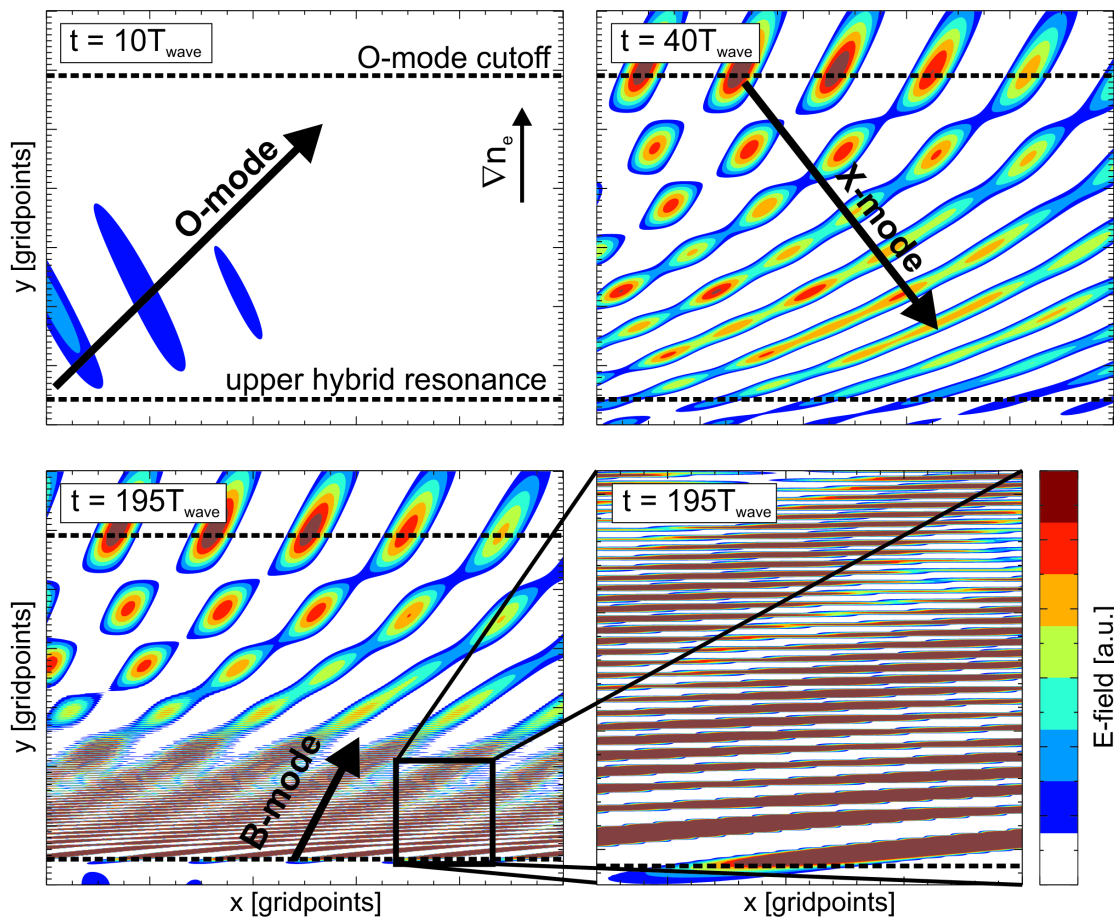


Figure 3.9: A zoom into the conversion region of the complete O–X–B mode conversion process, which is delineated by illustrations of the respective stages at three different points in time, the time is indicated in each of the graphs. Only $E_x > 0$ is shown. At $t = 10 T_{\text{wave}}$ the incident O-mode has crossed the UHR but not yet reached the cutoff. After $t = 40 T_{\text{wave}}$ the O–X conversion has started and the X-mode is approaching the UHR. After $t = 195 T_{\text{wave}}$ one can see the generated EBW propagating towards higher densities. (The figure is also published in Ref. [72].)

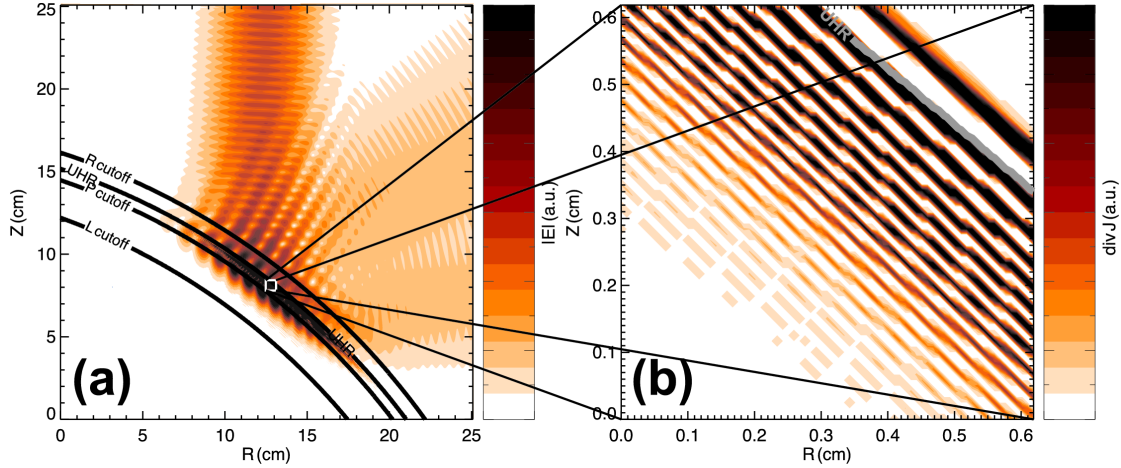


Figure 3.10: Simulation result obtained with IPF-FDMC for the experiment RFX-mod: (a) Absolute value of the wave electric field for an O-mode incident so that maximum O–X mode conversion efficiency is achieved; cutoffs and resonances are labeled in the plot. (b) Details of the EBW generated via mode conversion at the UHR. (The figures are also published in Ref. [45].)

X–B conversion has started and the extremely short wavelength of the EBW can be seen. This is emphasized by the lower right plot, which shows a detail of the X–B conversion region of the third snapshot.

Thus, with the full-wave code IPF-FDMC, the temporal development of the complete O–X–B mode conversion process could be nicely illustrated. The different length scales of the waves as well as the long timescale necessary for the mode conversion have been made visible. The complete sequence can be observed as a short movie¹ in Ref. [44].

In Fig. 3.9, the EBW is illustrated by showing the wave electric field of the incident microwave. It can be identified by its predominantly longitudinal character. The EBW is an electrostatic wave that is sustained by the movement of electrons. Hence, its electrostatic character can also be visualized by plotting the divergence of the current density, since

$$\text{div } \mathbf{J} \sim \tilde{n}_e. \quad (3.31)$$

This method has been used in simulations carried out during a feasibility study of EBW coupling via O–X–B mode conversion for the RFX-mod reversed field pinch in Padua (Italy) [45, 73]. Figure 3.10 illustrates simulation results carried out with IPF-FDMC during this study. On the left hand side, a snapshot of the absolute value of the wave electric field is plotted for a microwave beam that is incident in such a way that the conversion efficiency has its maximum value. On the right hand side, a

¹In Ref. [44], this mode conversion process is attached as a multimedia enhancement, which shows a video, in which the EBW can be furthermore identified directly as a backwards propagating wave (phase and group velocity are directed antiparallel with respect to each other).

zoom into the region around the UHR is shown. Here, $\text{div } \mathbf{J}$ is plotted and one can clearly see the EBW with its small wavelength propagating away perpendicularly to the X–B conversion layer.

An advantage of this representation can be immediately seen, when comparing it with Fig. 3.9: The signal of the incident O-mode, traversing the UHR, does not appear in the plots when showing $\text{div } \mathbf{J}$. With this type of representation, the EBW can be identified easily.

In the simulations for RFX-mod it was shown that the inclusion of the vacuum vessel geometry is necessary to correctly describe the experiment: The conversion efficiency *without* the vessel walls included was found to be approximately 50 %, while it was found to be 70 % *with* the vessel walls included in the simulations [73].

3.4 Summary

The full-wave code IPF-FDMC is an implementation of the Yee-algorithm with the inclusion of an expression for the plasma current. It is a fluid code that can handle all the effects occurring in cold plasma theory, e.g. O–X mode conversion. With an additional term in the expression for the current density, X–B conversion can also be treated.

On a 1D grid, the O–X and the X–B conversion have both been simulated with the code, revealing important features of the conversion processes. A shortening of the wavelength is observed in both processes and both were found to occur over a region of finite spatial width. The finite time interval needed for mode conversion is especially pronounced in the X–B conversion, which takes several hundreds of oscillation periods to fully develop. The electrostatic character of the EBW could also be demonstrated.

The code has been successfully applied to the TJ-II stellarator in order to optimize the O–X–B mode conversion scenario. During that study, the full O–X–B mode conversion process has been calculated on the 2D grid for the first time with a code based on the FDTD-method.

Next, a feasibility study of O–X–B mode conversion for the RFX-mod reversed field pinch has been carried out, during which the inclusion of the metal walls in the calculation was shown to be mandatory to correctly represent the experiment. The single pass absorption was found to be in the order of only 50 %, which could be increased by including the metal walls to 70 %, due to reflections of the microwave at the walls and multiple subsequent traverses across the conversion layer.

Hence, the code has been proven to be a reliable and robust tool to simulate wave-plasma interaction. In the following chapters, it will be used to investigate the microwave heating in TJ-K.

Chapter 4

The stellarator TJ-K

The stellarator TJ-K is the device on which all experiments discussed in this thesis have been carried out. It will be described in this chapter together with the diagnostics used in the experiments.

4.1 TJ-K

TJ-K is a stellarator of the type torsatron which has been constructed and operated in Madrid under the name TJ-I U [74, 75, 76, 77]. In 1999 it has been moved to the university of Kiel and was renamed TJ-K [11]. Whereas TJ-I U was operated in pulsed discharges with plasmas that reached electron temperatures $T_e \geq 100$ eV, TJ-K is operated in long discharges with low-temperature plasmas, $T_e \leq 20$ eV. In 2006, TJ-K was moved to the university of Stuttgart.

The relevance of low-temperature plasmas as the one in TJ-K for fusion research is given by the possibility of scaling dimensionless parameters of these plasmas to the conditions at the edge of high-temperature fusion plasmas [12, 78, 79].

4.1.1 Geometric configuration

The major and minor radii of TJ-K are $R_0 = 0.6$ m and $\langle a \rangle = 0.1$ m, respectively. The vessel is made of stainless steel 316L and has a wall thickness of about 1 cm and a magnetic permeability of $\mu_r \leq 1.05$ [11]. TJ-K is shown in Fig. 4.1 at the different locations where it was operated. From the three pictures in the figure one can see that TJ-K offers very good access to the inside of the vessel: 18 flanges of the type DN 250 ISO-K and 6 flanges of the type DN 63 ISO-K are equally distributed along the torus. The arrangement of the flanges is defined by the helical field coil which winds six times around the torus: six small flanges are located at the inner side of the torus, and six big flanges each at the top, outer and bottom side of the torus.

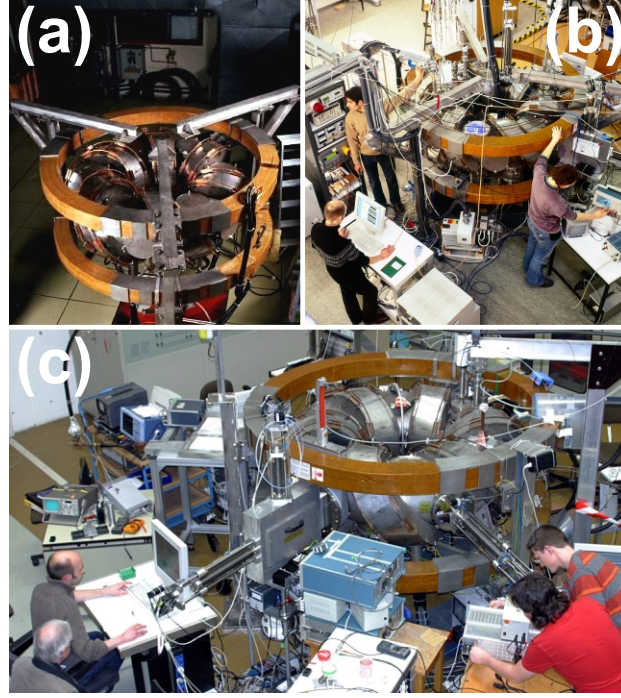


Figure 4.1: The stellarator TJ-K at the different laboratories, where it was operated: (a) CIEMAT, Madrid (b) IEAP, University of Kiel (c) IPF, University of Stuttgart.

4.1.2 Magnetic configuration

The magnetic field in TJ-K is provided by two vertical field coils and one helical coil ($l = 1$), which winds helically six times ($m = 6$) around the torus. This results in a six-fold symmetry of the magnetic field geometry. The winding of the helical coil follows the law [80]

$$\phi = 1/6 (\theta + 0.4 \sin \theta), \quad (4.1)$$

where ϕ is the toroidal and θ the poloidal angle.

Following one magnetic field line and connecting all intersection points in one poloidal cross section, defines a magnetic flux surface. The six-fold symmetry applies to the shape of the flux surfaces as well, i. e. it repeats every 60° with respect to the toroidal direction. The shape of the flux surfaces, calculated with the Gourdon code [81], is shown in Fig. 4.2. Depicted are the four toroidal positions, where the flanges are located. The solid lines refer to closed flux surfaces, whereas dashed lines refer to flux surfaces, whose magnetic field lines intersect with the vacuum vessel. They will be denoted as *open flux surfaces* in the following. The existence and the shape of the flux surfaces has been verified experimentally [82, 83].

Varying the ratio between the currents through the vertical and the helical field coils, $R_{v/h} = I_{\text{vertical}}/I_{\text{helical}}$, allows to shift the flux surfaces horizontally. The variation in $R_{v/h}$ also affects the shape of the flux surfaces. This has been investigated

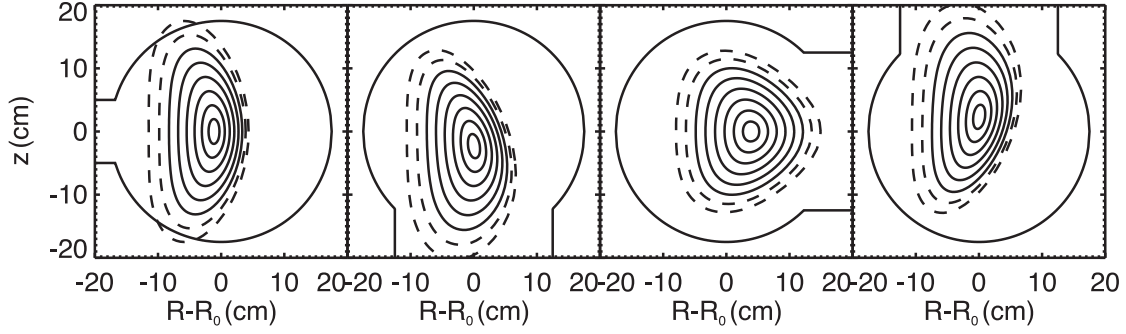


Figure 4.2: The flux surfaces in TJ-K at the different toroidal angles, where the flanges are located, corresponding to the default current ratio of $R_{v/h} = 0.57$. Closed flux surfaces are indicated by solid lines, flux surfaces which intersect with the vacuum vessel are indicated by the dashed lines.

recently in great detail [83]. For the calculated flux surfaces shown in Fig. 4.2, a current ratio of $R_{v/h} = 0.57$ has been chosen. This corresponds to the default value that is used for all the discharges presented in this thesis, if not stated differently. For the default configuration, the *rotational transform* has an average value over the poloidal cross section of $t \approx 0.3$, i. e. a magnetic field line has to complete three toroidal circumferences before one poloidal circumference is complete. An average minor plasma radius of $a = 10$ cm leads to an *inverse aspect ratio* of $\epsilon = a/R \approx 0.17$

The electrical circuit for distributing the current between the helical and the vertical field coils allows for a maximum helical current of $I_h = 1500$ A.¹ This results in an average background magnetic field of $B_0 = 360$ mT. The magnetic field strength in the poloidal cross sections, where the flanges are located, is depicted in Fig. 4.3. Starting at the flanges and going to the center of the vessel, one sees that the value of B_0 increases, i. e. all flanges are located at the low field side.

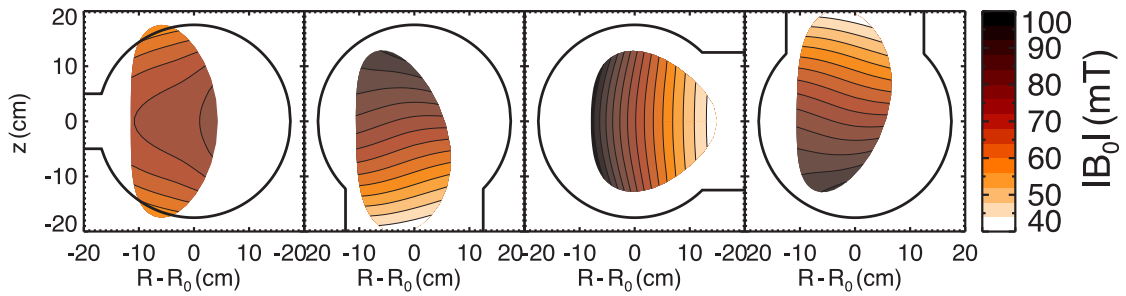


Figure 4.3: The absolute value of the background magnetic field strength in TJ-K at the four different toroidal angles, where the flanges are located, corresponding to a current of $I_h = 300$ A and the default current ratio of $R_{v/h} = 0.57$.

¹The helical field coil consists of 120 windings, and the two vertical field coils consist each of 93 windings.

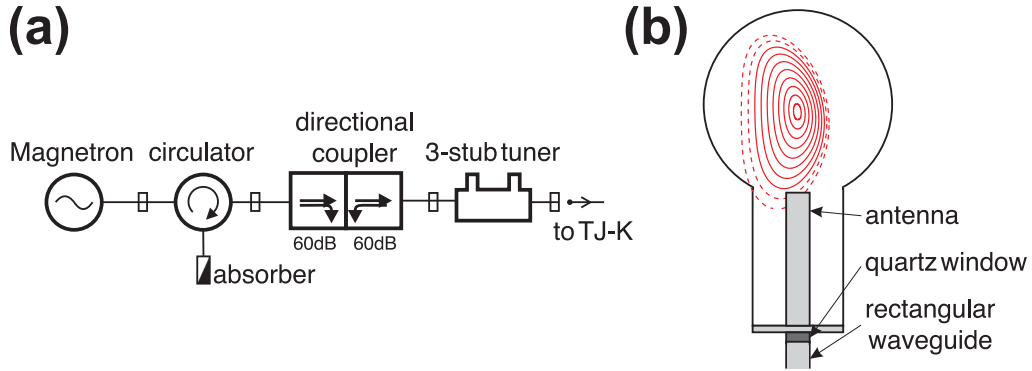


Figure 4.4: (a) Sketch of the transmission line of the 2.45 GHz microwave heating system. (b) Vertical cut through TJ-K at the bottom port B4, where the vacuum transition and the antenna are located.

4.2 Plasma heating

The plasma in TJ-K is heated by means of microwaves. Operation is possible at two different frequencies, 2.45 GHz and from 7.9–8.4 GHz. In the following two paragraphs, the configuration and the possible operational modes of the heating systems at the two different frequencies, are briefly described.

4.2.1 2.45 GHz microwave system

The microwaves at a frequency of 2.45 GHz are generated by magnetrons [84, 85]. Three different magnetrons were used in the experiments presented in this thesis: Magnetron ① can only be operated in cw mode with a maximum output power of 6 kW; magnetron ② delivers in cw mode a maximum power of 6 kW and in pulsed operation a maximum peak power of 10 kW at modulation frequencies of $50 \text{ Hz} < f_{\text{mod}} < 25 \text{ kHz}$; magnetron ③ delivers in cw mode a maximum power of 1.6 kW and at modulation frequencies of $50 \text{ Hz} < f_{\text{mod}} < 30 \text{ kHz}$ a maximum peak power of 2 kW.

The three magnetrons can be interchanged while the transmission line, shown in Fig. 4.4a, is always the same. Standard rectangular waveguides of the type *R26* are used in the transmission line. With a 3-stub-tuner (see e.g. Ref. [86] for details) the incident microwave can be matched to the plasma to minimize the reflected power. Directional couplers allow to monitor both the incident and the reflected power. As illustrated in Fig. 4.4b, a quartz window serves as vacuum transition at the bottom port B4. The antenna is mounted directly on top of the quartz window. If not stated differently, a simple rectangular cut waveguide was used in the discharges discussed in this thesis.

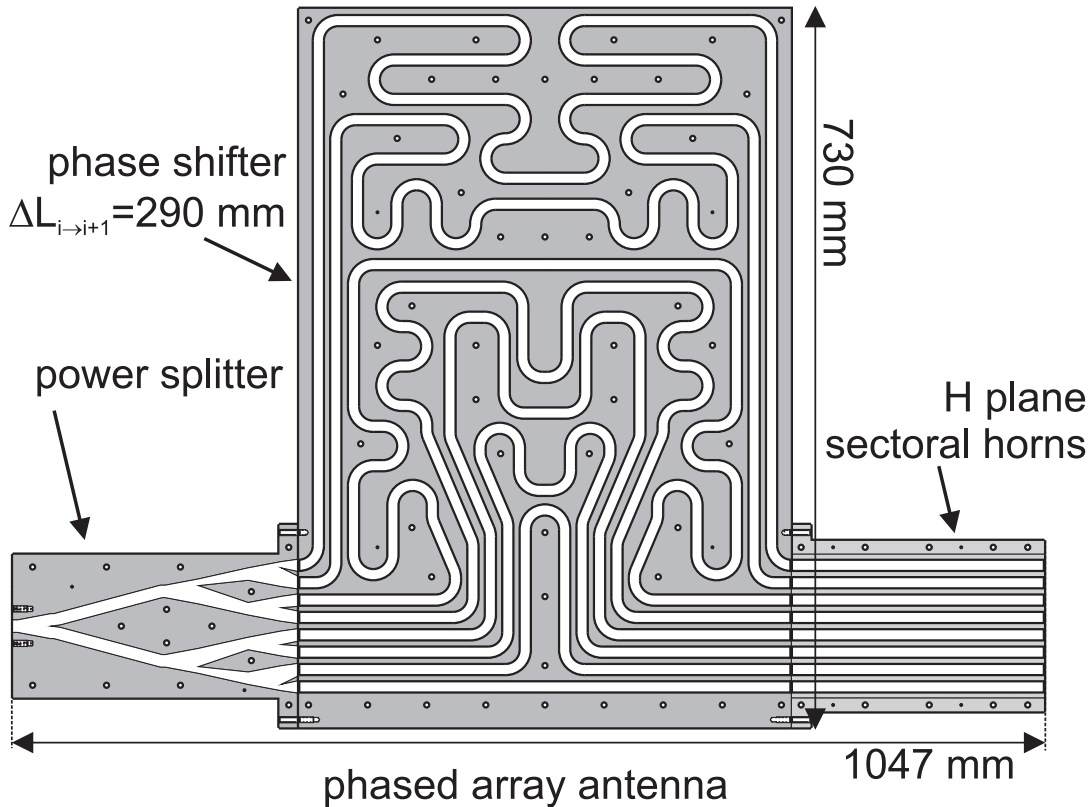


Figure 4.5: Longitudinal cut through *E*-plane of the array antenna, consisting of the power splitter, the phase shifter and the *H* plane sectoral horns. (The figure is also published in Ref. [89].)

4.2.2 8 GHz microwave system

The microwave source at the higher frequency differs from the 2.45 GHz source in the sense that it is an oscillator-amplifier system: The microwave is provided by a signal generator and then amplified by two traveling wave tube amplifiers (TWT-A) [84, 87], which are of the type VTX-6281A7. Each of the amplifying tubes is capable of delivering an output of 600 W in a frequency range of $7.9 \text{ GHz} \leq f_0 \leq 8.4 \text{ GHz}$. The TWT-A can each be operated alone or in combined operation with a maximum output power of 1200 W. The details of the different operational modes are describes in Appendix A.

A flexible waveguide, approximately 10 meters long, is used to guide the microwave to a phased array antenna, which is installed at the outer port O-1. The antenna was designed by H. Höhnle and a detailed description including the construction plans, can be found in his diploma thesis [88].

In the phased array antenna, the incoming microwave is first split up into eight channels, as illustrated in Fig. 4.5. The power distribution of the eight channels of 1:3:5:6:6:5:3:1 produces a Gaussian beam at the output. The power splitter is



Figure 4.6: Microwave lens made of PMMA acting as vacuum transition for the 8 GHz heating system.

connected to a phase shifter, realized by channels of different length, as can be seen from Fig. 4.5. Obviously, this results in a phase difference at the output of the phase shifter of the eight channels with respect to each other. Next to the phase shifter, H-plane sectoral horns [90] are mounted to each channel. At the output of the horn antennas, the phase shift of all the channels with respect to each other results in an oblique wavefront. The phase shift and, hence, the angle of incidence at the output of the phase shifter depends on the wavelength of the microwave. Hence, by sweeping the frequency, the angle of incidence can be controlled. The phase shifter is constructed in such a way that a variation in the frequency range from 7.9 to 8.4 GHz corresponds to a variation in the angle of incidence from -45° to $+45^\circ$ with respect to the antenna axis.

The vacuum transition is realized by a lens made of PMMA (also referred to as *plexiglas*) installed between the array-antenna and the outer port O-1. Using lenses in the microwave frequency regime is a widespread method [90, 91, 92]. PMMA is used as material due to its negligible dielectric losses at these frequencies [93].

The lens is designed to focus the antenna beam onto the predicted position of the O-X conversion layer. Its final shape has been defined by an optimization process with the full-wave code IPF-FDMC. As one can see in Fig. 4.6, grooves were milled into both sides of the lens, in order to minimize the reflected power of the microwave [94].

The phased array antenna is installed in such a way at TJ-K that its angle variation is in the toroidal direction. Since this corresponds basically to the direction of the magnetic field, an O-wave is incident into the plasma. According to the analysis in Ref. [88], a frequency of 8.15 GHz corresponds to perpendicular injection,

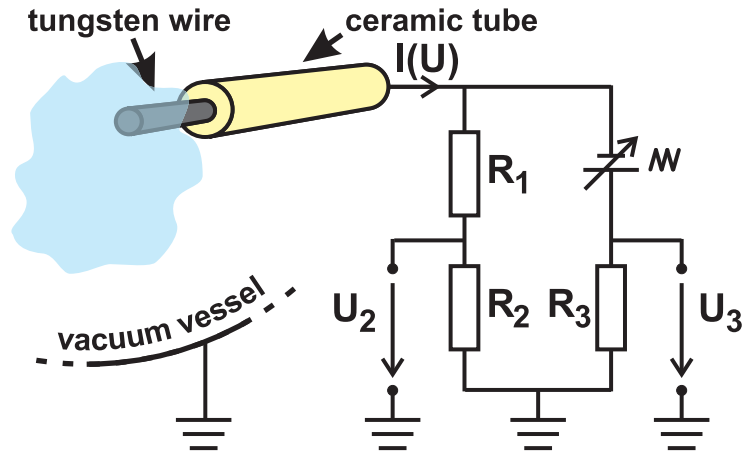


Figure 4.7: Langmuir probe and the electric circuit used for obtaining the characteristics. The values of the resistors are $R_1 = 482 \Omega$, $R_2 = 24 \text{ k}\Omega$ and $R_3 = 1 \Omega$ [99].

whereas 8.01 and 8.3 GHz correspond to the angle for optimum mode conversion efficiency and to the negative value of this angle, respectively.

4.3 Diagnostics

The diagnostics used in the experiments discussed in this theses will be briefly described in this section.

4.3.1 Langmuir probes

The Langmuir probe is a common diagnostics for low-temperature plasmas. It has been developed in the twenties of the last century by Langmuir and his coworkers [95, 96]. A great variety of textbooks exists in which the Langmuir probe in general and different realizations of it are treated in detail, e.g. [57, 97, 98]. Here, only the type of Langmuir probes which is applied in TJ-K is briefly described.

Basically, a Langmuir probe is an electrostatic probe consisting of a thin tungsten wire (typical diameter of $d = 200 \mu\text{m}$), which is insulated by a ceramic tube (Degussit AL23), as shown in Fig. 4.7. A small tungsten tip with a length in the order of 2 mm is in direct contact with the plasma. By biasing the tip, a current is drawn and the current-voltage characteristic can be acquired. Details about the electronic circuit for obtaining the characteristics at TJ-K can be found in Ref. [99]. From this characteristic, the plasma parameters electron temperature T_e , plasma density n , floating potential ϕ_{fl} and plasma potential ϕ_p can be obtained.

As can be seen from Fig. 4.8, the characteristic can be divided into three regions. In region A the probe is biased sufficiently negative, so that all ions in the vicinity of the probe are collected by it. Hence, the current saturates and is called *ion saturation current*. In region B, the bias voltage is decreased, which leads to an

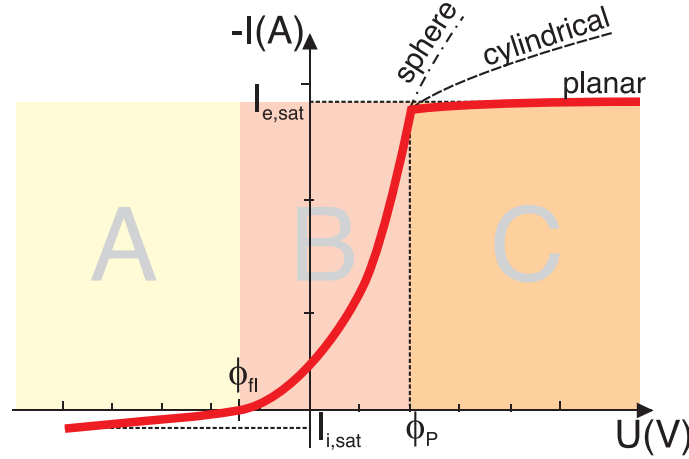


Figure 4.8: Characteristic of a Langmuir probe, red solid line corresponds to the planar probe, black dashed line to the cylindrical probe and the black dash-dotted line to the spherical probe. For historical reasons, the negative of the drawn current is plotted.

increase in the number of electrons with sufficiently high kinetic energy to reach the probe. When the electron current equals the ion current, zero net current is drawn and the probe is *floating*. The corresponding voltage is denoted as *floating potential* ϕ_{fl} . The characteristic is of exponential shape in this region until the bias voltage reaches the value of the plasma potential ϕ_p , where region C begins. Here, all electrons in the vicinity of the probe are attracted by it and the current saturates. This shape only applies to very large extended planar probe surfaces. In the experiment, mainly probes with cylindrical or spherical shapes are used, which leads to a different behavior of the characteristic in the region C, as depicted in Fig. 4.8.

The probes can be treated as planar if their spatial dimension d is large compared to the Debye length $\lambda_D = \sqrt{\epsilon_0 T_e / (e^2 n)}$: $d \gg \lambda_D$. In the limit $d \ll \lambda_D$, the orbital motion of charged particles leads to an increased distance over which electrons are attracted by the probe. This case is referred to as *orbital motion limited* theory and is described in Refs. [96, 100]. The behavior of the probes in the transition area between the two limits is described in Ref. [101].

Assuming Maxwellian electrons in a collisionless and unmagnetized plasma, the probe current derived from the simple probe theory reads [102]

$$(A) \quad I = I_{i,sat} = 0.61 en_e S \sqrt{\frac{T_e}{m_i}} \quad (4.2)$$

$$(B) \quad I = I_{i,sat} + I_e = I_{i,sat} + I_{e,sat} \exp \left\{ -\frac{e(\phi_p - U)}{T_e} \right\} \quad (4.3)$$

$$(C) \quad I = I_{e,sat} = -en_e S \sqrt{\frac{T_e}{2\pi m_e}}, \quad (4.4)$$

with m_i and m_e the ion and electron mass, respectively, and S the effective probe

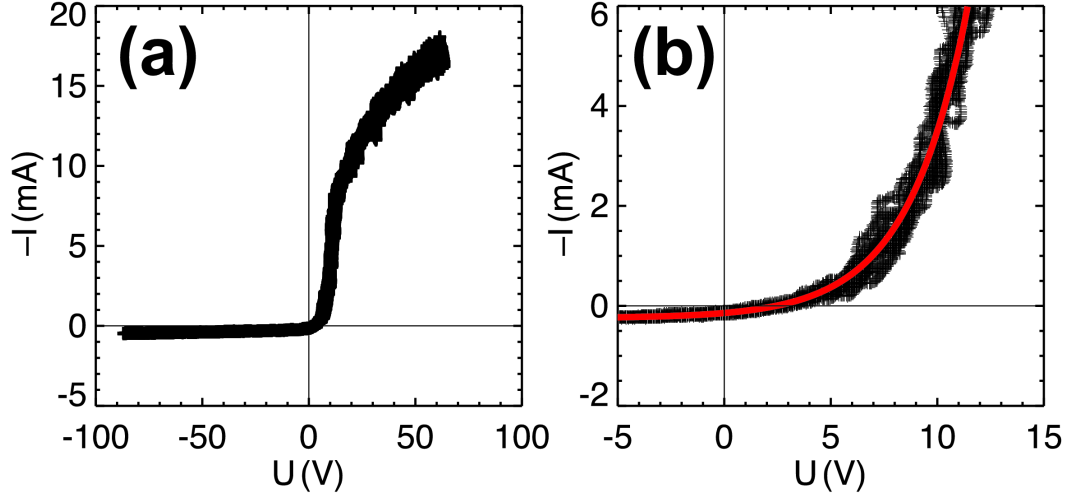


Figure 4.9: (a) Characteristic obtained with a Langmuir probe in TJ-K during an argon discharge (#6421, $R - R_0 = 6$ cm). (b) Zoom into the region, where the measured data (black crosses) is fitted to Eq. (4.6) (red, solid line).

surface.

For the probes, the plasma can be treated as unmagnetized, if the *Larmor radius*, $\rho_L = \sqrt{2mT}/(|q|B_0)$, is large compared with the spatial probe dimension d . If $\rho_L \approx d$, as in some discharges in TJ-K Eqs. (4.2)–(4.4) are still valid [103].

To obtain the plasma parameters from the characteristics, a fit to the measured data in region B is performed. If the plasma potential in Eq. (4.3) is replaced [102] by

$$\phi_p = \phi_{fl} - \frac{T_e}{e} \ln 0.61 \sqrt{2\pi m_e/m_i}, \quad (4.5)$$

the fit function reads:

$$I = 0.61enS \sqrt{\frac{T_e}{m_i}} \left\{ 1 - \exp\left(-\frac{e(\phi_{fl} - U)}{T_e}\right) \right\}. \quad (4.6)$$

The fitting procedure is realized by using the Levenberg-Marquardt algorithm [104].

A characteristic curve obtained in an argon discharge in TJ-K is shown in Fig. 4.9a. The corresponding fit using Eq. (4.6) is shown in Fig. 4.9b, the solid red line is the fit and the black crosses represent the measured data. Only the region to which the fit is applied is plotted. One can see that the fit represents the measured data very well.

To obtain plasma density profiles, one possibility consists in the measurement of the ion saturation current, since it is a function of the density. As can be seen from Eq. (4.2), the ion saturation current also depends on the effective probe surface S and on the square root of the electron temperature:

$$I_{i,sat}(r) \propto n_e(r)S(r)\sqrt{T_e(r)}, \quad (4.7)$$

with r the radial coordinate. The gradient in the background magnetic field alters the effective probe surface, since the Larmor radius ρ_L depends essentially on B_0 and a smaller value of ρ_L leads to a decreased current collected by the probe: $S(r) \propto 1/B_0(r)$. Hence, the plasma density is a function with the following form:

$$n_e(r) \propto I_{i,sat}(r)B_0(r)\frac{1}{\sqrt{T_e(r)}}. \quad (4.8)$$

To obtain the absolute values of the density profile, the ion saturation current profile is, according to Eq. (4.8), multiplied with the profile of the background magnetic field and the profile of the inverse square root of the electron temperature. Finally, the profile is normalized to the line averaged density obtained from microwave interferometry measurements (see Sec. 4.3.3). This technique avoids the difficult determination of the effective probe surface and is used for all the density profile presented in this thesis if not stated differently.

4.3.2 Monopole antennas

The microwave field is investigated by means of small antennas. Several types of small antennas have been tested. The antenna shown in Fig. 4.10 turned out to be the most robust and reliable. As one can see, the probe consists of a ceramic tube which is closed at its end and has an outer diameter of 3 mm. In order to minimize losses, a coaxial cable inside the tube, acts as antenna. At its end the insulation is stripped off so that the inner conductor is unshielded over a length of approximately 8 mm. It is a semi-flexible microwave cable (SUCOFORM_47_CU). To minimize losses of the collected signals in the GHz range, SMA connectors are used as vacuum transition.

Since one is only interested in measuring wave electric fields, the ceramic is closed at its end to avoid contact with the plasma and thus draw unwanted currents (cf. Langmuir probe). Every antenna has been checked in a test arrangement before it was used in the plasma. In this setup, the wave electric field in a rectangular waveguide was measured. The length of the antenna is smaller than the wavelength of the received electromagnetic wave (similar to antennas used in cars to receive broadcast radio signals). It belongs, therefore, to the group of short monopole antennas [105, 106]. Similar monopole antennas have been successfully used in other experiments with similar plasma parameters to investigate wave phenomena [107, 108].

Outside the vacuum vessel, the received signal is first down converted. In the case of the 2.45 GHz, a down converting amplifier (a modified KU LNC BB 2030 B) that mixes 2.45 GHz down to 275 MHz and amplifies it by 30 dB, is used. In the 8 GHz case, a similar device is used (KU LNC 8084 A), which converts 8.3 GHz down to 1.15 GHz and amplifies it by 30 dB. The output of the amplifying mixers is connected to a spectrum analyzer (Agilent E4402B).

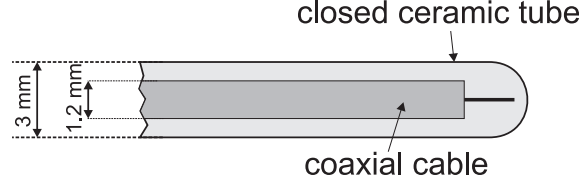


Figure 4.10: Sketch of a monopole antenna build of a closed ceramic tube and a coaxial cable whose outer insulation is stripped off at the end.

4.3.3 Microwave interferometry

A non-invasive method to obtain the plasma density via interferometry is to use electromagnetic waves in the microwave range. The frequency of the waves must be above the cutoff frequency on the path through the plasma. A *Mach-Zehnder interferometer* is such a system which has been installed at the outer port O-4 by J. Stöber [109]. It is briefly described in this section.

If an electromagnetic wave propagates through a plasma its wavelength becomes longer until the plasma density is too high and the wave is reflected. The refractive index N_{plasma} for perpendicular injection of an O-wave reads

$$N_{\text{plasma}} = \sqrt{1 - \left(\frac{\omega_{pe}}{\omega_0}\right)^2}, \quad (4.9)$$

where ω_{pe} is the electron plasma frequency and ω_0 refers to the frequency of the wave. Obviously, the refractive index depends essentially on the plasma density. The plasma density can be measured as follows: the wave is split up into two branches before it reaches the plasma: one traverses the plasma and the other not, acting as the reference branch. The phase shift $\Delta\varphi$ of the signal, which has passed the plasma with the length L , depends only on the electron density n_e :

$$\Delta\varphi = \frac{\omega_0}{c_0} \int_0^L (N_{\text{reference}} - N_{\text{plasma}}) dl \approx \frac{\omega_0}{2c_0 n_c} \bar{n}_e L, \quad (4.10)$$

with c_0 the speed of light in vacuum, n_c the cutoff density at which the wave is reflected and $\bar{n}_e = \int_0^L n_e(l) dl$ the line averaged density.

In TJ-K an interferometer with a frequency of $f = 64$ GHz is used. The corresponding cutoff density $n_c \approx 5.1 \cdot 10^{19} \text{ m}^{-3}$ is well above the densities in TJ-K which reaches maximum values of $n_e \approx 10^{18} \text{ m}^{-3}$. The two microwave signals with $f = 64$ GHz are mixed down to 60 MHz and the phase shift φ is obtained. Assuming a plasma width of 17 cm at the toroidal position where the interferometer is installed, the line averaged density can finally be calculated from

$$\bar{n}_e \approx 3.883 \cdot 10^{15} \text{ m}^{-3} \cdot \varphi, \quad (4.11)$$

where φ is taken to be in degrees.

4.3.4 Laser-induced fluorescence

Laser-induced fluorescence (LIF) is a well approved diagnostic for investigating ions in low temperature plasmas [110]. An intense laser beam excites a single ionized argon from a metastable state. Then, the fluorescent emission from the back-transition into the ground state, which has a different wavelength, provides information on the ion velocity distribution function, from which the ion temperature and the ion mean velocity can be calculated.

Such a LIF system has been set up by S. Enge [111]. A laser with an output power of 25 mW at 668.6 nm is used to excite argon ions from the state $3d^4F_{7/2}$ to $4p^4D_{5/2}$. The fluorescence light at 442.7 nm is emitted from the decay to the state $4s^4P_{3/2}$ and detected with a photo multiplier tube. The system was successfully used at the double plasma device FLIPS [111, 112], located also at IPF, and at TJ-K [113]. It is possible to measure the ion temperature with an error as small as 0.02 eV. The LIF diagnostics is limited to the investigation of *argon* ions.

In addition to LIF, passive spectroscopy is used to measure the temperature of other ions and of the neutral gas. To this end, an Echelle spectrometer [114] is available on TJ-K.

Chapter 5

Heating plasmas at low magnetic field

In this chapter the production and heating of plasmas at low magnetic field is described. The term *low magnetic field* refers to field strengths, at which the electron cyclotron frequency $\omega_{ce}/(2\pi)$ is resonant with the microwave frequency of $f_0 = 2.45$ GHz somewhere in the plasma. One of the magnetrons operating at this frequency is used as heating source. These sources are described in detail in Sec. 4.2.1.

5.1 Plasma breakdown

A power-modulated 2.45 GHz microwave source was used to study the initial breakdown of the plasma. It was modulated with a square wave at a frequency $f_{\text{mod}} = 100$ Hz and a duty cycle of 0.5. The 2-dimensional probe array SPIDER, described in detail in Refs. [115, 116], was used for measurements of the ion saturation current. As one can see in Fig. 5.1, 32 Langmuir probes are distributed over the whole poloidal cross section. The flux surfaces for $R_{v/h} = 0.57$ at $\phi = 30^\circ$ are indicated by red lines in the plot. Solid lines correspond to closed flux surfaces and dashed lines to flux surfaces, whose magnetic field lines intersect with the vacuum vessel. SPIDER consists of eight probe arms, with four probes on each arm, as shown on the right hand side of Fig. 5.1. The probe array was installed at the outer port O2.

A fast data acquisition system with a sample rate of 1 MHz allows for the investigation of plasma breakdown in the entire poloidal cross section. With time traces of typical lengths of the order of 1 min, averaging over a long series of power modulation periods is possible, which improves the signal-to-noise ratio. Here, an acquisition time of half a minute and a modulation frequency of $f_{\text{mod}} = 100$ Hz was chosen, which results in 50 acquired modulation periods. Time traces of the modulation signal of the incident microwave power and of the ion saturation current for an inner Langmuir probe of SPIDER are shown in Fig. 5.2. One can see, how the plasma density, which is proportional to the ion saturation current, reacts to the

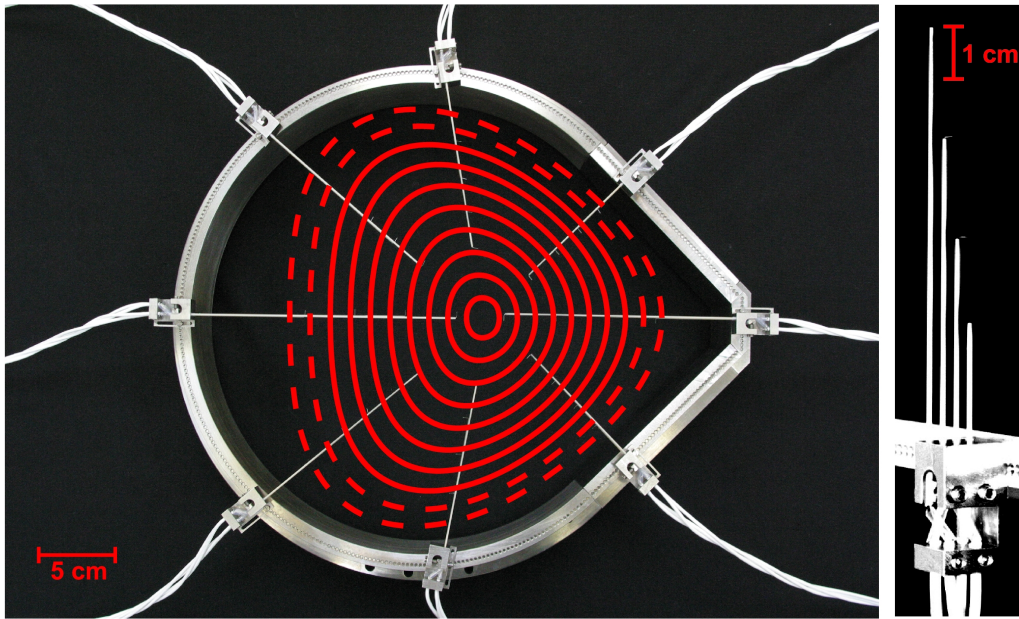


Figure 5.1: Langmuir probe array SPIDER, flux surfaces are indicated by red lines. The array consists of eight probe arms, which each consists of four Langmuir probes, as shown on the picture on the right-hand side [115].

modulated heating power. Using higher values of f_{mod} would mean that the plasma density cannot reach its asymptotic value, corresponding to the equilibrium profile. It would also result in a residual density at the beginning of the switch-on phase, which disturbs the breakdown investigations. A value of $50 \text{ Hz} < f_{\text{mod}} < 100 \text{ Hz}$ turned out to be appropriate. For the time traces shown in Fig. 5.2, the modulation frequency was set to $f_{\text{mod}} = 100 \text{ Hz}$.

Figure 5.3 shows the temporal evolution of the poloidal density profile during a hydrogen discharge. Six snapshots are shown, starting at $t = 21 \mu\text{s}$ after the microwave power was switched on up to $t \approx 1 \text{ ms}$, when the equilibrium profile is established. The geometry of the flux surfaces, the position of the cyclotron resonance layer and the position of the probe tips are indicated in the graphs. Up to a time of $40 \mu\text{s}$, the density is produced close to the resonance layer. Then, up to about $200 \mu\text{s}$, the plasma fills the flux surface due to parallel transport and a hollow density profile is achieved. At this time, the position of maximum density starts to shift away from the resonance to the plasma center. This process is visible in the graphs for $t = 230 \mu\text{s}$ and $t = 280 \mu\text{s}$. As will be discussed later in detail, it is due to the fact, that the power is now coupled to the plasma at the upper-hybrid resonance layer. After about 1 ms the typical equilibrium shape with a centrally peaked density profile has developed.

The position of the electron cyclotron resonance layer can be shifted by changing the background magnetic field. This allows to check that the breakdown really occurs at the resonance layer. In Fig. 5.4, the breakdown of a hydrogen discharge is shown,

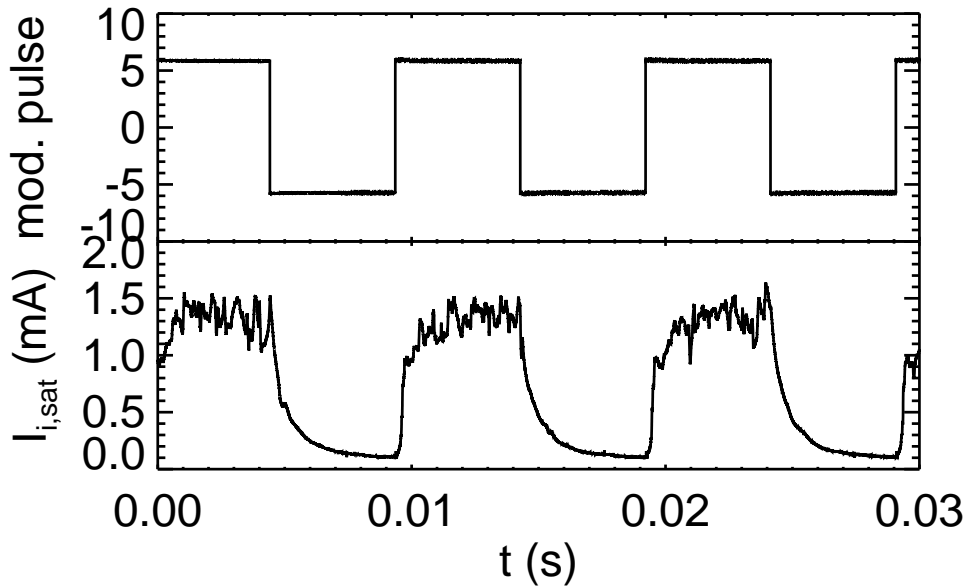


Figure 5.2: Time traces of the modulation signal of the microwave power (top) and of the ion saturation current (bottom) of one of the inner Langmuir probes of the multiple probe array SPIDER. The signals were obtained during a hydrogen discharge (#4723). The scatter in the ion saturation current signal is due to density turbulence.

in which B_0 has been changed in such a way, that the cyclotron resonance layer intersects the magnetic axis. One can clearly see, how the position of the breakdown is shifted accordingly. Similar results were obtained for the other working gases.

It is not possible to start a plasma if the cyclotron resonance is located outside the confinement region. This clearly illustrates that the existence of the cyclotron resonance layer is mandatory for the plasma breakdown to occur.

5.2 Equilibrium profiles

The shape of the equilibrium profiles is basically the same for all working gases. Figure 5.5 shows the poloidal profiles of the ion saturation current, the electron temperature and the floating potential of an argon discharge. These values were obtained using the 2D movable Langmuir probe system. To account for finite gyro-radius effects, the ion saturation signals are corrected according to the local strength of the background magnetic field, as described in Sec. 4.3.1.

As was already apparent in the build-up phase of the profiles, shown in Sec. 5.1, a centrally peaked density profile is achieved. The shape of the electron temperature profile is hollow with maximum values in the region near to the separatrix. Since the electron temperature profile reflects the microwave power deposition profile, this

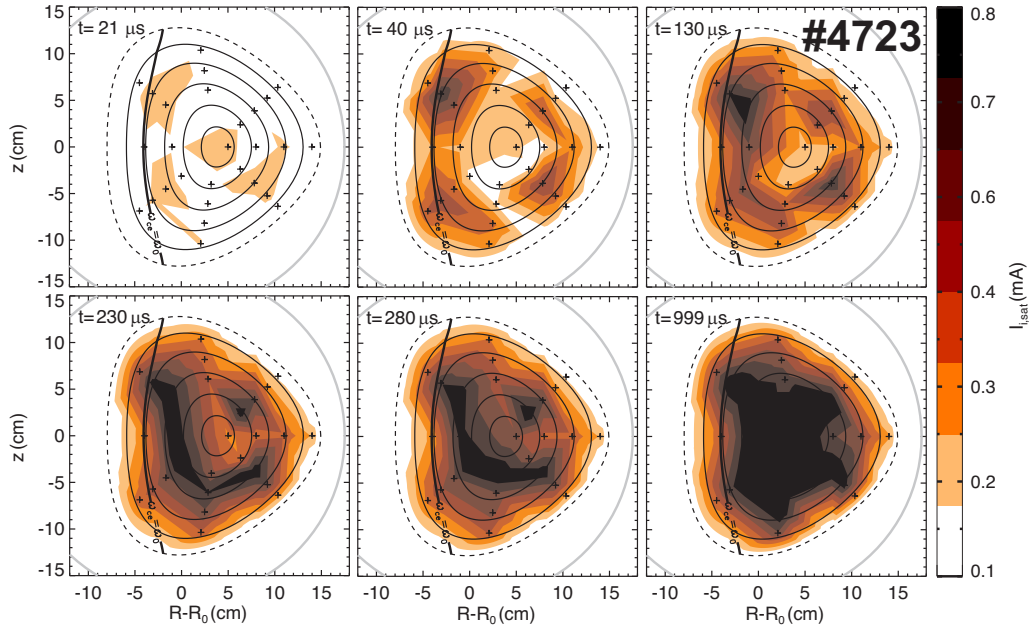


Figure 5.3: Plasma breakdown as a time series for a hydrogen discharge ($B_0 = 72 \text{ mT}$). Shown is the ion saturation current obtained from Langmuir probes located at the + signs. The time after switch-on of the microwave is indicated in the upper left side of the graphs. The flux surfaces are indicated as well as the fundamental resonance layer, $\omega_{ce} = \omega_0$. One can clearly see that the breakdown starts at the resonance layer.

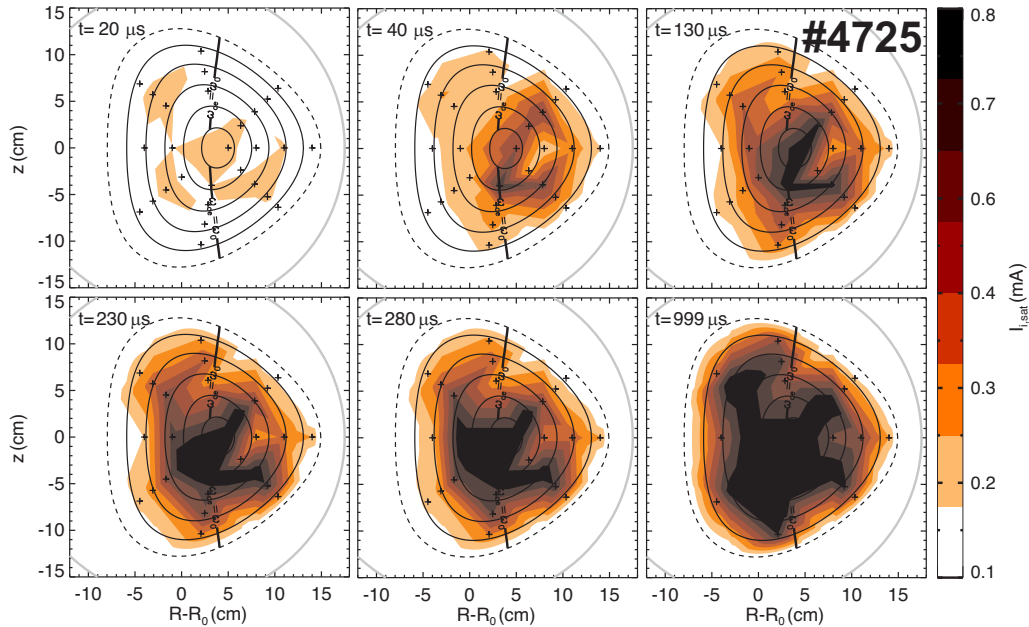


Figure 5.4: Same as Fig. 5.3, but for a higher background magnetic field, $B_0 = 96 \text{ mT}$, which results in a shift of the resonance layer into the plasma center. Again, the breakdown at the resonance can be clearly seen.

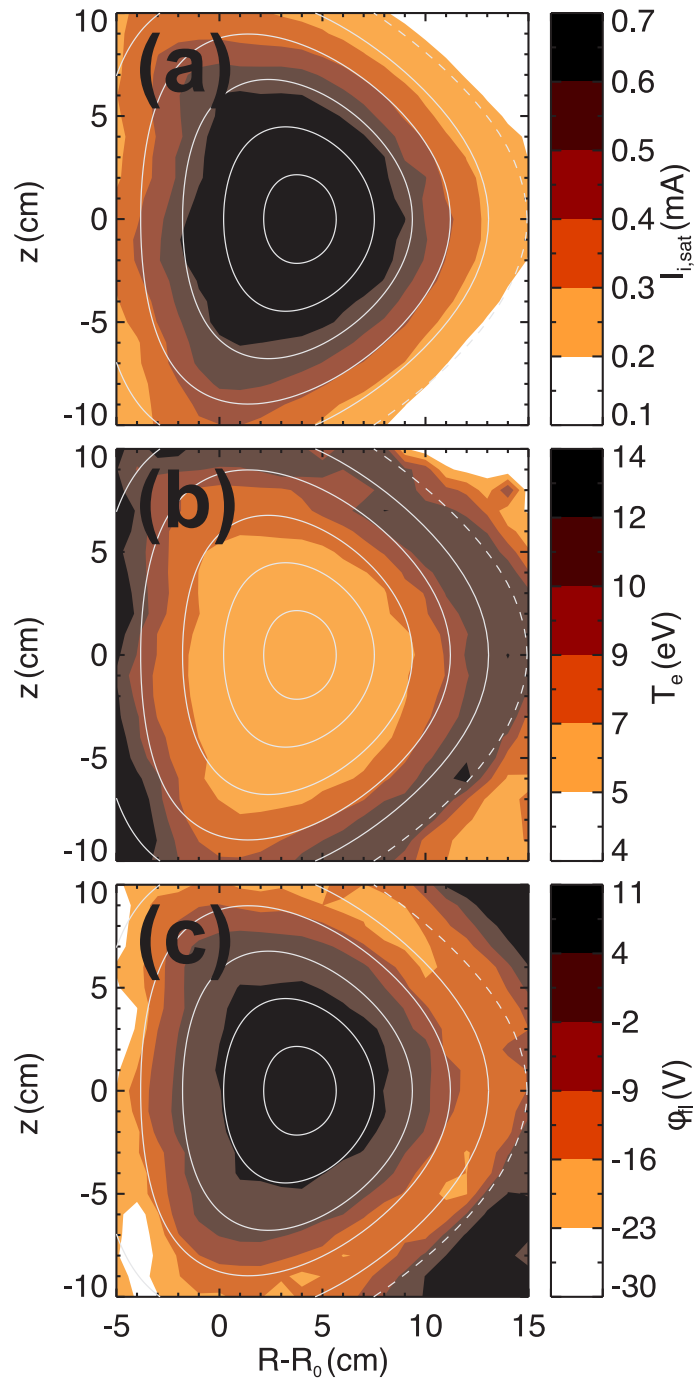


Figure 5.5: Poloidal equilibrium profiles of (a) ion saturation current, (b) electron temperature and (c) floating potential from an argon discharge (#4743) at $p_0 = 1$ mPa, $B_0 = 72$ mT and $P_{in} = 1.8$ kW injected microwave power.

indicates that the plasma in TJ-K is heated near the edge. At first sight, this seems to be in contradiction to the centrally peaked density profile. However, a combined particle and energy balance study can successfully describe the profiles as follows: Heating at the edge leads to positive electron temperature gradients and, hence, to inward heat flux. The electron heat transported to the plasma center is gradually lost due to ionization processes. Therefore, the electron temperature profile is hollow. Ionization in turn leads to an additional particle source in the plasma center. Hence, centrally peaked density profile are due to the central particle source. The particle source is balanced by outward diffusion. A particle pinch, usually used to describe the peaked density profiles in fusion plasmas with much higher ionization degrees as compared with TJ-K [117, 118], is not needed to explain the density gradient.

The profile of the floating potential has its maximum in the center of the plasma and its minimum close to the separatrix. It roughly represents the profile of the plasma potential [119]. According to Ref. [119], it can be concluded from the shape of the profile that the ions seem to be better confined than the electrons. A possible explanation for the positive radial electric field is given by losses of trapped electrons due to the curvature drift. Outside the separatrix, the magnetic field lines intersect the vacuum vessel, hence particles moving on these field lines get lost. The increasing potential could therefore be due to the higher mobility of electrons compared to ions moving along these field lines.

Comparing the shape of the equilibrium profiles from Figs 5.3 and 5.5, which were obtained during a hydrogen and an argon discharge, respectively, one can see that they are basically the same. This is also true for the other working gases.

The absolute values of the plasma density profile are obtained as described in Sec. 4.3.1. For the profile shown in Fig. 5.6a the influence of B_0 was taken into account but the electron temperature was set to a constant value, $T_e = \text{const}$. The cutoff and resonances for the microwave with $f_0 = 2.45$ GHz are indicated as contour levels in the plot. The plasma frequency layer ω_{pe} is located close to the separatrix outside of the confinement region. Therefore, the plasma can be referred to as *overdense*. The electron cyclotron resonance layer ω_{ce} is located on the very left-hand side of the plot. The resonance of the X-mode (the upper-hybrid resonance layer ω_{UH}) is located in front of the O-mode cutoff layer.

Taking into account also the influence of the electron temperature profile, slightly changes the shape of the resulting density profile. For the profile shown in Fig. 5.6b, the T_e -profile from the same discharge, shown in Fig. 5.5b, has been used. The density values in the plasma center slightly increase, whereas they decrease slightly at the edge, due to the hollow shape of the T_e -profile. Using the T_e -correction, the UHR is now situated closer to the confinement region than without the correction. Although the difference between Fig. 5.5a and 5.5b is relatively small, the influence of the T_e -profile is taken into account in the following, if the corresponding data are available.

From Figs. 5.6a, 5.6b and 5.5b, it is clearly visible that the temperature has its highest values at the UHR. This is an important result, because it indicates the

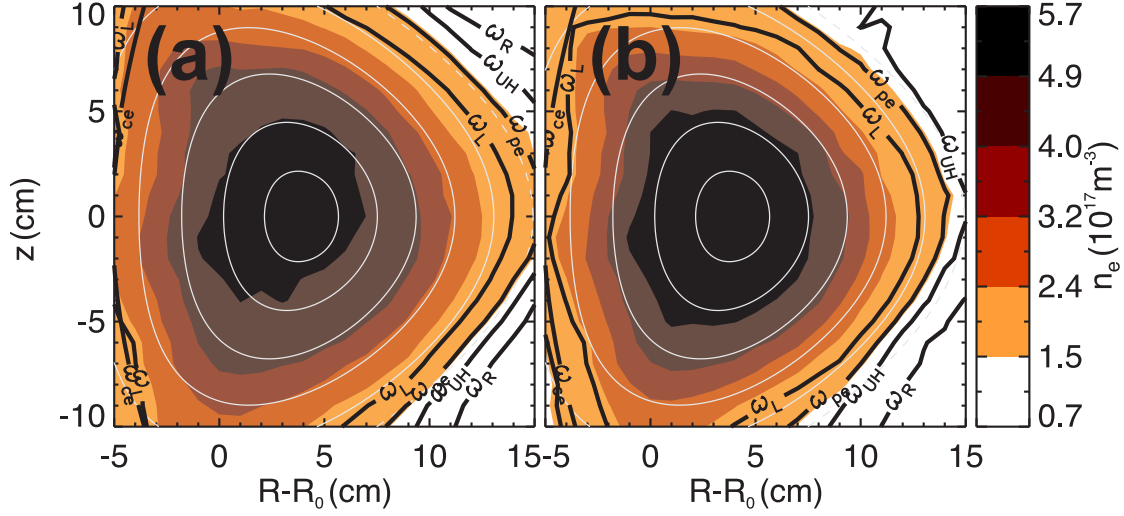


Figure 5.6: Poloidal density profile with (a) taking T_e to be constant over the whole cross section and (b) with taking into account the T_e -profile shown in Fig. 5.5b. The shape of the flux surfaces is indicated by the light gray lines and the position of the resonances and cutoffs is indicated as labeled in the graphs.

UHR as being responsible for plasma heating. However, the cyclotron resonance is still a potential candidate for plasma heating. Further investigations are therefore necessary in order to determine the respective roles of these candidates. These will be discussed in the following sections.

Another candidate is the EBW, presented in Sec. 2.3. If heating by EBW plays a dominant role in this scenario, one would expect a substantial amount of microwave power to be absorbed near the fundamental resonance layer, assuming that collisional damping of the EBW is small enough to allow for sufficient propagation away from the UHR [120]. In this case, the electron temperature profile should become centrally peaked if the fundamental resonance layer is moved to the plasma center. Since it has been experimentally checked that this is not the case [121], either heating by EBW seems not to play a dominant role in TJ-K or the effects of collisions are underestimated.

5.3 Achieved plasma parameters

In general, densities between $10^{16} \text{ m}^{-3} \leq n_e \leq 10^{18} \text{ m}^{-3}$ and electron temperatures in the range of $5 \text{ eV} \leq T_e \leq 20 \text{ eV}$ are achieved in the scenario discussed in this chapter. These values depend on the background magnetic field B_0 , the type of gas, the neutral gas pressure p_0 and the absorbed heating power P_{abs} , where P_{abs} is taken to be the difference between ingoing and reflected power, measured with a directional coupler installed in the transmission line: $P_{abs} = P_{in} - P_{out}$. The scaling of the global plasma parameters, namely line averaged density \bar{n}_e and central electron

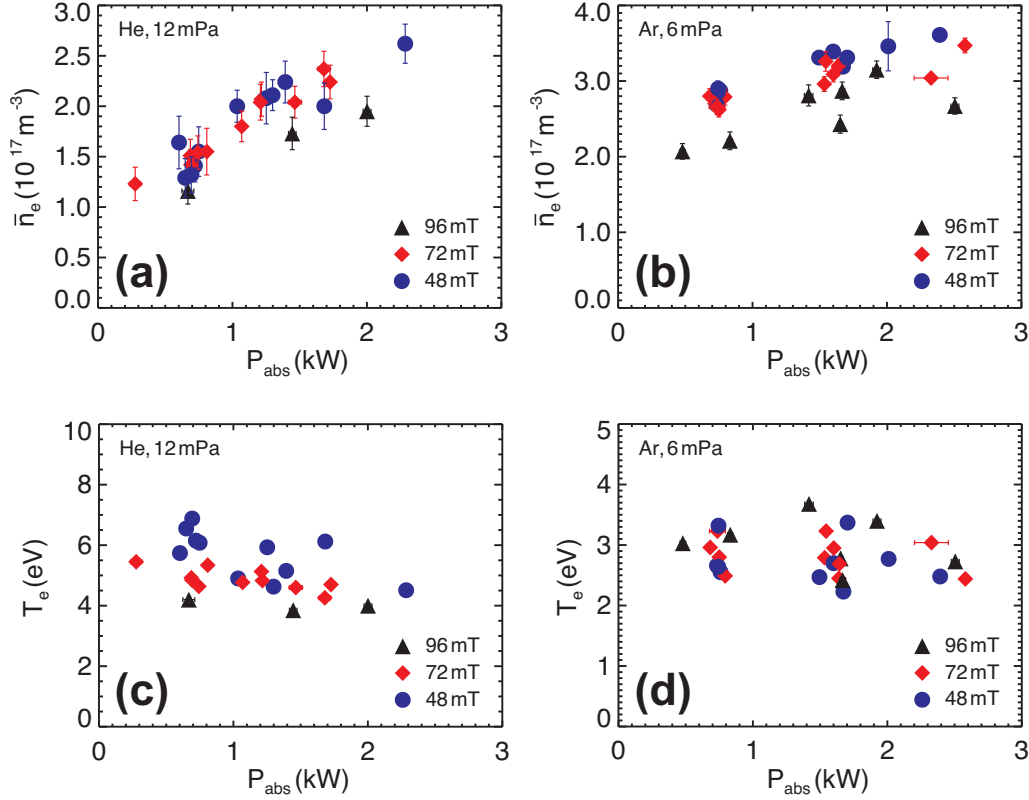


Figure 5.7: (a)+(b): Line averaged density as function of absorbed microwave power, different magnetic field strengths are indicated by different colored symbols, for (a) a series of helium discharges at $p_0 = 12 \text{ mPa}$ and (b) a series of argon discharges at $p_0 = 6 \text{ mPa}$. (c)+(d): Central electron temperature as function of absorbed microwave power for the same series of (c) helium discharges at $p_0 = 12 \text{ mPa}$ and (d) argon discharges at $p_0 = 6 \text{ mPa}$ as in (a) and (b).

temperature T_e , has been studied in a series of parameter studies.

In Figs. 5.7a and 5.7b the line averaged density is plotted as function of heating power for a series of helium discharges at $p_0 = 12 \text{ mPa}$ and a series of argon discharges at $p_0 = 6 \text{ mPa}$, respectively. The magnetic field has been varied from 48 to 96 mT. An increase of the density with increasing absorbed power can be clearly seen in both graphs for the three values of B_0 . However, for the highest values of B_0 , indicated by black triangles, lower densities are achieved than for lower values of B_0 . This is especially the case for argon. For an explanation, one must take into account the geometry of the magnetic configuration. This discussion is given at the end of this section. The dependence of the density on the heating power was found to be basically the same for all gases.

The scaling of the central electron temperature T_e for varying microwave power is shown in Figs 5.7c and 5.7d for the same discharges as in Figs. 5.7a and 5.7b. The variation in T_e is small. In helium, a small decrease with increasing heating power

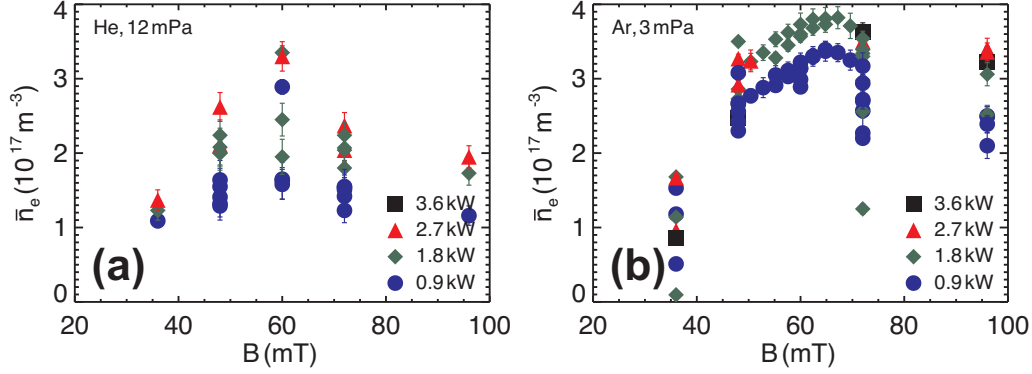


Figure 5.8: Line averaged density as function of background magnetic field strength, different colored symbols account for different heating power, for (a) a series of helium discharges at $p_0 = 12 \text{ mPa}$ and (b) a series of argon discharges at $p_0 = 3 \text{ mPa}$.

can be seen, which can be attributed to the stronger density increase. The trend that increasing heating power only leads to a small decrease in T_e was confirmed for other gases. Also apparent in the helium discharges is a trend to lower temperatures with increasing values of B_0 . In general, in argon higher densities and lower temperatures are observed than in helium.

From Figs. 5.7a and 5.7b a dependence of the plasma density on the background magnetic field can be recognized. The correlation is emphasized in Figs. 5.8a and 5.8b, where the line averaged density is shown as a function of B_0 . The helium discharges in Fig. 5.8a were obtained at $p_0 = 12 \text{ mPa}$ and the argon discharges shown in Fig. 5.8b at $p_0 = 3 \text{ mPa}$. The different colored symbols belong to different values of absorbed microwave power. The density in the helium discharges has a pronounced maximum at $B_0 = 60 \text{ mT}$. A scan with smaller steps of B_0 has been carried out for the argon discharges (Fig. 5.8b). Again, a maximum is visible, located at $B_0 \approx 67 \text{ mT}$. To understand this behavior, one has to take a look at the position of the cutoffs and resonance, which shifts radially with B_0 .

In Fig. 5.9 the 2D density profile, using Eq. (5.2) and assuming equal density values on a flux surface, is plotted at 4 different values of B_0 , increasing from Fig. 5.9a to 5.9d. The position of the cutoffs and resonances is indicated by different lines, labeled in the graphs. One can see that the cyclotron resonance layer ω_{ce} is located far outside the confinement region in Fig. 5.9a, which corresponds to the lowest value of B_0 in this series. Even, if absorption at ω_{ce} would play a role, which is not expected at the small electron temperatures (see Sec. 2.2.3 for details), the resonance would be too far outside the confinement region to contribute to plasma heating. In contrast, for the scenario with the highest value of B_0 , Fig. 5.9d, the cyclotron resonance layer is located in the center of the plasma and therefore, it is well shielded from the microwave by the plasma cutoffs located at the plasma boundary. The value of the magnetic field strength at which maximum density was found from Fig. 5.8b, is used for the plot shown in Fig. 5.9b. Here, ω_{ce} is located at

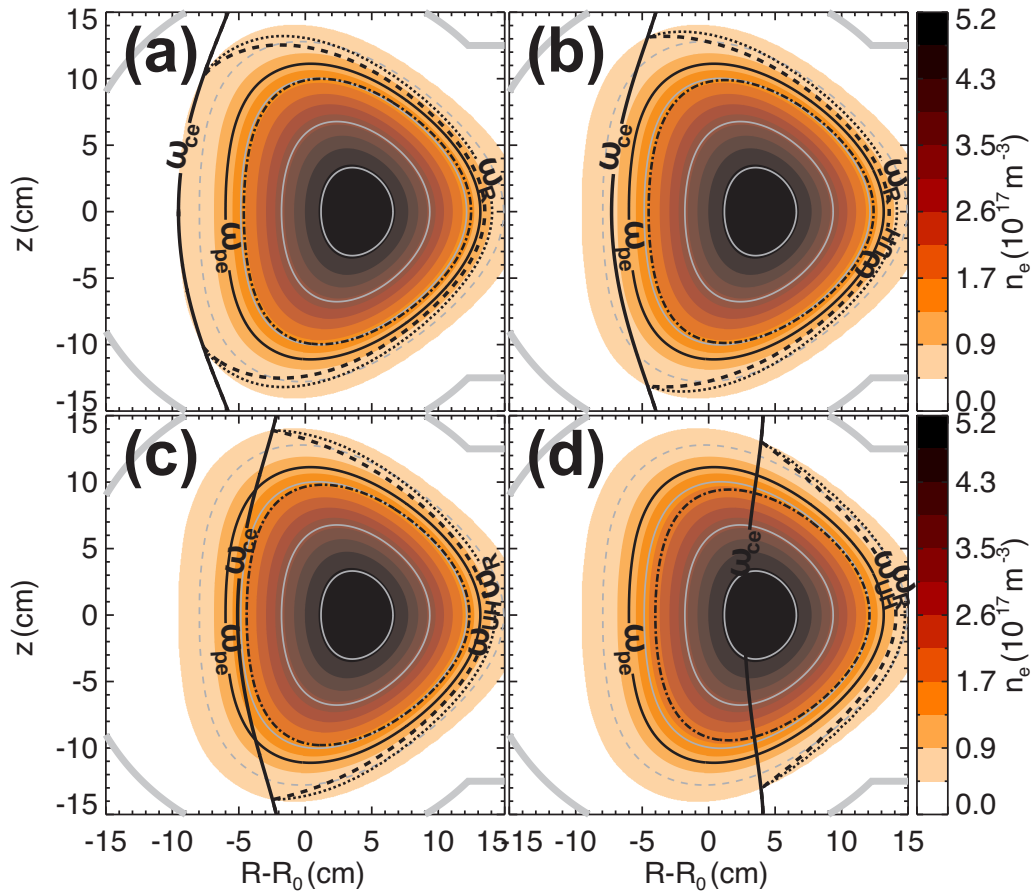


Figure 5.9: Poloidal density profiles obtained from Eq. (5.2) with the positions of the resonances and cutoffs as labeled in the graphs for (a) $B_0 = 48$ mT, (b) $B_0 = 66$ mT, (c) $B_0 = 72$ mT and (d) $B_0 = 96$ mT.

a small distance outside the cutoff and thus the incident microwave can reach this resonance without being shielded. Although the theoretical single pass absorption at the cyclotron resonance is low, see Ref. [89], a larger amount of power can be absorbed at this resonance if multiple reflections between vacuum vessel and cutoff and, hence, multiple traverses through the resonance layer are taken into account. In addition, part of the cyclotron resonance layer is in this configuration located on the same flux surfaces, as the upper-hybrid resonance, which complicates the analysis. In this case, due to the higher electron temperatures that are achieved at the UHR, the power absorption at the cyclotron resonance may also play a role. This is not expected at the other values of the magnetic field strength.

5.4 Estimation of the heating efficiency

To model the discharges in TJ-K, a global particle and power balance has been carried out. To this end, the sum of particle and energy sources and sinks is taken to be compensated by radial particle and energy transport. In low temperature plasmas, like the plasma in TJ-K, atomic processes are responsible for the sources and sinks. The different atomic processes are described by rate coefficients. Rate coefficients for hydrogen, helium and argon in the range of the relevant parameters for TJ-K are given in Ref. [122]. The resulting particle and energy flux allows then to estimate the particle diffusivity D and the heat diffusivity χ , respectively. In this model, the ratio of thermal to particle diffusivity, $\gamma = \chi/D$, is an important parameter. According to Ref. [116], a value of $\gamma = 10$ provides a good description of the discharges in TJ-K. Assuming ions and neutrals to be cold and the electron temperature higher than 1 eV, according to Ref. [122] the balance equations can be cast in the form

$$n_e = \frac{P/(n_0 V)}{((\gamma + 3/2 \alpha) T_e + E_{\text{ion}}) \langle \sigma v \rangle_{\text{ion}} + E_{\text{rad}} \langle \sigma v \rangle_{\text{rad}}}, \quad (5.1)$$

where P is the microwave power, n_0 the neutral gas density, $V = 0.118 \text{ m}^{-3}$ the plasma volume, $\alpha = T_{e,\text{separatrix}}/T_{e,\text{centre}} = 1.3$, E_{ion} the ionization energy with the corresponding rate coefficient $\langle \sigma v \rangle_{\text{ion}}$ and E_{rad} the mean radiation energy which is lost due to excitation of neutrals with the corresponding rate coefficient $\langle \sigma v \rangle_{\text{rad}}$. The balance allows to estimate upper limits for n_e and T_e for a given heating power, neutral gas density, and type of gas. A comparison with the experimental data gives an estimate of the amount of heating power absorbed by the plasma.

The background magnetic field B_0 does not appear explicitly as an input parameter in Eq. (5.1). Nevertheless, a variation in the value of B_0 was observed to have a strong impact on the plasma parameters density and temperature, as was shown Sec. 5.3. Hence, B_0 is the control parameter, which is varied to get different plasma parameters for the same heating power, neutral gas pressure and type of gas.

Fig. 5.10 shows experimental data from a series of (a) hydrogen, (b) helium and (c) argon discharges for three values of the neutral gas pressure. The different

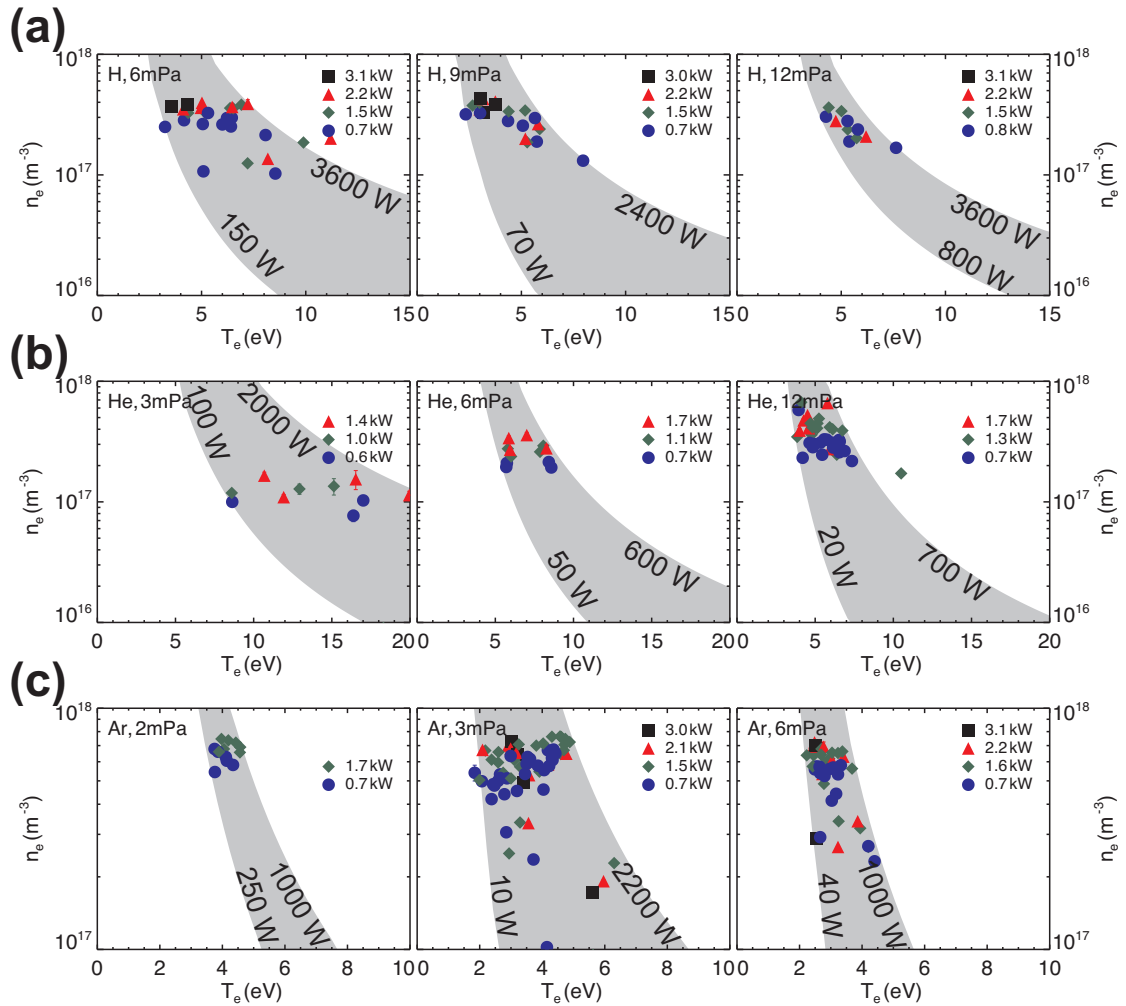


Figure 5.10: Central electron density as a function of central electron temperature for (a) a series of hydrogen discharges, (b) a series of helium discharges and (c) a series of argon discharges. Symbols indicate data obtained from measurements, where different colored symbols account for different absorbed power. Shaded area indicates estimation obtained from the global particle and power balance, Eq. (5.1), where the input power has been varied in the range given by the numbers in the graphs. The different graphs for the three different gases represent each a different neutral gas pressure given in the upper left side of each graph.

colored symbols account for different heating powers. The values of the electron temperature are obtained from swept Langmuir probes (see Sec. 4.3.1 for details) and were taken in the plasma center. To get the central density, the values obtained from the interferometer, which are line averaged values (see Sec. 4.3.3 for details), have been multiplied with an average peaking factor of 2. The shaded areas mark the accessible parameter space obtained from the balance equation, when the heating power is assumed to be entirely absorbed in the confinement region. The values of the heating power necessary to obtain the boundary of the shaded areas are given in the graphs. This type of presentation is chosen because it includes all experimental data points by varying only the heating power.

Considering the hydrogen discharges shown in Fig. 5.10a, it is noticeable that the experimental data spread out farther for lower values of the neutral gas pressure. In the plots for $p_0 = 6$ mPa and $p_0 = 9$ mPa, several discharges can be found at the lower boundary of the shaded area, with an injected power exceeding the required power given at this boundary by a factor of 10. Two mechanisms can be responsible for this discrepancy. In Ref. [122] it was shown that higher values of γ , which are the equivalent of higher heat diffusivities, shift the values obtained from the balance equation to lower densities and temperatures. Hence, the losses due to conduction in these discharges would be underestimated. The second possible explanation involves the location of power deposition. In the balance it is assumed that all power fed into the system is absorbed in the confinement region. However, in Sec. 5.3 it was shown that heating of the plasma can take place partly on open field lines. If power deposition on open field lines plays a non-negligible role, part of the power is lost parallel to the field lines to the vacuum vessel. In contrast, one can also find some hydrogen discharges in Fig. 5.10a, with heating powers below the calculated values necessary to sustain the discharges. Here, losses due to conduction are probably overestimated and complete absorption of the injected power can be assumed.

Helium discharges are shown in Fig. 5.10b. They tend to spread more for lower values of p_0 . Only for $p_0 = 3$ mPa, a few discharges are found with the experimental heating power below the theoretical values. For $p_0 = 6$ mPa and $p_0 = 12$ mPa, the experimental values either agree with the theoretical ones or lie above those. As described before, this can be either due to underestimated losses through conduction or to heating on open flux surfaces.

The highest densities are reached in argon discharges, as shown in Fig. 5.10c. Here, all experimental heating powers lie above the theoretical values. Due to the higher densities, the upper-hybrid resonance is shifted outwards. Hence, for discharges, where experimental heating power is higher than the theoretical one, the reason is most likely increased heating on open flux surfaces. For the case of $p_0 = 3$ mPa, a trend of experimental values to move perpendicularly to the boundary curves is observed, which indicates a change in transport with magnetic field strength.

In sum, the global particle and power balance can be used to estimate an upper limit of the accessible plasma parameters. A decrease in the spread of the measured

densities and temperatures with increasing pressure is found for all gases. This applies not to the low pressure series for argon, albeit it contains numbers of discharges too small to draw a valid conclusion. The most efficient heating is found in hydrogen discharges. Nevertheless, care has to be taken for hydrogen, since the deduced transport coefficients scatter a lot for different discharges. Argon discharges are the least efficient due to the inherent high density that shifts the position of plasma heating to open field lines. The measurements reported in this section underline the important role of energy losses along open field lines in TJ-K.

5.5 Full-wave simulations

With the full-wave code IPF-FDMC, described in detail in Sec. 3, simulations of the microwave incident into TJ-K have been carried out. In order to study the wave propagation numerically, it is convenient to describe the experimental density profile by an analytical formula. The following equation was used to fit the experimental data:

$$n_e(r_{\text{eff}}) = n_{e,0} \cdot \exp \left\{ - \left(\frac{r_{\text{eff}}}{w_n} \right)^{\alpha_n} \right\}, \quad (5.2)$$

with $n_{e,0}$ the density on the magnetic axis, r_{eff} the effective flux surface radius and the profile parameters w_n and α_n . Constant density on flux surfaces is assumed, thus 2-dimensional density profiles can be calculated at arbitrary toroidal positions. In Fig. 5.11, a radial density profile obtained during an argon discharge is shown together with the density profile obtained from Eq. (5.2) with $w_n = 0.55$ and $\alpha_n = 2.9$. One can see that the experimental data are well represented.

The plasma density profile used as background in the simulations is parameterized by Eq. (5.2): Figure 5.12a shows the density profile in the poloidal cross section, where the profiles are usually measured. Figure 5.12b shows the profile in the poloidal cross section, where the antenna of the 2.45 GHz heating system is installed. The resonances and cutoffs are indicated by different lines.

The background magnetic field of TJ-K can be computed at arbitrary position with a code that has been developed by M. Ramisch at IPF and is referred to as *MCC* [124]. Hence, the actual experimental geometry is used in the simulations. In this section, first the simulations in the poloidal plane and then in the toroidal plane will be presented.

5.5.1 Simulations in the poloidal plane

Due to the 3-dimensional geometry of the flux surfaces in TJ-K, the antenna radiates a mixture of X- and O-mode. The simulations allow to treat the two modes separately. First, calculations in the X-mode configuration with a high resolution will be presented, where 512 grid points per vacuum wavelength are used. Figure 5.13a

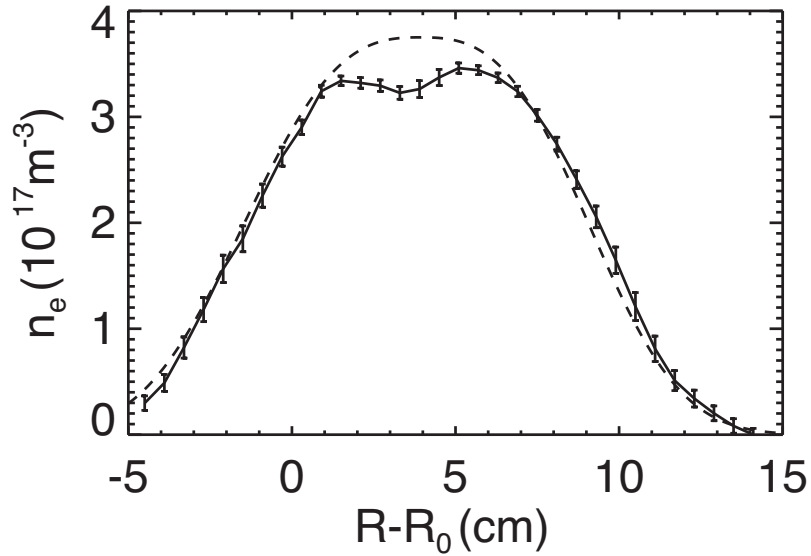


Figure 5.11: Radial electron density profile at outer port. Solid line indicates experimental data from #3859, dashed line indicates the fit formula given in Eq. (5.2).

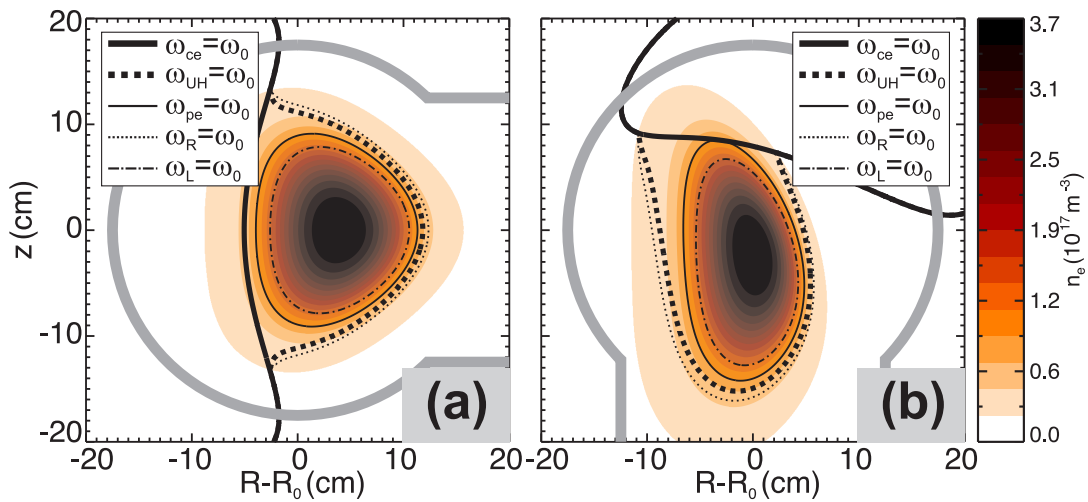


Figure 5.12: Density profile in different poloidal cross sections obtained from Eq. (5.2), resonances and cutoffs are indicated by different line styles. (a) Toroidal position, where diagnostics are usually located. (b) Toroidal position, where the microwave power is injected from the bottom into the torus. (The figure is also published in Ref. [123].)

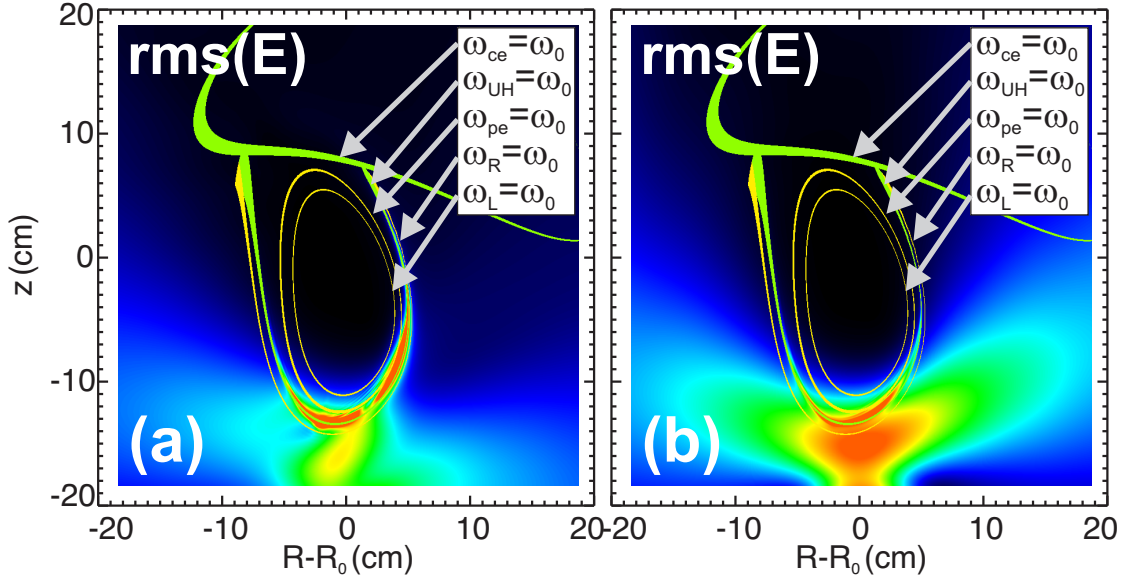


Figure 5.13: Results from simulations with the full-wave code IPF-FDMC after 30 periods of oscillation. The antenna in (a) X-mode configuration and (b) in O-mode configuration is located at the bottom. The boundaries are implemented as absorbing to simulate the single pass absorption. Shown is the rms-value of the wave electric field. (The figure is also published in Ref. [123].)

shows the rms value of the wave electric field, for the case with the antenna implemented in X-mode configuration. The microwave is fed into the rectangular cut waveguide described in Sec. 4.2.1 to represent the experimental situation as closely as possible. The steady state solution is achieved after 30 oscillation periods. A strong field enhancement is found at the position, where the microwave first interacts with the plasma. This enhancement is concentrated in a thin layer around the UHR. Although the UHR lies behind the R-cutoff, the simulations yield a single pass absorption coefficient of $\eta_X = 0.12$. This is due to the small distance between the R-cutoff and the UHR, allowing tunneling of the X-mode through the evanescent layer between cutoff and resonance. This tunneling process was first described by Budden for the ionosphere [42] and is therefore sometimes referred to as *Budden tunneling* [125].

To calculate the absorption coefficient according to Budden's analysis, it is convenient to use the tunneling parameter $\beta = \pi k_0 x_0 / 2$, where k_0 denotes the vacuum wavenumber and x_0 the distance between R-cutoff and UHR. The transmission and reflection coefficients are $T = e^{-\beta}$ and $R = 1 - e^{2\beta}$, respectively. From Fig. 5.13a it is possible to estimate $x_0 \lesssim 0.8$ cm. This yields $\beta \approx 0.645$ and for the fraction of absorbed power $\eta_X^2 = 1 - (R^2 - T^2) \approx 0.20$. This value differs from the result obtained with full-wave simulation since the microwave beam diverges after it is emitted from the antenna and, therefore, only a fraction of the beam reaches the evanescent layer at normal incidence. Hence, Budden's analysis can only serve to

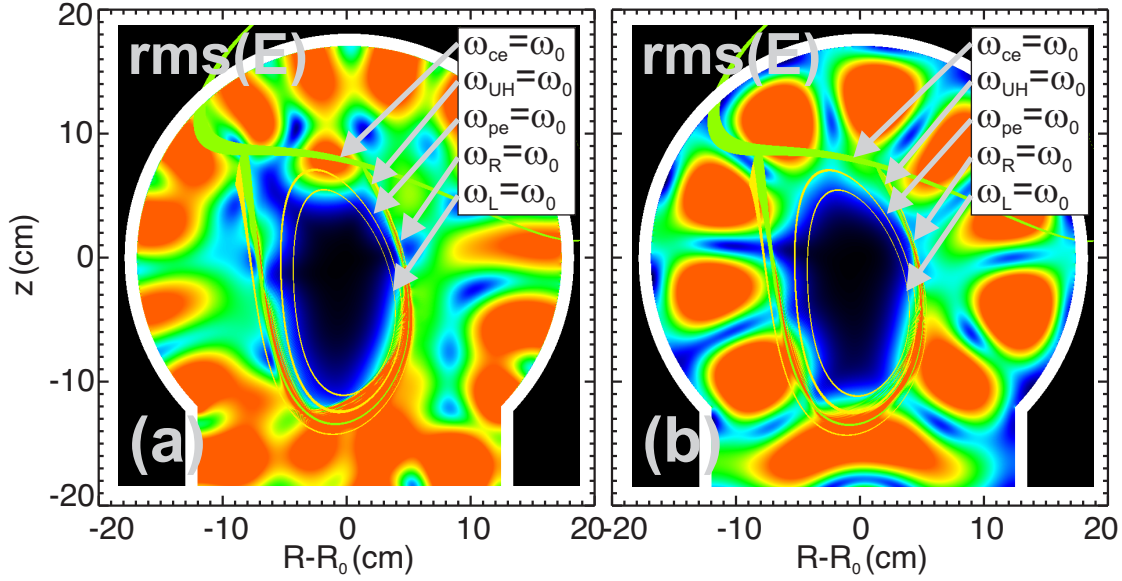


Figure 5.14: Same as Fig. 5.13 but after 300 oscillation periods and with the geometry of the vacuum vessel of TJ-K included in the calculations. (The figure is also published in Ref. [123].)

find the upper limit for the absorption.

Rotating the antenna by 90 degrees leads to a launch of the microwave in O-mode polarization. In the simulations, this results in a strong decrease in the absorption coefficient to $\eta_0 \approx 0.02$. Figure 5.13b shows the rms-value of the wave electric field. Again, the plot is made after 30 oscillation periods. A small enhancement around the UHR can be seen. But here, in contrast to the X-mode configuration, the wave trajectory to finally reach this enhancement region is different: Part of the incident O-mode is mode-converted at the O-mode cutoff ω_{pe} into an X-mode which then propagates back to the UHR. In principle, further mode-conversion of the X-mode into an EBW could take place. This type of mode conversion is not implemented in these simulations. Instead of being mode converted, the X-mode is assumed to be absorbed at the UHR via collisions. The overall conversion efficiency is only determined by the O-X conversion efficiency, whether the mode-converted X-mode is completely absorbed or further converted into an EBW at the UHR (c. f. Sec. 2.4). The fraction of the incident O-mode, which is not converted into an X-mode, is simply reflected at the O-mode cutoff and then leaves the plasma without further interaction.

For both types of polarizations, the fraction of absorbed power increases dramatically, when the TJ-K vacuum vessel is taken into account in the simulations. The vessel walls are realized as perfectly conducting material which is justified by the fact that the reflectivity of stainless steel for the 2.45 GHz is 99.9 % [126]. Hence, the microwave absorption is determined almost completely by losses inside the plasma and not at the wall. Figure 5.14a shows the rms-value of the wave electric field for

the case of X-mode incidence. The geometry of the vacuum vessel and the port where the microwave antenna is located are indicated by the thick white line. In this geometry, because of multiple reflections, it takes 300 oscillation periods for the simulation to become stationary. The full-wave code now yields a fraction of absorbed power of $\eta_X \approx 0.80$. This value represents an increase by a factor of almost seven above the single pass value. It can be explained by the fact that the wave is reflected multiple times between the vacuum vessel and the cutoff. Each time a fraction of the power is deposited in the layer around the UHR. Additionally, the X-mode can reach the UHR without having to pass a cutoff if it is reflected from the upper wall of the vessel, which corresponds to the high-field side at this toroidal position. For this trajectory, Budden's analysis yields almost complete absorption at the UHR. From these simulations it can be seen that the plasma can be heated efficiently near the boundary. The rest of the power (20 %) is reflected back into the waveguide.

In O-mode polarization the vacuum vessel leads to an increase in the absorption coefficient from $\eta_O \approx 0.02$ to ≈ 0.18 , shown in Fig. 5.14b. The increase can be explained by a partial conversion of the incident O-mode into an X-mode due to reflection at the vessel walls. The X-mode is then absorbed at the UHR. This polarization change due to reflection at the vessel walls has also been proposed for the DIII-D tokamak in the USA and is discussed in detail in Refs. [125, 127].

5.5.2 Simulations in the toroidal plane

To study wave propagation and interaction with the plasma *along* the torus axis, simulations in the toroidal plane have been carried out. The toroidal plane is realized as a vertical cut along the center of the vacuum vessel. The density profile results from a vertical cut along $R - R_0 = 0$ cm in Fig. 5.12b. The same applies to the background magnetic field profile.

Figure 5.15a shows the rms-value of the wave electric field for X-mode incidence after 195 oscillations periods, when the stationary state is reached. The geometry of the vacuum vessel and of the antenna are both included in the simulations and indicated in the plots by white lines. The UHR is located at $z \approx -9.5$ cm. At precisely this position the expected enhancement in the electric field can be seen. This enhancement extends toroidally, since the vacuum vessel acts as the outer wall of a coaxial waveguide with the cutoff layer as the inner conducting surface. Through this waveguide the microwave is distributed over the toroidal circumference of TJ-K. The same effect has been discussed for the Madison Symmetric Torus [128].

The case of O-mode incidence is considered in Fig. 5.15b. The enhancement at the UHR is still seen but it is broadened in the z -direction. It is important to note that for both polarizations the enhancement at the UHR extends in the toroidal direction. The simulations with the code furthermore show an asymmetry in the electric field with respect to the antenna axis. This effect was predicted from theory and is discussed in detail in Ref. [129]. It is also reported in Refs. [44, 53].

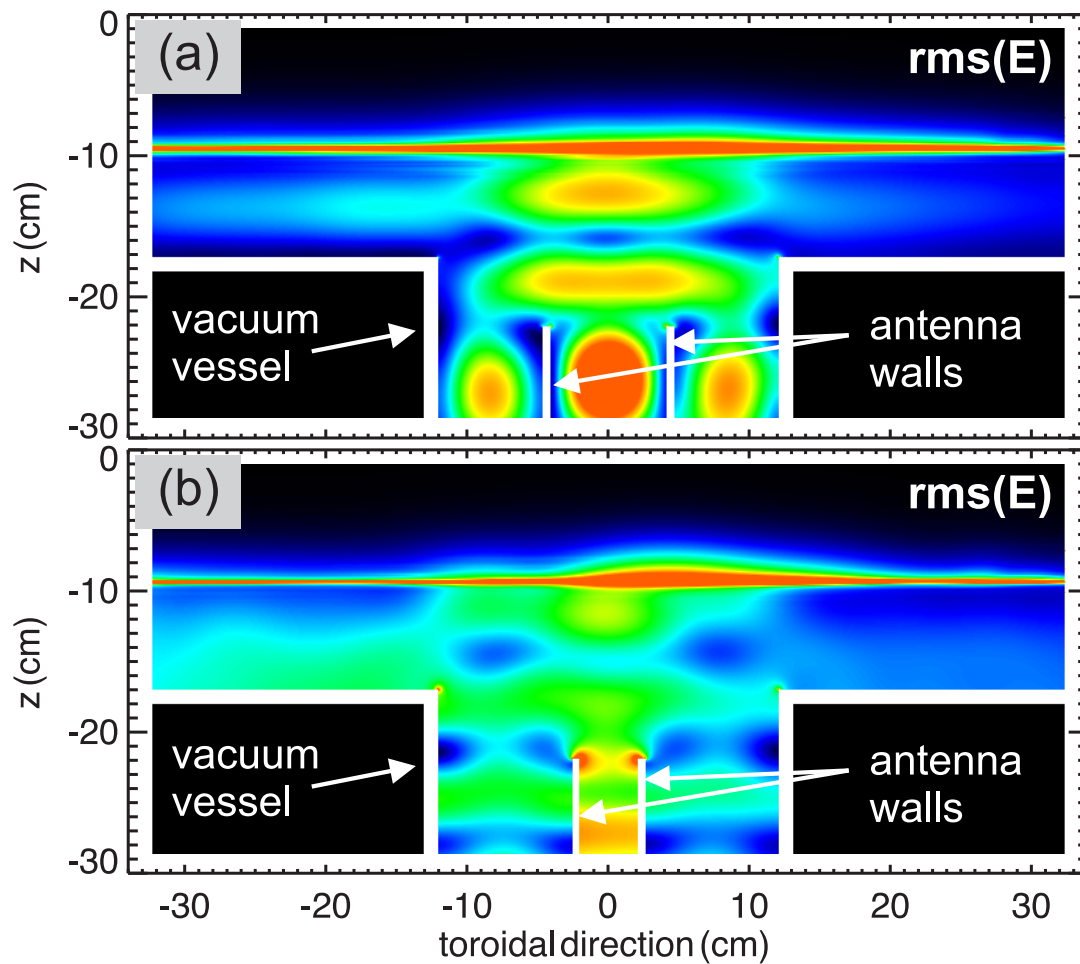


Figure 5.15: Results after 195 oscillation periods from simulations with the full-wave code IPF-FDMC carried out in the toroidal plane. The UHR is located at $z = -9.5$ cm. (a) Antenna in X-mode configuration is located at the bottom. (b) Antenna in O-mode configuration. (The figure is also published in Ref. [123].)

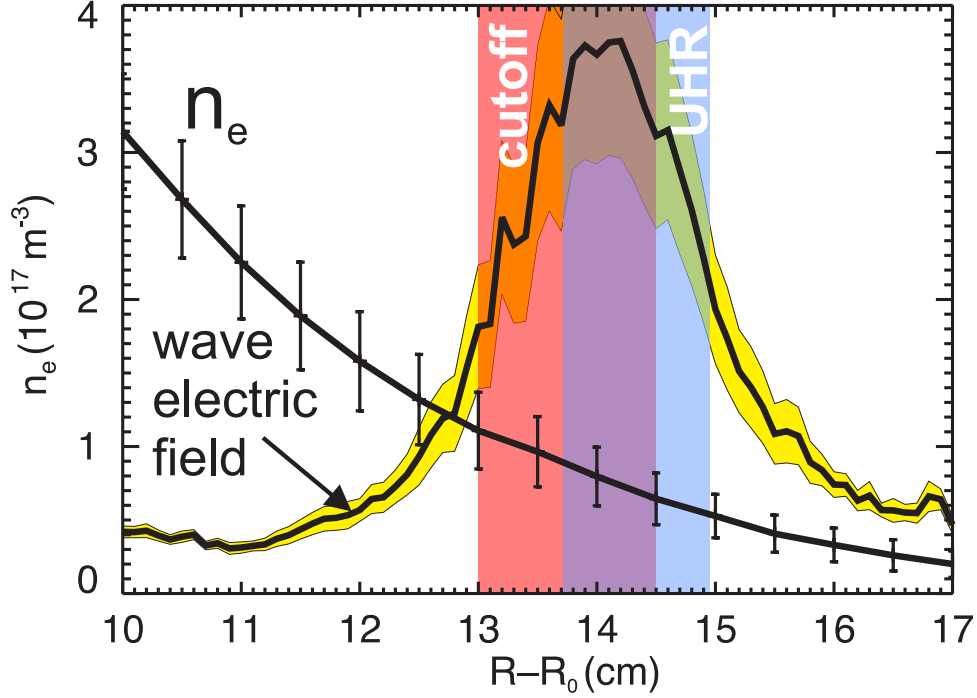


Figure 5.16: Radial profile of electron density with error bars and radial wave electric field at 2.45 GHz with error as the (yellow) filled area surrounding the curve obtained during an argon discharge (#5614). From the scatter in the measured density, the width of the UHR and the O-mode cutoff are derived. (The figure is also published in Ref. [123].)

5.6 Measurement of the wave electric field of the incident microwave

The simulation in the previous section demonstrated a marked enhancement of the wave electric field at the UHR. This result is compared with experiments using a monopole antenna as described in Sec. 4.3.2. The probe was mounted at a different toroidal position than the microwave heating antenna. Nevertheless, according to the simulations in Fig. 5.15, the enhancement extends toroidally and should therefore still be visible at different toroidal positions.

Figure 5.16 shows the radial profiles of the wave electric field and the electron density. The position of the UHR and the O-mode cutoff are indicated by the filled areas, which represent the error arising from the density measurements. This variation is mainly due to the relatively large turbulence level close to the plasma boundary. The concomitant fluctuations in the measurement of the wave electric field are indicated by two thin lines. The enhancement of the wave electric field at the UHR is clearly confirmed. Behind the UHR, the field drops to a small value. This is to be expected, since both the O-mode and X-mode cutoffs are located close to the UHR. The fact that the field enhancement at the UHR can be measured with

the monopole antenna at a toroidal position away from the antenna port underlies the relevance of the code results reported in Sec. 5.5.2.

Field components due to a possible EBW in the mode conversion layer could not be identified. This is thought to be due to the complicated situation in this layer, where the EBW coexists with the O- and X-mode components, oscillating at the same frequency and at the same position.

Another reason that no EBW is seen, could be collisional damping. Previous calculations with IPF-FDMC for values of the normalized collision frequency $\nu/\omega_0 \approx 10^{-5}$ [44], which corresponds to experimental values in TJ-K show no distinct damping of the EBW. This is in agreement with the results found in Ref. [120], where a threshold of $\nu/\omega_0 \approx 10^{-4}$ is given, above which the damping of the EBW due to collisions becomes non-negligible. Hence, damping of the EBW cannot be the reason for the absence of wave power behind the cutoff. Although the generation of EBW cannot be finally excluded, a significant contribution by EBW to plasma heating at the cyclotron resonance is not seen.

5.7 Fast power modulation studies

Power-modulation experiments were used to measure the power deposition profile. The microwave power acts on the electron temperature and through ionization on the plasma density. This technique is well established to measure the power deposition profile [130, 131], since the temporal development of the electron temperature is hardly resolved on the necessary short time scales with Langmuir probes. Simulations with a particle and power balance have shown that at modulation frequencies above 20 kHz, the modulation amplitude in density is directly connected to the power deposition profile [116].

Figure 5.17 depicts the response of the ion saturation current as measured with the multiple probe array SPIDER during a hydrogen discharge, heated with microwaves modulated with 20 kHz. The positions of the fundamental resonance and the UHR are indicated by the thick solid and the thick dashed lines, respectively. They were obtained from Eq. (5.2) and the line averaged density corresponding to this discharge. Due to the lower density as compared to the profiles shown in Fig. 5.12, the UHR is shifted inward. One can see that the density modulation is most pronounced at the UHR layer and on the flux surfaces which are connected to it. Again, this experiment shows that heating by EBW seems not to play a major role, since no distinct modulation is found near the cyclotron resonance layer, where the EBW would be absorbed.

5.8 Parametric instabilities

In Secs. 5.5 and 5.6 it was shown that the microwave reaches its maximum amplitude at the UHR. The high values, which were found in the experiment, can give rise to

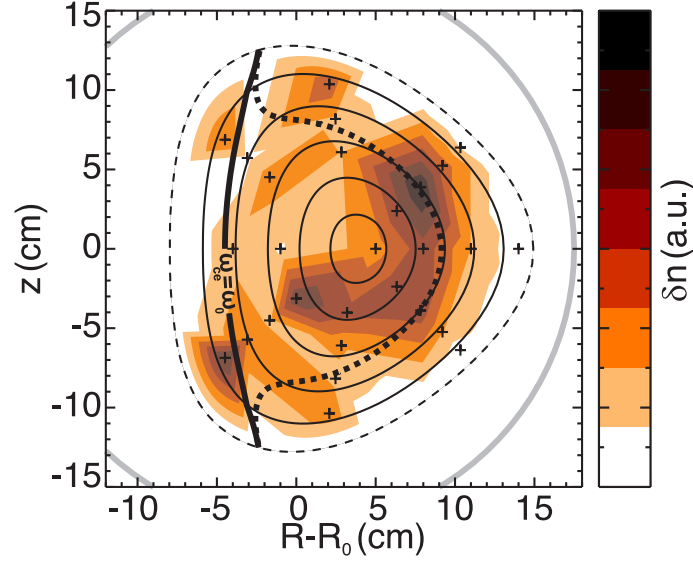


Figure 5.17: Modulation amplitude δn of the ion saturation current for a hydrogen discharge (#4943) during which the microwave power was modulated with 20 kHz. The position of the fundamental resonance and the UHR are indicated by thick solid and dashed lines, respectively. (The figure is also published in Ref. [123])

nonlinear phenomena like parametric instabilities [108, 132]. Since the development of high power radio frequency sources in the seventies, especially the gyrotron [133], the investigation of parametric instabilities has been of great interest in the magnetic fusion community due to the possible applications for plasma heating [134, 135]. For the same reason, parametric instabilities are investigated [136, 137] in the context of laser fusion [138]. Ionospheric heating experiments originate further scientific interest in parametric instabilities [139, 140].

Due to this widespread interest in the field of plasma physics, substantial theoretical [141, 142], numerical [132, 143] and experimental [144, 145, 146, 147, 148] research has been performed in the past and is still pursued nowadays [149, 150, 151].

Parametric instabilities occur not only in plasma physics, since they belong to the wide field of nonlinear dynamics. Every oscillating system in which one *parameter* is modulated at an appropriate frequency can give rise to parametric instabilities. A broad overview with the focus on radiophysical systems is given for example in the textbook from Damgov [152].

An extensive review of the topic of parametric instabilities in plasmas can be found in Ref. [153], and an introduction into this topic in Refs. [32, 154]. The simplest case of a parametric instability is the three wave coupling in which a *pump wave* with the frequency ω_0 excites two waves with the frequency ω_1 and ω_2 , also referred to as *idler* and *signal*. According to the Manley-Rowe relations [155, 156],

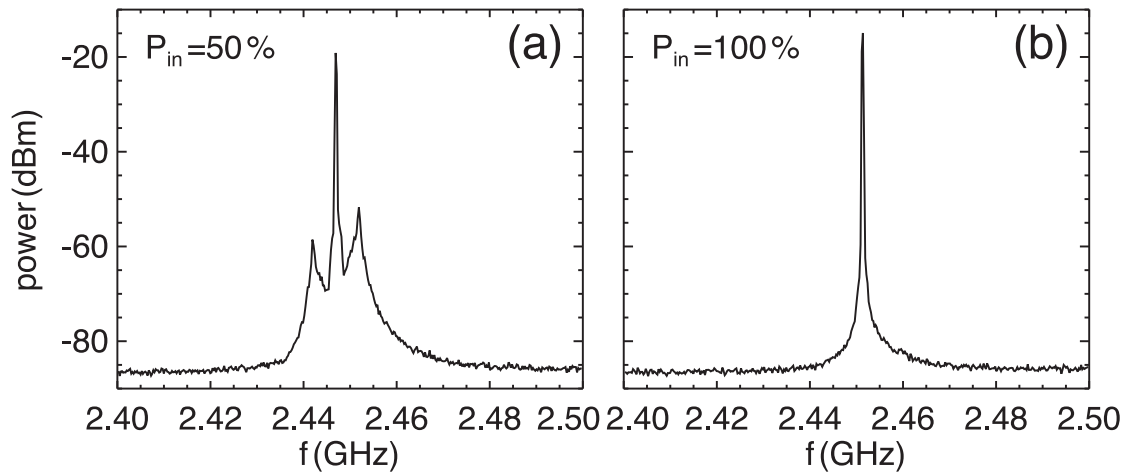


Figure 5.18: Frequency spectrum of the microwaves generated by the magnetron ③ at (a) half and (b) at maximum output power.

the frequency and wavenumber matching condition must be fulfilled:

$$\omega_0 = \omega_1 + \omega_2 \quad (5.3)$$

$$k_0 = k_1 + k_2. \quad (5.4)$$

The corresponding waves in the plasma must appear as solutions of dispersion relations. Thus, it is possible to transfer energy from high-frequency modes, like upper-hybrid oscillations, to low-frequency modes, like lower-hybrid oscillations. The parametric excitation can constitute an important mode-conversion mechanism that can transfer energy from an incident wave into the plasma by exciting two new modes inside the plasma. If the excited waves can then transfer their energy to the plasma, effective heating through a parametric instability can be obtained.

A parametric instability has been identified in the stellarator W7-A [148] in 28 GHz heating experiments, in which the incident wave f_0 decays into a low-frequency component f_{low} and a high-frequency component $f_{\text{high}} = f_0 - f_{\text{low}}$. The lower frequency is considered to belong to the lower-hybrid and the higher frequency to the upper-hybrid frequency range. Experimental results from TJ-K indicate that the same process takes place. This will be presented in the following section.

5.8.1 Measurements in TJ-K

The monopole antenna described in Sec. 4.3.2 is used to obtain frequency spectra in the heating frequency domain around 2.45 GHz. To this end, the probe is connected via a low loss microwave cable (SUCOFLEX 104) to a spectrum analyzer (Agilent E4402B). Due to the high dynamic range of the spectrum analyzer, the use of a notch filter, which suppresses the source frequency, is not necessary. Since one of the decay components is expected to lie very close to the heating frequency, the

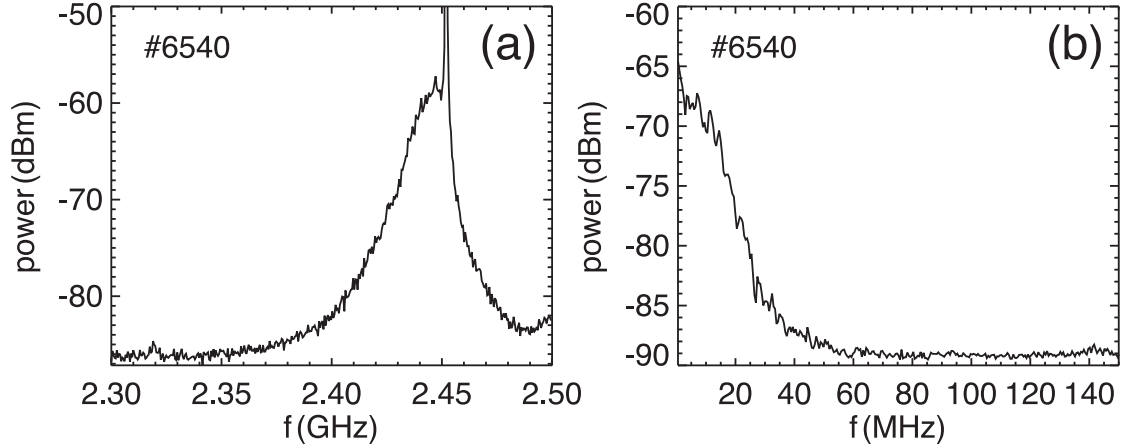


Figure 5.19: (a) Spectrum obtained with monopole antenna at $R - R_0 = 10$ cm. (b) Spectrum obtained with loop antenna positioned at plasma boundary.

spectral width of the magnetron has to be very narrow. This has been checked with a directional coupler installed in the transmission line.

Figures 5.18a and 5.18b show the frequency spectra of the microwaves generated by the magnetron at half and full output power, respectively. Obviously, the magnetron must run at maximum power to obtain the required spectral purity. Hence, in order to vary the power injected into the vacuum vessel, a 3-stub tuner is used. Mismatching of the tuner results in increased reflected power, which is absorbed in a beam dump (see Fig. 4.4). This operation mode conserves the clean frequency spectrum of the magnetron. Therefore, to vary the heating power, the 3-stub tuner is used, while the output power of the magnetron is kept at maximum level.

The low frequency component of the parametric decay is measured using a small loop antenna made of stainless steel with a diameter of approximately 37 mm and located close to the plasma edge at the inner port I-3. The antenna is connected to an amplifier (avantek GPD403) via a standard BNC cable. This signal is then acquired with the same spectrum analyzer used for measurements at high frequency. A similar type of antenna was successfully used at the W7-AS stellarator to detect lower-hybrid waves [157].

Figure 5.19a shows a spectrum in the vicinity of the heating frequency obtained with the monopole antenna in a helium discharge. The incident microwave at $f_0 = 2.45$ GHz can be clearly identified. With the spectrum of the signal emitted from the magnetron as a reference (cf. Fig. 5.18), a sideband appearing on the low-frequency side of f_0 can be recognized. This sideband is broadband with a continuous decay down to a frequency of $f_1 \approx 2.4$ GHz. The monopole antenna was positioned at $R - R_0 = 10$ cm. The low-frequency component, measured with the loop antenna and corresponding to $f_2 = f_0 - f_1$, is found in the spectrum shown in Fig. 5.19b. The width of this spectrum is similar to the high-frequency component, fulfilling the requirement for a parametric decay given in Eq. (5.3). It was not possible to detect

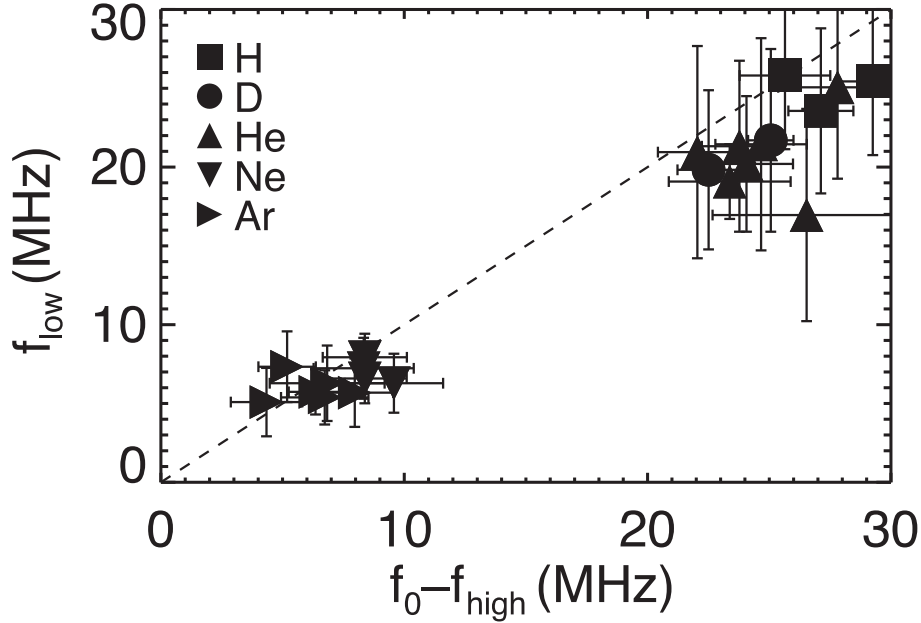


Figure 5.20: Comparison of the spectral width at a decay of -10 dB of the high-frequency decay spectrum (horizontal axis) and the low-frequency decay spectrum (vertical axis) for different gases indicated by different symbols.

the low-frequency signal with the monopole antenna. This could be due to the low capacitance between plasma and the thin antenna wire so that the electrostatic low-frequency wave cannot couple to the monopole antenna inside the ceramic tube.

To determine the range over which f_1 and f_2 are observed, the spectral width at a decay of -10 dB is chosen. This analysis was applied to a series of discharges with different gases and varying heating power. The resulting graph is given in Fig. 5.20, where the horizontal and vertical axes correspond to the high and low-frequency signal, respectively. Both values match well, supporting the assumption that a parametric decay instability occurs during the wave absorption process at the UHR layer.

A general trend can also be seen from the figure: lighter gases tend to show broader spectra. Hence, the low frequency component in the parametric decay, f_2 , seems to be related to the ion mass. This points to *lower-hybrid waves* or *ion acoustic waves* as candidates for the decay wave.

According to Ref. [22], the dispersion relation for lower-hybrid waves reads

$$k_x^2 \left(1 + \frac{\omega_{pe}^2}{\omega_{ce}^2} + \frac{\omega_{pi}^2}{\omega_{ci}^2 - \omega^2} \right) - k_x \frac{d}{dy} \frac{\omega \omega_{pi}^2(y)}{\omega_{ci}(\omega_{ci}^2 - \omega^2)} + k_{\parallel} \left(1 - \frac{\omega_{pe}^2}{\omega^2} \right) = 0, \quad (5.5)$$

with y the direction parallel to the density gradient and k_{\parallel} the wavenumber parallel to \mathbf{B}_0 . Assuming propagation perpendicular to \mathbf{B}_0 , i. e. $k_{\parallel} \rightarrow 0$, in an homogenous plasma, i. e. $d/dy(\omega_{pi}^2(y)) \rightarrow 0$, reveals a resonance at the *lower-hybrid* frequency

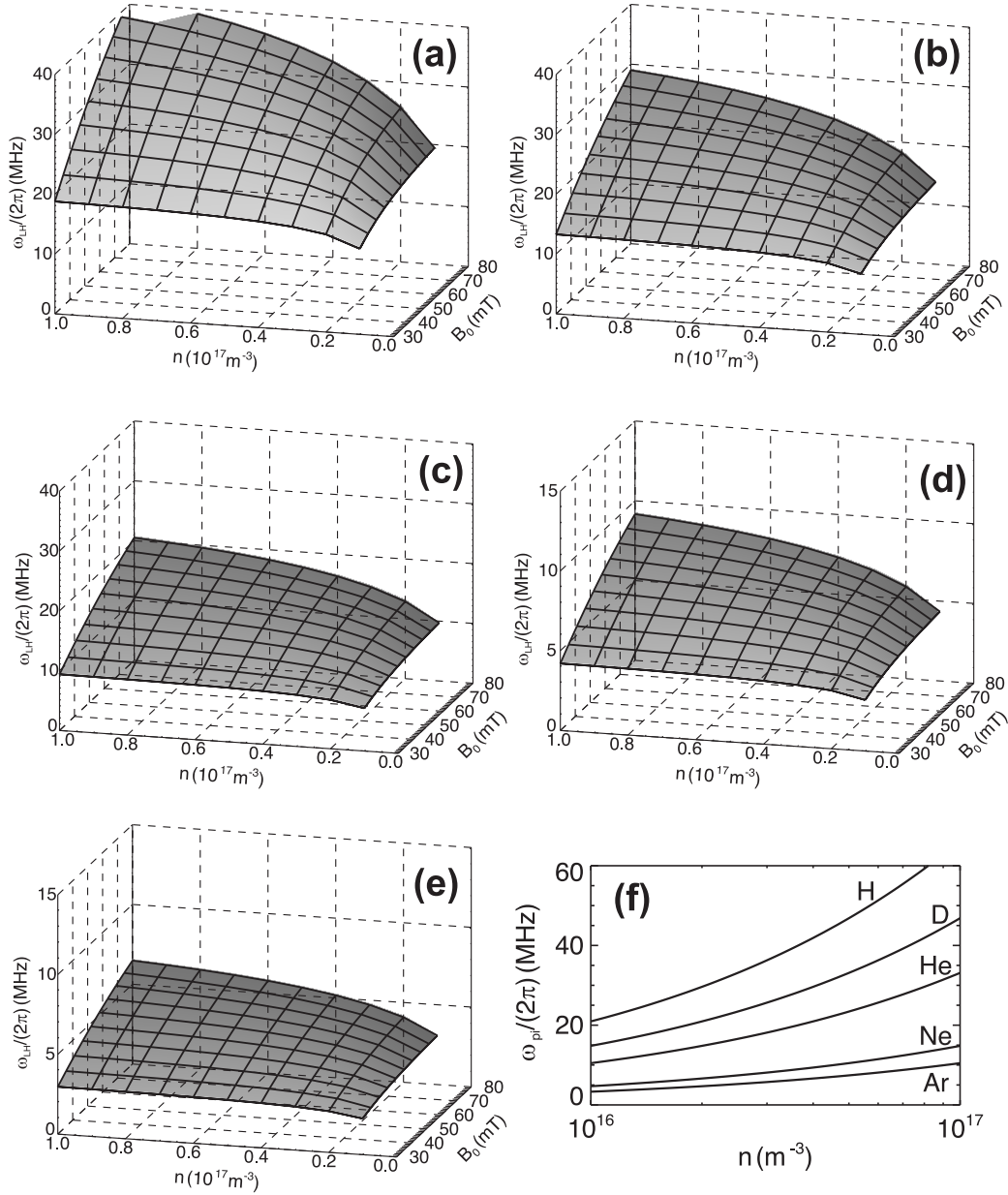


Figure 5.21: Lower-hybrid frequency as function of magnetic field and plasma density for (a) hydrogen, (b) deuterium, (c) helium, (d) neon and (e) argon. (f) Ion plasma frequency as function of plasma density for different gases, which are indicated in the plot.

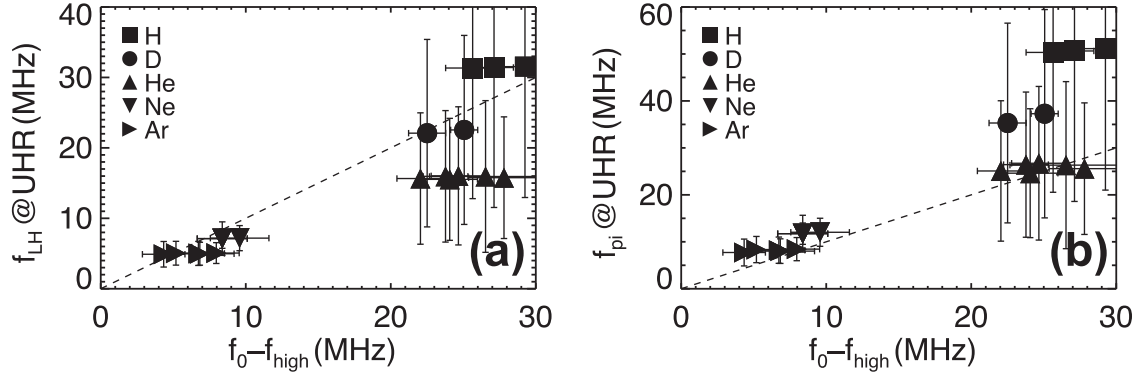


Figure 5.22: (a) Lower-hybrid frequency calculated at the position of the upper-hybrid resonanc as a function of the spectral width of the HF signal (see Fig. 5.20a), different gases are indicated by different symbols. (b) Same as (a) but for the ion plasma frequency instead of the lower-hybrid frequency.

ω_{LH} with

$$\frac{1}{\omega_{LH}^2} = \frac{1}{\omega_{ci}^2 + \omega_{pi}^2} + \frac{1}{\omega_{ci}\omega_{ce}}. \quad (5.6)$$

In the vicinity of the lower-hybrid resonance (LHR), ω/ω_{ci} can reach high values (of the order $(m_i/m_e)^{1/2}$). The middle term in Eq. (5.5) can therefore contribute to significant corrections as compared with the conventional lower-hybrid resonance [22]. Furthermore, a non-zero parallel wavenumber can lead to a broadening of the spectrum. As one can see from Eq. (5.6), ω_{LH} is a function of the plasma density n and the magnetic field B_0 . Figures 5.21a – 5.21e illustrate this relationship: the lower-hybrid resonance frequency is plotted as function of n and B_0 for the five working gases used in TJ-K. The values of $f_{LH} = \omega_{LH}/(2\pi)$ increase with increasing density, increasing magnetic field and decreasing ion mass. The calculated frequencies are in the range of the values found it the experimental decay spectra (cf. Fig. 5.20).

The parametric decay instability needs sufficiently high wave electric field amplitudes to occur. According to Secs. 5.5 and 5.6 the highest values arise at the UHR. From density profile measurements the position of the UHR and, hence, the values of n and B_0 can be identified for which the parametric instability is likely to occur. In Fig. 5.22a the frequency of the LHR at this position is compared with the measured frequency range of the decay wave. The vertical axis depicts the values of the LHR, obtained as just described, the horizontal axis depicts the spectral width of the decay spectra in the HF regime of the corresponding discharges. A straight line with $f_{LH} = f_0 - f_{high}$ is indicated by the dashed line. The general trend that heavier gases result in lower values for the LHR is found with good agreement between the experimental and theoretical values. Only for the case of the helium discharges the experimentally obtained values are all slightly higher than the theoretical ones.

The second candidate for f_2 , the ion acoustic waves (IAW), appear as a solution of the dispersion relation for waves in a warm plasma, propagating along the background magnetic field [23]:

$$1 - \frac{\omega_{pe}^2/\omega^2}{1 - \frac{\gamma}{3} \frac{v_{th,e}^2}{c^2}} - \frac{\omega_{pi}^2/\omega^2}{1 - \frac{\gamma}{3} \frac{v_{th,i}^2}{c^2}} = 0, \quad (5.7)$$

with γ the adiabatic exponent. The IAW experiences a resonance at the ion plasma frequency ω_{pi} . Since no propagation is possible for higher frequencies, $f_{pi} = \omega_{pi}/(2\pi)$ would constitute an upper limit for the width of the decay spectra in a parametric decay instability. Figure 5.21f shows ω_{pi} as a function of plasma density with the ion mass as parameter. The lighter the ion and the higher the density, the higher is the ion plasma frequency. In Fig. 5.22b the width of the decay spectra in the HF regime, $f_0 - f_{\text{high}}$, is compared with ω_{pi} deduced from the plasma density at the UHR of the corresponding discharge. Again the dashed line has a slope of 1. All gases, except helium, are located *above* this dashed line. Hence, f_{pi} seems to be too high for these gases. Since the ion plasma frequency constitutes only an *upper limit* for the allowed frequencies of the ion acoustic waves, this result fits the assumption that the ion acoustic wave is excited in the parametric instability. As in the case for the lower-hybrid waves, the full dispersion relation for the ion acoustic wave is also a function of k_x , which could be partly responsible for the observed broad spectrum. A detailed analysis is given in Ref. [22].

Both the ion acoustic waves and the lower-hybrid waves have a theoretical upper limit in frequency up to which they can propagate in the plasma. In the first case, it is the ion plasma frequency and in the second case the lower-hybrid resonance. The observed width in the spectra can be due to possible excitations of waves over the whole spectral range up to the respective limits. From both the Figs. 5.22a and 5.22b, it is at present not possible to decide if either the ion acoustic waves or the lower-hybrid waves is involved in the parametric decay instability. In principle, it is also possible that both candidates are involved.

An inherent feature of parametric excitation is that it only occurs above a certain power threshold. Therefore, an investigation was made to see if this power threshold exists in TJ-K as well. Figure 5.23 shows results from a power scan. For each of the working gases several frequency spectra are shown for the high-frequency regime. Each of the spectra corresponds to a different heating power, with the values given in each of the plots. The broad spectra that are achieved at maximum heating power indicate that the parametric decay process is far above its threshold. In TJ-K a lower heating power also changes the background parameters, hence it is difficult to find and isolate the power threshold. Nevertheless, a power scan has been performed and for each gas, similar results are found: With a decrease in heating power, the amplitude of the decay spectrum also decreases. The same is also true on the low-frequency domain, not shown here. For the case of hydrogen, for example, the amplitude of the sideband decreases by almost one order of magnitude

when decreasing the heating power from $P_{\text{abs}} = 1.4$ to 0.5 kW. Since the resulting decrease of the line averaged density is only 30 % with almost constant electron temperature, this indicates the non-linear behavior of this process.

According to the Manley-Rowe relations [155, 156], it is possible to estimate the maximum power transferred to the lower frequency component. Here, it is only a percentage of up to 2 % of the incident power, i. e. a power on the order of 30 W. Therefore, the parametric decay process itself does not play a significant role in the heating at the UHR. It could in principle contribute to heat the ions in TJ-K, which are at a temperature of $T_i \leq 1$ eV.

Sometimes the appearance of parametric instabilities is taken as an indicator for X-B conversion [28, 107]. In both these references, also a frequency component with a higher value than the frequency of the incident wave is detected. Since these components are not detected in TJ-K, the EBW seems not to play a role in the parametric instability described above.

5.9 Summary

The intention of this chapter was to explain the plasma generation and heating with 2.45 GHz at resonant magnetic field. The breakdown was observed with a multiple Langmuir probe array and found to occur at the electron cyclotron resonance layer, as expected. Centrally peaked plasma density profiles and hollow electron temperature profiles are achieved. The hollow-shaped temperature profiles indicate heating near the separatrix. The upper-hybrid resonance and the electron cyclotron resonance layer both usually lie near the separatrix. The cyclotron resonance can be excluded for absorption due to the low electron temperature. Hence, heating at UHR remains as the only candidate.

Estimations of the heating efficiency, using a global particle and power balance, also support heating at the UHR. It was shown that with increasing density, the UHR is shifted into regions of open magnetic field lines. Plasma production then becomes more inefficient due to parallel losses to the vacuum vessel wall along the open field lines.

Full-wave simulations were carried out which showed the importance of the vacuum vessel for efficient heating: Without the vacuum vessel geometry included in the calculations, an absorption of 12 % is found for X-mode injection and with the vessel walls included, the simulations yield an absorption of 80 %. In the simulations, an enhancement of the wave electric field at the UHR was found, which was furthermore shown to be toroidally extended. This enhancement has been successfully verified by measurements of the wave electric field with a small monopole antenna. Furthermore, power modulation experiments indicate the UHR as the position where the microwave power is deposited.

With both the monopole antenna and a small loop antenna it was possible to verify the existence of a parametric decay instability. This instability occurs at

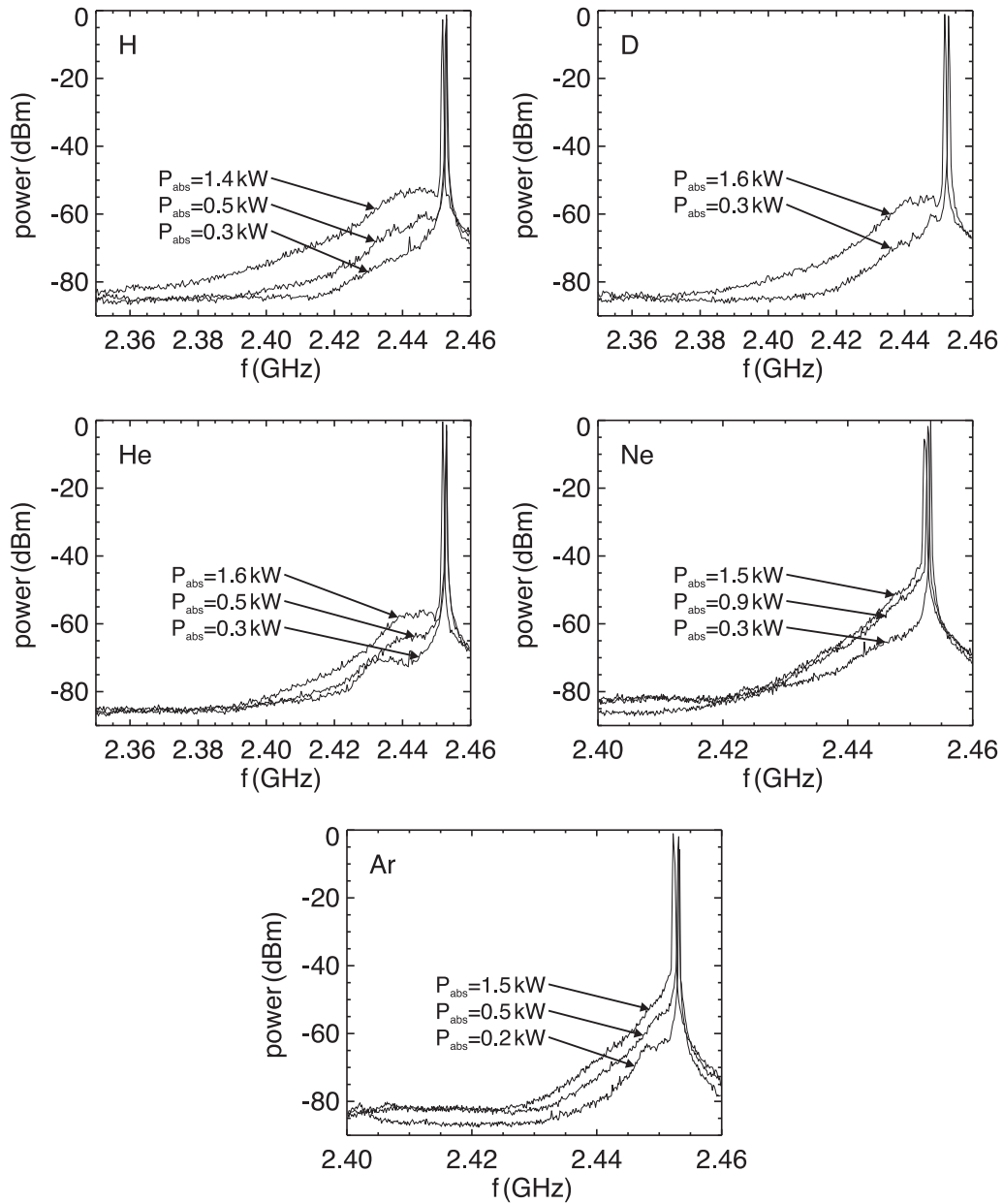


Figure 5.23: Frequency spectra for all working gases available in TJ-K with the power of the incident microwave as the parameter varied.

the UHR. The corresponding frequencies lie below the heating frequency, where the low frequency component is either due to ion acoustic waves or due to lower-hybrid waves, which both can in principle contribute to ion heating [158].

Summarizing, heating has been found to take place at the UHR. No direct evidence for the excitation of electron Bernstein waves could be found during the experiments.

Chapter 6

Heating plasmas at high magnetic field

In this chapter the production and heating of plasmas at high magnetic field is described. The term *high magnetic field* refers to field strengths of $B_0 \approx 0.3$ T, where the electron cyclotron frequency matches the frequency of the microwave system operating at $f_0 = 7.9 - 8.4$ GHz. This *resonant heating* scenario is first described (Sec. 6.1). Later, a heating scenario is described, in which additional heating with 2.45 GHz is applied to the plasma. This scenario, which has been discovered during this thesis, is referred to as *non-resonant heating*.

6.1 Resonant heating

The microwave source that provides a maximum power of 1.2 kW at a frequency of $f_0 = 7.9 - 8.4$ GHz is described in detail in Sec. 4.2.2. Here, the focus is on the investigations performed with this source.

6.1.1 Plasma breakdown

The oscillator–amplifier system allows for power modulation frequencies up to the MHz range. To study the initial plasma breakdown, the same analysis as for the low-field case (see Sec. 5.1) can be applied: The power was modulated with a frequency of $f_{\text{mod}} = 100$ Hz and the ion saturation current was obtained from the probe array SPIDER, shown earlier in Fig. 5.1.

Figure 6.1 shows the build-up of the poloidal plasma density profile during an argon discharge. Three snapshots in time are taken, which reveal basically the same behavior as in the low-field case: The density is first produced at the resonance layer and the flux surfaces that are connected to it, which results in a hollow density profile. The hollow shaped profile finally evolves to the typical, centrally peaked, profile. A detailed analysis can be found in Ref. [115].

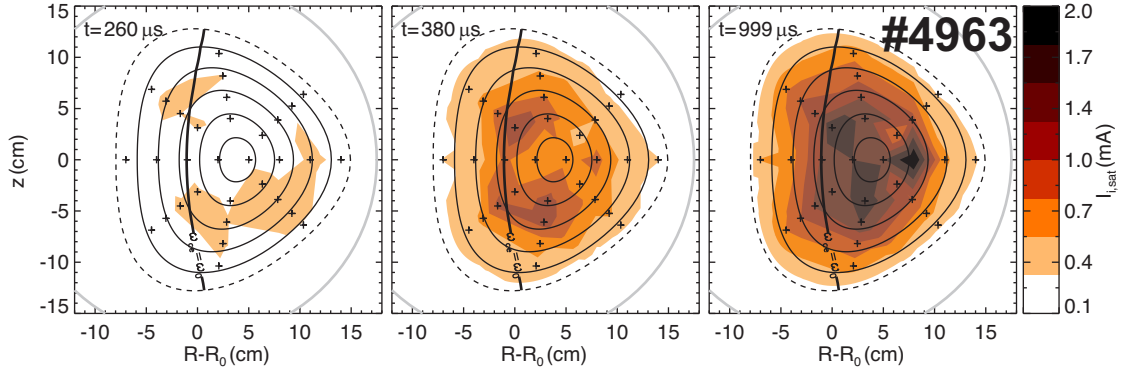


Figure 6.1: Plasma breakdown as a time series for an argon discharge ($B_0 = 277$ mT). Shown is the ion saturation current obtained from Langmuir probes located at the + signs, the time after switch-on of the microwave is indicated in the upper left side of the graphs. The flux surfaces are indicated as well as the fundamental resonance layer, $\omega_{ce} = \omega_0$. One can clearly see, how the breakdown happens at the resonance layer and the corresponding flux surface.

6.1.2 Equilibrium profiles

The array antenna (described in Sec. 4.2.2) replaced the original simple horn antenna which was formerly installed at the port T4 [121]. The reason was low coupling efficiency of the incident microwave power to the plasma. The combination of the phased array antenna and the tunable frequency of the 8 GHz heating source allows for a tunable angle of incidence (see Sec. 4.2.2 and the diploma thesis of H. Höhnle for details [88]). Since the theoretical predicted O–X mode conversion efficiency depends on the angle of incidence, as described in Sec. 2.4.1, the array antenna can be used to check if heating by EBW plays a dominant role in TJ-K. Similar EBW heating investigations, where a phased array of waveguides is used to scan the angles of incidence, have been recently performed on the MST reversed field pinch [128, 159].

Figures 6.2a and 6.2b show the density and electron temperature profiles of two helium and two argon discharges, respectively. The angle of incidence of the microwave was varied between the two discharges: shots #6683 and #6696 correspond to perpendicular injection and shots #6691 and #6695 correspond to injection at the calculated optimum angle. The influence of the background magnetic field and the electron temperature is accounted for in the computation of the density profile, as described in Secs. 4.3.1 and 5.2.

The profiles are sampled only up to the plasma center, because it turned out that, only in the high-field discharges, the probes can cause a significant decrease in the density (up to 50%) if they go beyond the plasma center. Compared to the low-field discharges discussed in Sec. 5, the high-field discharges seem to have similarly shaped density profiles, while the shape of the electron temperature profiles is less hollow. As will be shown below, this is due to the fact that the UHR lies further in

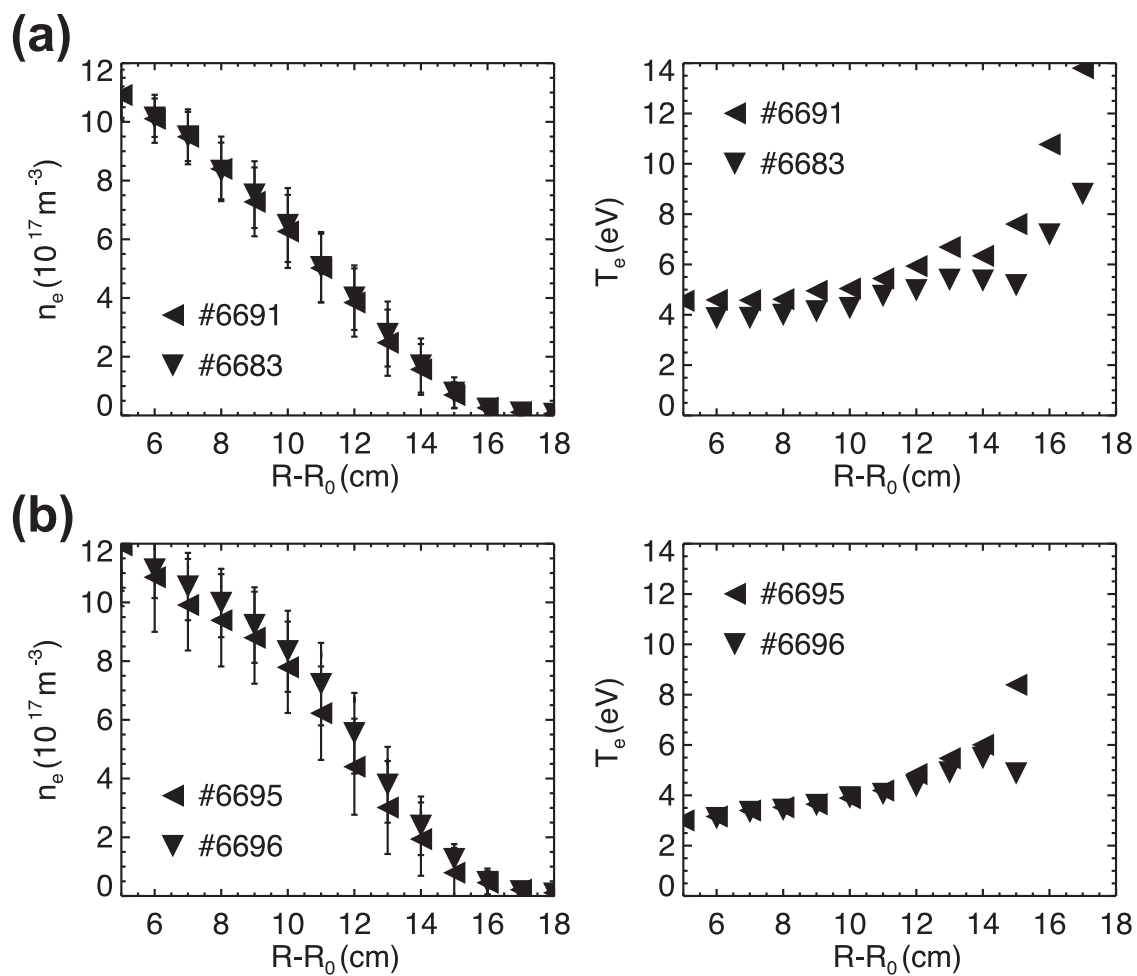


Figure 6.2: Profiles of the plasma density (left) and the electron temperature (right) for (a) two helium discharges and (b) two argon discharges at different injection angles. For shots #6691 and #6695 the heating frequency was $f_0 = 8.0$ GHz and for shots #6683 and #6696 it was $f_0 = 8.14$ GHz.

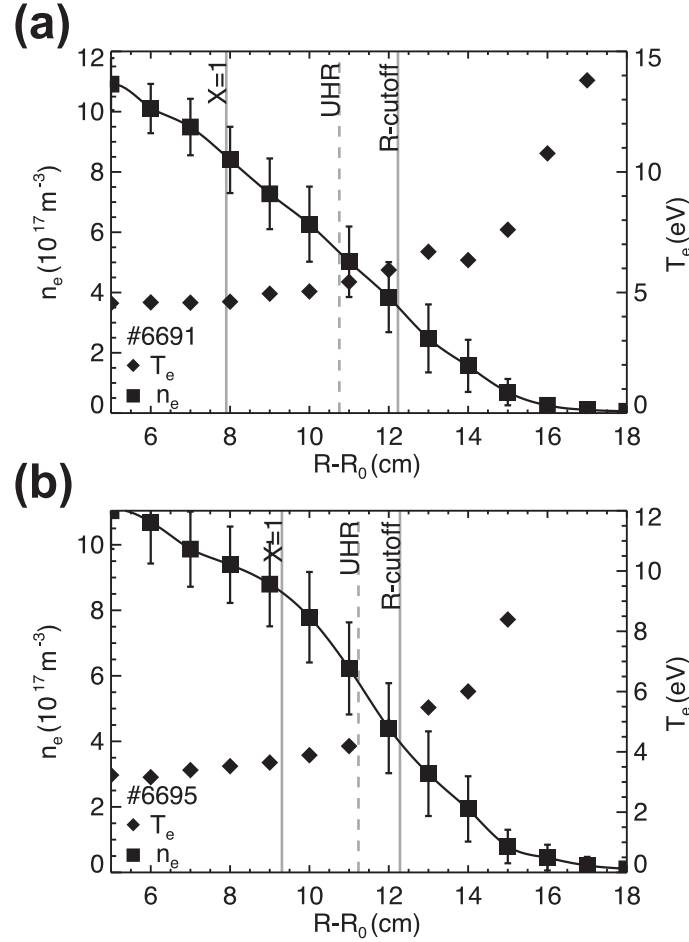


Figure 6.3: Radial density profile from (a) #6691, a helium discharge and (b) #6695, an argon discharge. For both discharges, f_0 was set to 8.0 GHz. Filled squares represent measured density values and the thick curve a spline curve fitted to them. Filled diamonds depict measured electron temperatures. Cutoffs and resonances are labeled in the graph.

the plasma center.

The density profiles for the different antenna angles basically look the same. Hence, no effect of sweeping the angle of incidence can be deduced from the n_e profiles. Regarding the T_e profiles, one can identify a slight increase of the temperature for the case of optimum injection. A slightly increased coupling efficiency between the incident microwave and the plasma can be therefore concluded for the optimum injection angle. The lack of a clear effect excludes substantial heating by the EBW. Therefore, it is necessary to analyze the profiles in terms of the positions of the cutoffs and resonances.

Figures 6.3a and 6.3b show the equilibrium profiles from the two shots #6691 and #6695 (corresponding to optimum incidence and also shown in Fig. 6.2) together with the position of their cutoffs and resonances. The solid line, connecting the measured density values, represents a spline fit to these values. Both shots are

characterized as overdense, and O-X mode conversion should therefore be in principle possible. Nevertheless, their peak densities lie only slightly above the cutoff density, marked by the $X = 1$ line in the graphs. Hence, the area enclosed by the cutoff layer, that is the area of overdense plasma, is relatively small. In Sec. 3.3.1 it was shown that the O-X conversion takes place over a finite spatial distance, reaching behind the nominal O-mode cutoff layer. In other words, the conversion *needs* a region of finite spatial width to be effective. From this observation, at best only very small conversion efficiencies can be expected. This issue is addressed in detail with full-wave simulations in Sec. 6.1.5.

Since it is now clear that heating due to EBW is not expected to play a dominant role in this regime, two candidates remain as possible heating mechanisms: absorption at the cyclotron resonance or at the upper-hybrid resonance. For the plasma parameters achieved, namely the low electron temperatures, the expected absorption of the O- and X-mode at the cyclotron resonance is below 0.1 % [2] and, hence, negligible. This leaves heating at the UHR as the possible process for the plasma production. The antenna configuration is such that it radiates in O-wave polarization, which is not the optimum configuration for this heating scenario. However, one must follow the microwave after it leaves the antenna: It is a linearly polarized O-wave, which excites both the O- and X-mode when entering the plasma [7, 38]. The excited X-mode can then be absorbed at the UHR. Furthermore, if an O-mode is reflected at an appropriate angle at the vacuum vessel wall, it is also mode-converted into an X-mode, as described in Sec. 5.5.1.

6.1.3 Scaling of plasma parameters

In general, slightly higher densities and similar electron temperatures are achieved as compared with the low field discharges (see Sec. 5.3). The connection between the density and the incident power is illustrated in Fig. 6.4: During a helium discharge, the incident power was ramped up stepwise. The density values shown are obtained from microwave interferometry measurements. One can clearly see, how the density increases with increasing microwave power, reaching values of $\bar{n}_e \approx 4 \cdot 10^{17} \text{ m}^{-3}$. The density scaling is seen to saturate at this value.

The scaling of the density as a function of the background magnetic field is depicted in Fig. 6.5. The magnetic field was first ramped up from $0 \rightarrow 276 \text{ mT}$ over a time of $\Delta t = 20 \text{ s}$ and then ramped down in the same time interval. Both processes are labeled by arrows in the plot. The incident microwave power was kept at a constant level of $P_{in} = 1000 \text{ W}$ and the working gas was helium. An increase of the density with increasing B_0 can be clearly seen with an asymptotic behavior towards the same density value as in Fig. 6.4.

A most important result is the hysteresis, which requires a value of $B_0 \geq 200 \text{ mT}$. For lower values, it was not possible to start a plasma. This can be understood because at this magnetic field strength, the cyclotron resonance ω_{ce} is at the inner vacuum vessel wall and the breakdown needs to take place at ω_{ce} , as described in

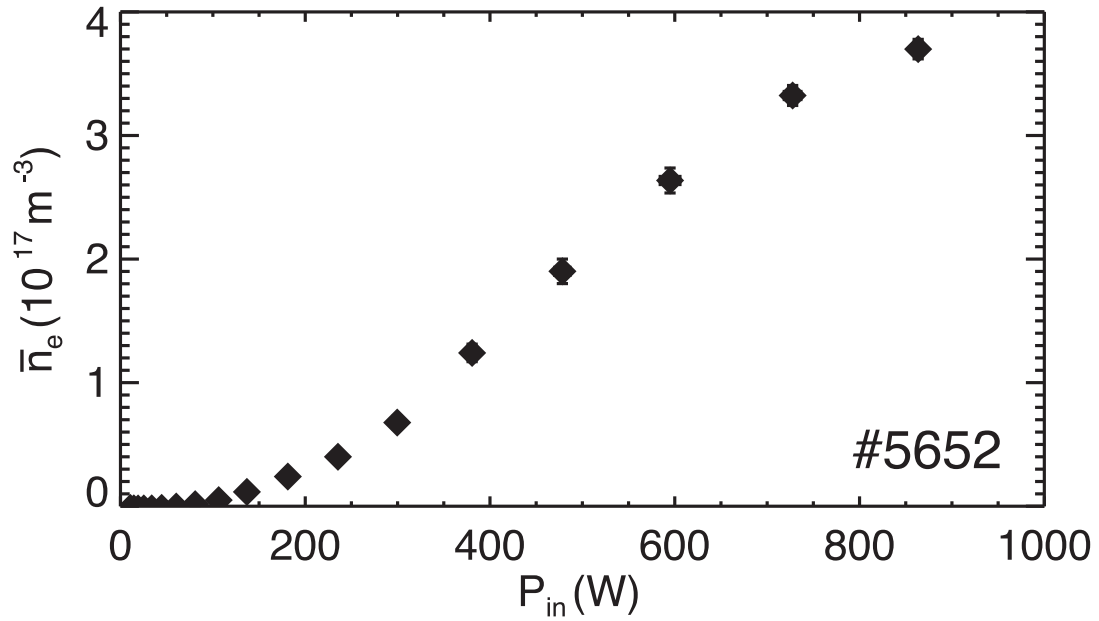


Figure 6.4: Line averaged plasma density as a function of the incident microwave power at $f_0 = 8.3$ GHz. Magnetic field was set to $B_0 = 276$ mT and the working gas was helium.

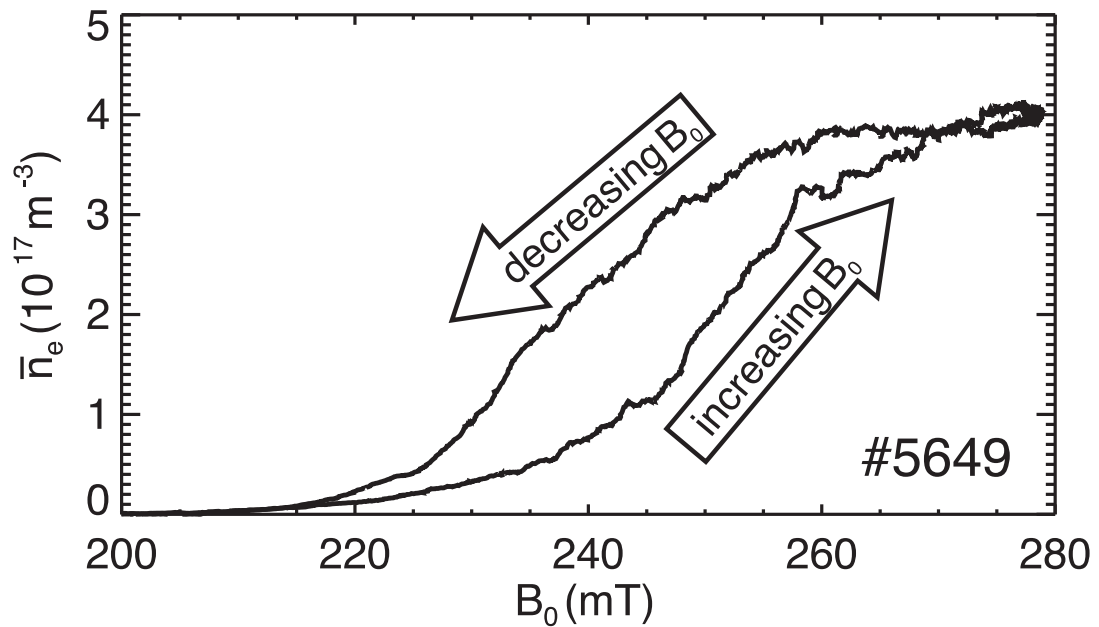


Figure 6.5: Line averaged plasma density as a function of the background magnetic field. The incident power at $f_0 = 8.3$ GHz was kept at a constant power level of $P_{in} = 1000$ W and the working gas was helium.

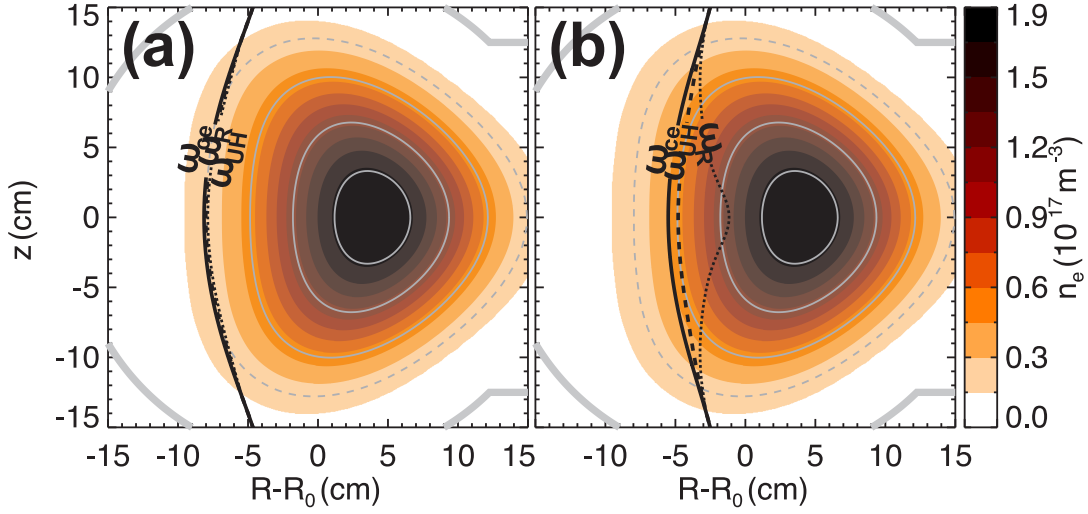


Figure 6.6: Poloidal density profiles obtained from Eq. (5.2) with the positions of the resonances and cutoffs as labeled in the graphs for (a) $B_0 = 220$ mT and (b) $B_0 = 240$ mT. The absolute values of the density correspond to experimental values during the ramp-up phase as depicted by Fig. 6.5.

Sec. 6.1.1. With increasing B_0 the cyclotron resonance moves further inwards.

To understand the hysteresis one has to consider the influence of B_0 on the positions of the cutoffs and resonances. Figure 6.6 shows poloidal density profiles, as obtained from fits to experimental data using Eq. (5.2), with the resonances and cutoffs overlaid for two different values of the magnetic field strength. Figure 6.6a and 6.6b correspond to 220 and 240 mT, respectively. To isolate the effect of increasing B_0 , the peak density is set to the same value for both profiles, corresponding to a value lying inbetween the densities reached for 220 and 240 mT as shown in Fig. 6.5. For the case of the lower magnetic field, the UHR is situated at the same position as the cyclotron resonance, which itself is located on open flux surfaces, where only very low densities are achieved. No effective heating is therefore to be expected in this case. From Fig. 6.6b one can see that with increasing values of B_0 , the cyclotron resonance moves inwards into regions of closed flux surfaces and increasing density. According to Eq. (2.29) this leads to a separation of the UHR and the cyclotron resonance, and the UHR is shifted further inwards. Hence, heating at the UHR becomes more effective and an increase in plasma density is to be expected as observed in Fig. 6.5.

When the magnetic field is decreased again, the density stays longer at its maximum level than expected from the time span with increasing magnetic field, i. e. a hysteresis is observed. This can be understood from the same analysis as for the ramp-up procedure of B_0 . Figure 6.7 shows two poloidal density profiles for (a) $B_0 = 276$ mT and (b) $B_0 = 250$ mT with the density values taken from Fig. 6.5. The only noticeable difference between the two case is that the cyclotron resonance is shifted to the left. The position of the UHR and the distance between the UHR

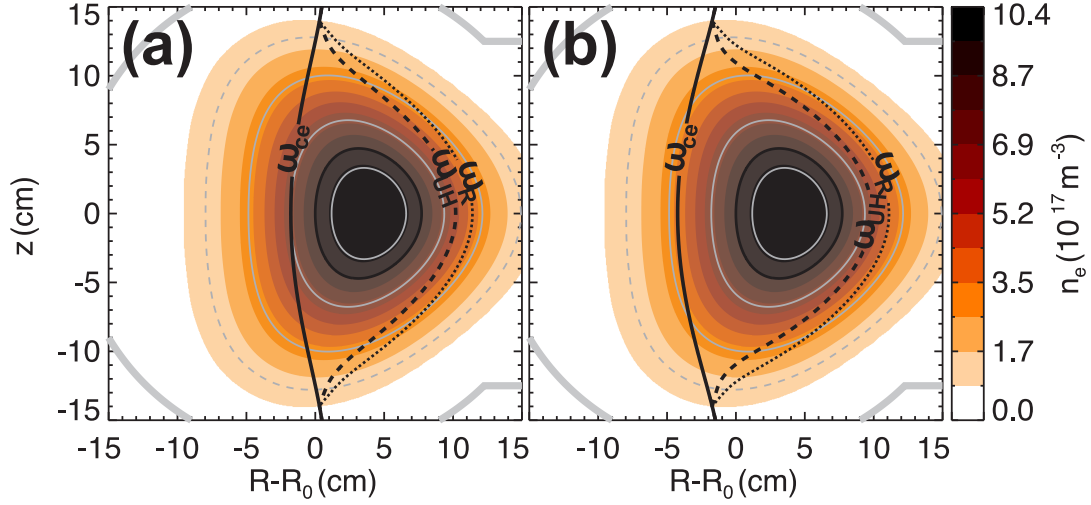


Figure 6.7: Poloidal density profiles obtained from Eq. (5.2) with the positions of the resonances and cutoffs as labeled in the graphs for (a) $B_0 = 276$ mT and (b) $B_0 = 250$ mT. The absolute values of the density correspond to experimental values during the decrease of B_0 as depicted by Fig. 6.5.

and the R-cutoff (which is an evanescent region for the X-mode) is basically the same. Hence, no change in the heating efficiency is expected from this analysis and is also not observed in the experiment, as shown in Fig. 6.5. With a further decrease in the magnetic field at the same density, the cyclotron resonance moves further to the left and the position of the UHR starts to detach from it and forms a closed line around the plasma center (not depicted). The same applies to the R-cutoff, which forms a similar shape around the UHR. This results in a more efficient shielding of the UHR by the R-cutoff, since now the wave cannot penetrate to the UHR from the high-field side (left side in the plots) anymore. This in turn, results in less efficient heating and, finally, in a decreased density. The decreasing density leads to an increasing gap between the UHR and the R-cutoff, which leads to an even less efficient heating. Ultimately, this results in the extinction of the plasma as soon as the magnetic field falls below a certain value.

6.1.4 Estimation of the heating efficiency

The particle and power balance presented in Sec. 5.4 can be also applied to the discharges heated with 7.9 – 8.4 GHz at high magnetic field. A comparison with the experimental data then gives a quantitative estimate of the absorbed heating power.

Figure 6.8 shows experimental data obtained from a series of argon discharges for a neutral gas pressure of $p_0 = 2$ mPa. Different heating powers are indicated by different symbols. The shaded area marks the accessible parameter range as obtained from the balance equation (5.1). The boundary values of the input power

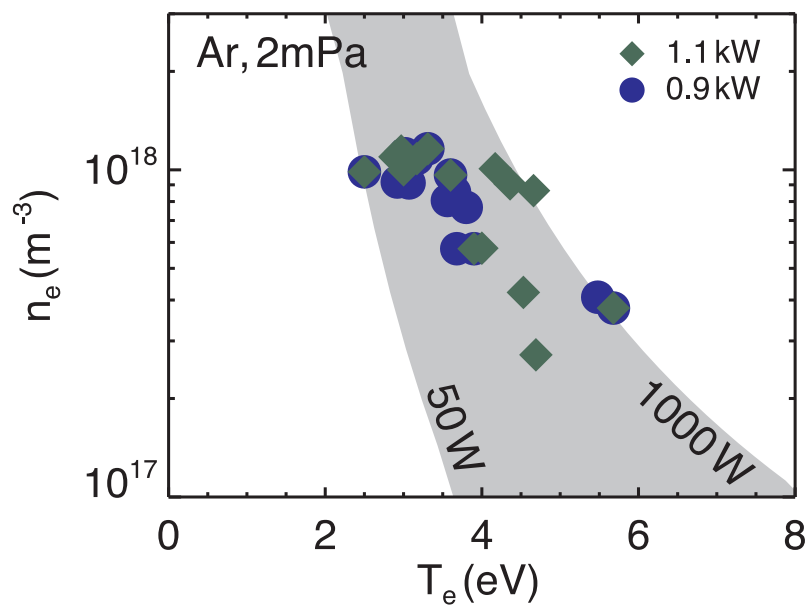


Figure 6.8: Central electron density as a function of the central electron temperature for a series of argon discharges with a neutral gas pressure of $p_0 = 2 \text{ mPa}$. Symbols indicate data obtained from measurements, where different colored symbols account for different absorbed power. Shaded area indicates values obtained from the global particle and power balance, Eq. (5.1), where the input power has been varied in the range given by the values in the graphs.

are given in the plot, where the area is chosen to include all experimental values.

The trend of decreasing temperature with increasing density that was found in the low field discharges, is also found in Fig. 6.8. A spread of the experimental values can be seen with a few discharges located at the lower border and a few located at the upper border of the shaded area. Since all of the discharges were performed with a microwave power of 900 W or above, a localization at the lower border corresponds either to very inefficient heating on open flux surfaces or to an underestimation of losses due to conduction, according to the analysis in Sec. 5.4. In the previous section it was shown that heating, in the case of the high density and, hence, high magnetic field, is not expected to take place on *open* flux surfaces (see Fig. 6.7b). Thus, it is more likely that discharges with high densities and low electron temperatures have higher losses due to conduction than discharges with lower density and higher temperature.

A quantitative analysis for the other working gases is not presented here, due to the lack of a large enough database. Only very few high field discharges can be performed per day due to the high currents that are necessary to sustain the background magnetic field. With values of 1200 A this requires a significant cooling time of the magnetic field coils. From the available data it is concluded that the behavior of the other working gases seems to follow the same rules as for the argon discharges.

6.1.5 Full-wave simulations

To investigate the interaction of the incident wave with the plasma, simulations have been carried out in the poloidal cross section, where the array antenna is located. The density and the background magnetic field profiles were set according to the parameters of the discharges shown in Fig. 6.2. A Gaussian beam with a beam waist of $w_0 = 1.4\lambda_0$ is used in the simulations. This value was chosen to get the best approximation for one of the H-plane sectoral horns of the array antenna (see Sec. 4.2.2). The computational grid size was set to $\delta \approx 0.28$ mm.

Figure 6.9a shows the rms-value of the wave electric field after 50 oscillation periods without the inclusion of the vacuum vessel walls of TJ-K. The steady state solution is achieved at this time. As one can see, the microwave lens, shown in Fig. 4.6, was included in the simulations. Details on the inclusion of the lens are given in Appendix A.2. The angle of incidence was set to 43° with respect to the toroidal direction, corresponding to the calculated optimum injection angle for O-X mode conversion efficiency. A single pass absorption of 17 % is found for this case. A small enhancement of the wave electric field around the UHR can be seen, indicating localized power dissipation. Since the antenna emits an O-wave, this dissipation is due to partial O-X conversion and the subsequent absorption of the generated X-mode at the UHR. The small degree of absorption is due to the relatively low density, leading to an O-mode cutoff layer, which encircles only the very center of the plasma. As noted before, in order to convert the wave into an X-mode, which

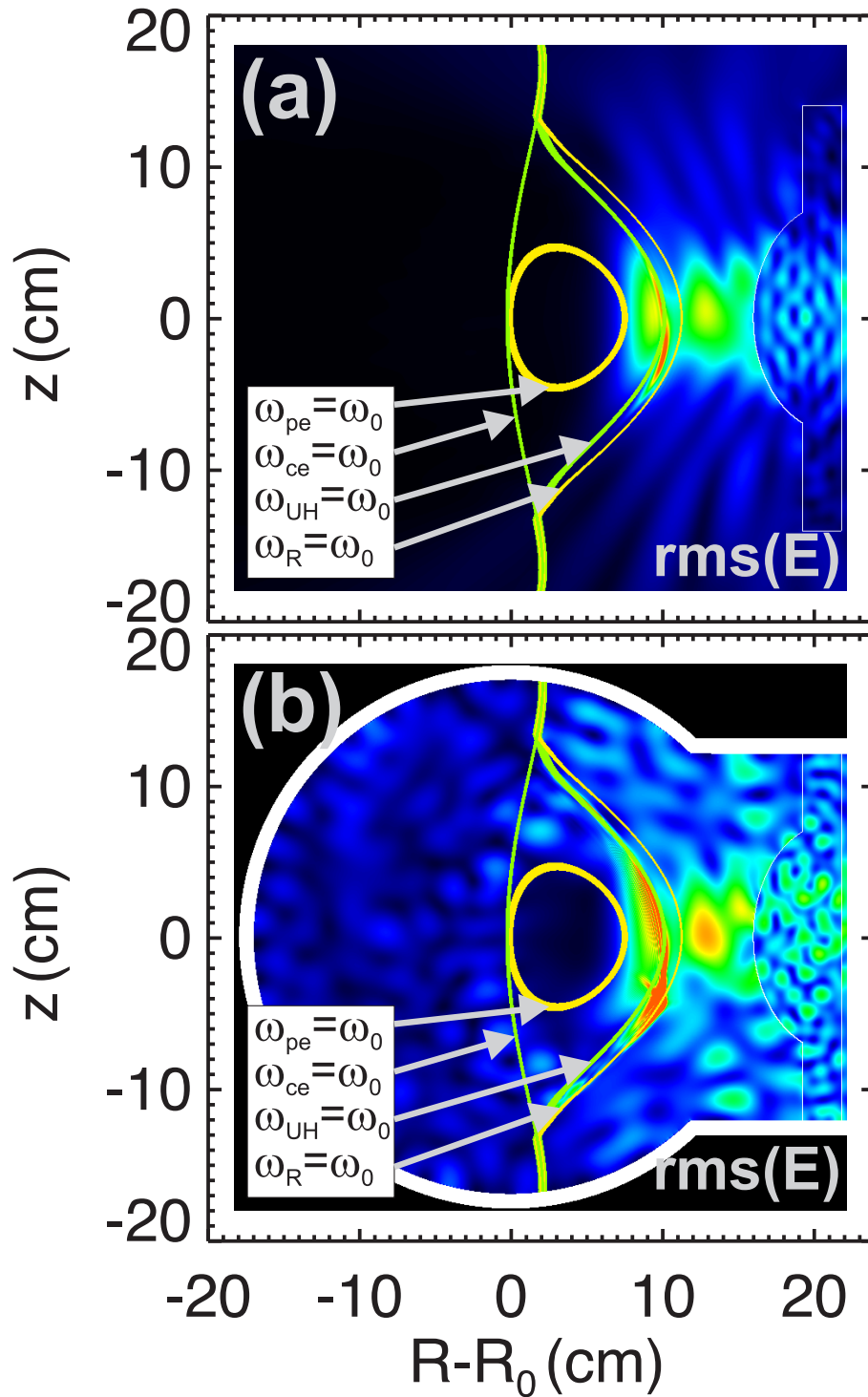


Figure 6.9: Simulation of the 8 GHz heating scenario in the poloidal cross section where the array antenna is located. Shown is the rms-value of the wave electric field for (a) the case without and (b) with the vacuum vessel walls of TJ-K included in the calculation.

then can be absorbed at the UHR, sufficient additional volume behind the O-mode cutoff is required (see Fig. 3.3). Obviously, this amount of space is not available.

The inclusion of the vacuum vessel wall leads to an increase of the absorbed power to 26 %. Figure 6.9b shows the corresponding calculation result after 150 oscillation periods. The enhancement around the UHR layer is now stronger as compared with Fig. 6.9a. The non-absorbed power during the first pass of the UHR layer is reflected at the vacuum vessel and partly absorbed during the second pass at the UHR layer. In contrast to the low-field case, only a small increase in the absorbed power is found. This is due to the different antenna geometry: In the low-field case, the microwave was injected through a small antenna aperture. Since the walls of the vacuum vessel surrounded the calculation grid, the only way the wave can leave the grid, is through the antenna which is taken to be terminated by a perfect absorber. In the high-field case, the antenna has a bigger aperture. Hence, a larger percentage of the wave energy is lost. A smaller number of traverses across the UHR layer take place, which results in less absorption.

6.1.6 Summary

With a multiple Langmuir probe array, the plasma breakdown was found to take place at the electron cyclotron resonance layer. Equilibrium profiles are achieved with higher densities but similar electron temperatures as compared to the low-field discharges. A hysteresis in the scaling of the line averaged density with increasing versus decreasing magnetic field was found and could be successfully explained by considering the respective positions of the cutoffs and resonances. No noticeable effect of sweeping the angle of incidence of the microwave beam was found. Although care has been taken to inject the microwave beam at the optimum angle for O-X mode conversion and to match the curvature of the wavefront to the curvature of the conversion layer, no clear evidence for an excited EBW was found. From measured density profiles and full-wave simulations, one can conclude that this is due to the low density, which achieves only slightly higher values than the corresponding cutoff density of the microwave. Power deposition at the UHR layer is the likely candidate for plasma heating. Excitation of EBW does not play an important role, but cannot be fully excluded.

An upgrade of the heating power should increase the density and, hence, the mode conversion efficiency. With this upgrade that is planned to be available in summer 2010, a pronounced effect of sweeping the injection angle of the microwave beam is to be expected.

6.2 Non-resonant heating

In this section, a new operational regime is described. It has been discovered during this thesis and is first described in the diploma theses of H. Höhnle [88] and

G. Birkenmeier [116]. It is referred to as *non-resonant heating*, since both the cyclotron and upper-hybrid resonances are not located in the plasma. Nevertheless, a plasma with a considerably higher density than in the resonant case can be sustained.

The question arises, if a type of plasma waves, not considered before, exist for the discharge parameters in this new regime. In the diploma thesis of P. Diez [160] it was investigated, whether the non-resonant heating could be due to heating at the so-called *O-resonance*. This resonance has been predicted theoretically in the early 70s [161, 162] and experimentally verified in linear plasma devices [163, 164, 165]. Coupling to this resonance is only possible for right-handed circularly polarized waves propagating inside the plasma (above the O-mode cutoff density). In Ref. [160] it was shown that coupling to this resonance for the antenna position in TJ-K is not possible.

Although the detailed mechanism of the non-resonant heating is not fully understood at the moment, the present state of knowledge is presented in the following sections.

6.2.1 Plasma breakdown

In Sec. 6.1, the resonant heating regime at high magnetic field was described. In this case the achieved density is too low, to expect heating by EBW and, hence, a noticeable effect of sweeping the angle of incidence. In order to increase the density, it was tried whether additional heating with $f_1 = 2.45$ GHz has an effect in the high-field discharges. Surprisingly, although 2.45 GHz is far below the electron cyclotron frequency in the plasma, an additional heating effect was observed. This effect is reproducible, being confirmed by measurements at the WEGA stellarator in Greifswald [166, 167].

In TJ-K, the achieved density was still too low to get an effective O-X conversion efficiency for the 8 GHz power. However, it was found that the magnetron at 2.45 GHz can sustain the discharge alone, even if the 8 GHz source is switched off, as described first in Ref. [168]. This process is illustrated in Fig. 6.10. The line averaged density, the injected 2.45 GHz power and the injected 8.3 GHz power of an argon discharge (#6439) are plotted as a function of time. The magnetic field was kept constant at a value of $B_0 = 276$ mT. The plasma is started with 8.3 GHz and a power of 0.5 kW. After a time of 18 s, the 2.45 GHz is injected into the plasma with a power of 1.6 kW. The additional heating manifests itself as an increase of the density. After the 8.3 GHz heating is switched off the plasma stays at its high density level. In this case, the line averaged density even rises to considerably higher values, after the 8 GHz power is switched off. This could be due to a relatively small change in the shape of the equilibrium profile which leads to an increased matching of the plasma to the 2.45 GHz microwave which then results in increased plasma density. The density values achieved in these discharges clearly exceed the values in the low-field discharges (cf. Sec. 5.3). Although the breakdown is shown here for

argon only, the non-resonant heating regime was also found with the other working gases.

Note that it is not possible to start a plasma at the high magnetic field with f_1 alone. Also, a minimum density value is required before the non-resonant heating process starts to operate. This density is produced with the 8 GHz heating system. To determine the value of the minimum density, power modulation experiments have been carried out, in which the power of the 8 GHz was modulated with a triangular wave, in order to continuously increase the plasma density, whereas the power of the 2.45 GHz was modulated in phase with a square wave. This process is illustrated in Fig. 6.11 for a helium discharge where the modulation frequency was set to $f_{\text{mod}} = 97$ Hz and the data was acquired with a sampling rate of 1 MHz. The signals shown in Fig. 6.11 are averaged over 100 modulation cycles.

The density threshold, where non-resonant heating starts, can be identified by the first change in the slope of the density trace. As a guide to the eye, different slopes are highlighted by thick colored lines. The first change in the slope happens at $t \approx 2$ ms and a density value of $\bar{n}_e \approx 7 \cdot 10^{17} \text{ m}^{-3}$, which roughly corresponds to the O-mode cutoff density of f_1 . A local maximum in the density is found at this point. Since the signals shown in Fig. 6.11 are averaged over 100 modulation cycles, this local maximum is not an artefact. The physical mechanism behind this phenomenon is not yet clear.

An additional jump in the slope of the density increase occurs, when the 8 GHz power is further ramped up and, hence, the plasma density is further increased. As can be seen from Fig. 6.11, this additional increase in the slope occurs at $t \approx 4$ ms. The corresponding density is roughly the L-cutoff density.

From the above results, the importance of the cutoffs of the 2.45 GHz has become obvious for the non-resonant heating regime. An attempt to explain this behavior is made in Sec. 6.2.5.

6.2.2 Scaling of plasma parameters

In addition to the initial density as a requirement for the non-resonant heating to take place, a second important parameter is found to exist: the background magnetic field B_0 .

The scaling of the density with B_0 is depicted in Fig. 6.12. The magnetic field is first ramped up in 20 s to 276 mT and then ramped down over the same time span. As soon as the maximum value of B_0 is reached, 2.45 GHz heating is applied and one can see the resulting increase from $\bar{n}_e = 4 \cdot 10^{17}$ to $6 \cdot 10^{17} \text{ m}^{-3}$. Before the down-ramping starts, the 8.3 GHz power is switched off.

During the decrease of B_0 the density stays at a constant level until the field reaches 190 mT, where a sudden drop in the density is observed. At $B_0 \approx 175$ mT the discharge cannot be sustained any longer. The disappearance of the plasma is due to the fact that, at this field strength, the cyclotron resonance is approaching the plasma from the low-field side. Hence, the R-cutoff, which is always located at a

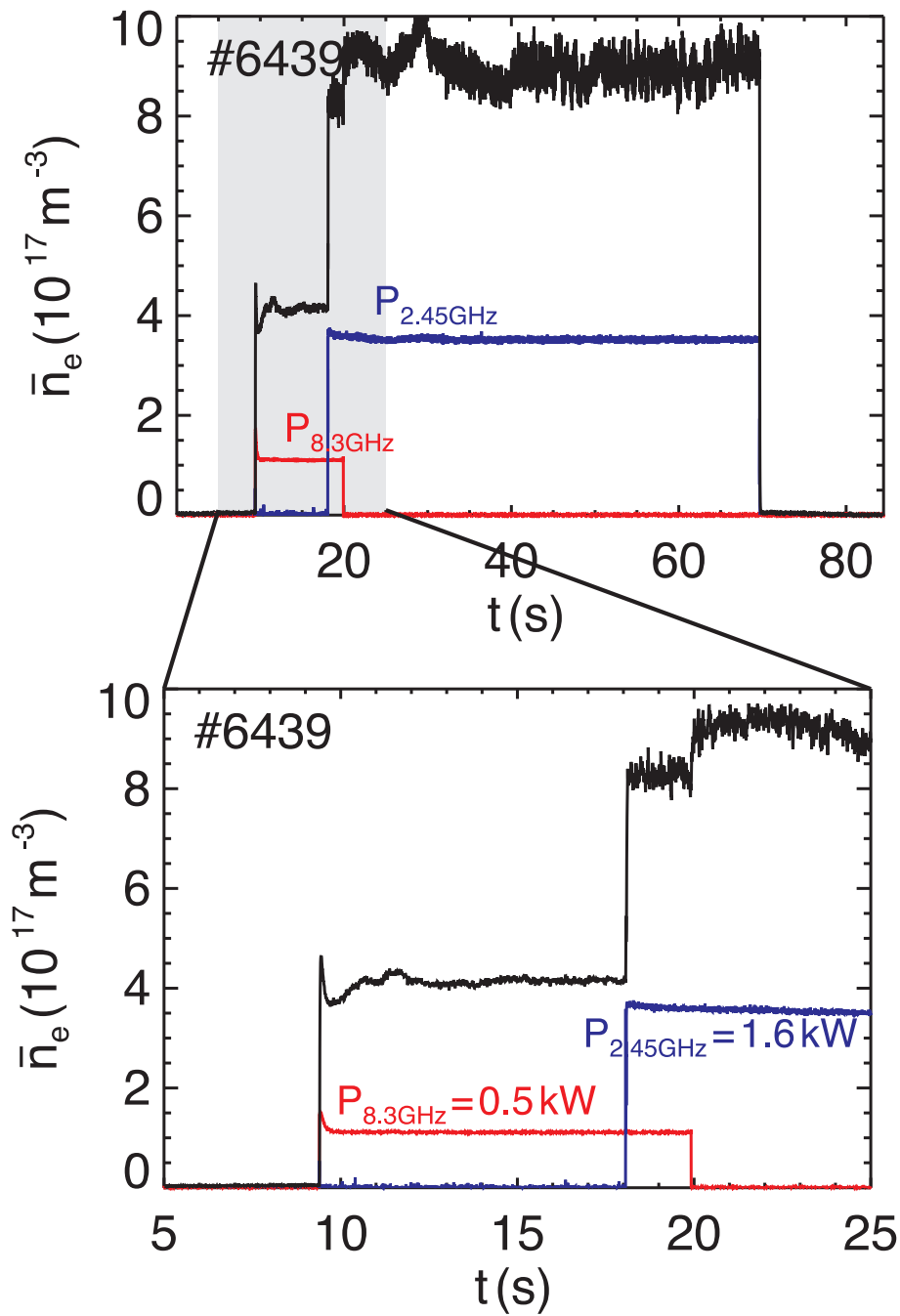


Figure 6.10: Time traces of the line averaged density, the injected 8 GHz power and the injected 2.45 GHz power of an argon discharge (#6439) with a magnetic field strength $B_0 = 276 \text{ mT}$. (a) The complete discharge and (b) a zoom into the time span, in which the breakdown takes place.

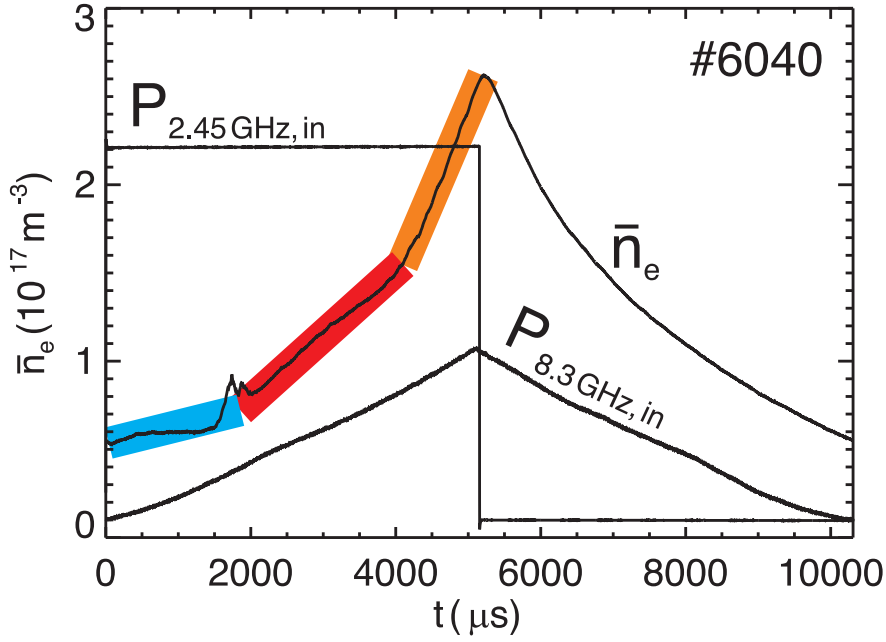


Figure 6.11: Line averaged density, injected 8.3 GHz power and injected 2.45 GHz power obtained during power modulation experiments in a helium discharge (#6040). The signals are averaged over 100 modulation periods. The phase of increasing density can be separated into three parts of different slopes, depicted by the thick different colored lines.

lower field strength than the cyclotron resonance, approaches the plasma boundary, too. This leads to a shielding of the microwave by the R-cutoff at decreasing field strength. Eventually, this results in the total reflection of the microwave in front of the antenna and energy can no longer be delivered to the plasma to sustain the discharge.

Figure 6.13 shows the line averaged plasma density as a function of the neutral gas pressure for a series of non-resonant helium discharges. An increase with increasing pressure can be clearly seen. For low pressure values that are slightly above 10 mPa, a very steep increase is observed. The increase in pressure leads to higher ionization rates and, hence, the plasma density increases. A maximum density value seems to be reached around $p_0 = 50$ mPa. If the pressure is too high, convective losses become important and the density starts to decrease.

6.2.3 Power deposition studies

As in Sec. 5.7, power modulation experiments have been carried out, to locate the power deposition during non-resonant discharges. The injected microwave power was modulated with the highest modulation frequency possible with the magnetron, $f_{\text{mod}} = 29.7$ kHz. The power deposition can be deduced from the amplitude of the

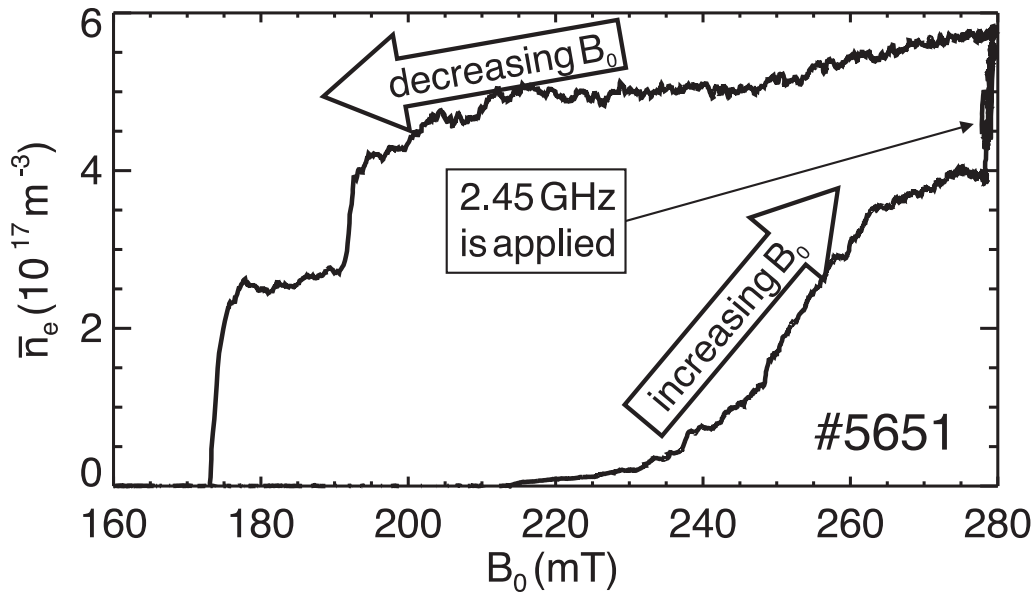


Figure 6.12: Line averaged plasma density as a function of the background magnetic field. The injected power at 2.45 GHz is switched on, when the maximum field is reached, and the injected power at 8.3 GHz is switched off then. The working gas was helium.

density modulation, where higher amplitudes correspond to higher power deposition rates.

Figure 6.14 shows power deposition profiles and the respective plasma density profiles for three different heating powers, as indicated in the plot. The discharges were all performed with argon as working gas at a magnetic field of $B_0 = 266$ mT. With increasing heating power, the density increases, as can be seen from Fig. 6.14b. Dashed lines indicate the O-mode and the L-cutoff densities. One can see how the position of both cutoffs moves outwards with increasing heating power.

A clear peak is found in each of the power deposition profiles. These peaks move radially outwards with increasing heating power. The position of the maximum modulation amplitude corresponds within the error bars to the position of the L-cutoff. Hence, the microwave power of the 2.45 GHz must be deposited around the L-cutoff layer. Consequences of these findings are discussed in Sec. 6.2.5.

For the other working gases, the shape of the equilibrium profiles is basically the same. Similar behavior as those presented for argon can be expected.

6.2.4 Toroidal currents

Also in stellarators toroidal net currents can be present. They are either due to direct interaction of an incident electromagnetic wave with the plasma particles [169] or due to internal plasma currents, which are bootstrap currents [170] or a combination of bootstrap and Pfirsch-Schlüter currents [171, 172]. The net currents can be measured by using so-called *Rogowski coils*. A Rogowski coil is a flux-to-voltage transducer,

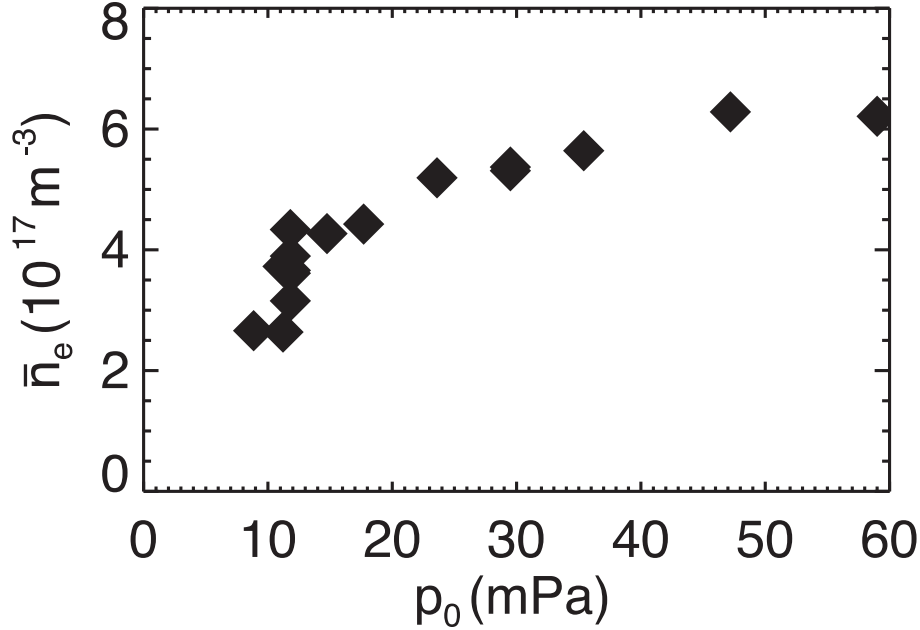


Figure 6.13: Line averaged plasma density as a function of the neutral gas pressure for a series of non-resonant helium discharges.

which allows for non-invasive measurements of toroidal net currents [173, 174].

For TJ-K an external Rogowski coil has been constructed. With this coil, toroidal net currents of the order of $I = 1$ A have been measured in low-field discharges [175]. This value is rather low compared to the currents in the helical coils (up to $I_{\text{hel}} \approx 120 \cdot 1$ kA) and could only be resolved during power modulation experiment with synchronous detection using lock-in amplifiers. In the non-resonant heating regime, remarkably higher currents are measured as shown in Fig. 6.15, where the toroidal current is given as a function the plasma density for a series of helium discharges.

From measurements of the energy content with a diamagnetic loop [176] it is apparent that a non-thermal component of electrons must exist in the plasma. The assumption of a purely Maxwellian distribution function of the electrons would lead to an unrealistic high electron temperature of $T_e \geq 100$ eV, which was not measured.

The existence of a non-thermal electron component is confirmed by the measurement of a small amount of ionizing radiation with a commercial radiation detector, which is only sensitive to radiation energies higher than 10 keV. This radiation is thought to be due to the component of non-thermal electrons. These non-thermal electrons and the toroidal net current are found only in this operational regime, hence, it is likely that the current is partly carried by the energetic electron component.

As shown in Fig. 6.15, the current decreases with increasing plasma density. At higher density the collision time of the fast electrons decreases [4], which results

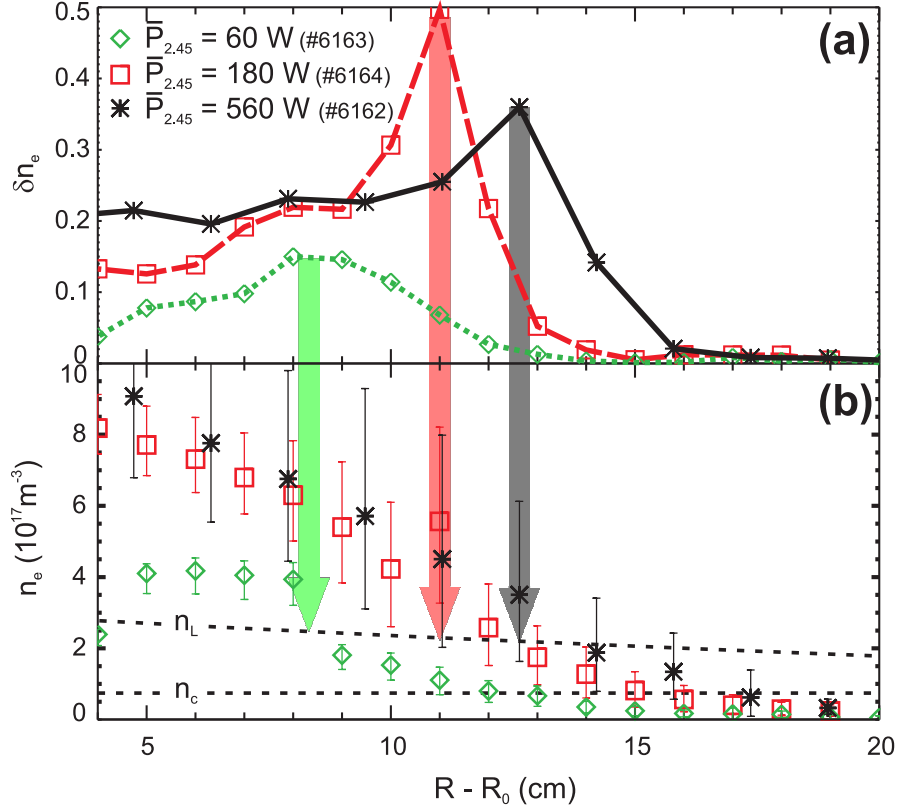


Figure 6.14: (a) Density modulation amplitude corresponding to power deposition obtained during power modulation experiments with $f_{mod} = 29.7$ kHz. (b) Density profiles with the O-mode cutoff density and the L-cutoff density. In (a) and (b) different colors correspond to different heating powers, as labeled in the upper right corner of the graph. (Adapted from Ref. [160].)

in a decrease of the current. It is therefore concluded that the underlying physical mechanism of the current depends strongly on the electron collision time.

In principle, two candidates exist that can cause the toroidal net current. One candidate is the bootstrap current and the other is a current directly driven by the incident microwave. In order to generate a bootstrap current inside the plasma, the contributing particles must be either in the so-called *banana regime* or in the *plateau regime*, that is the collision times must be longer than the time it takes for a trapped particle to travel between two reflection points [47]. In TJ-K for the bulk electrons this is certainly not the case, but for the non-thermal electron component the requirement can be fulfilled. Nevertheless, at the magnetic field strengths of only 300 mT, trapped electrons having energies above 10 keV are lost quickly. It is unlikely that they can contribute to a toroidal net current.

For the second candidate, i. e. current drive by the microwave, the wave beam needs to have a preferential direction of propagation with respect to the direction of the magnetic field, otherwise the generation of a toroidal net current is hard to

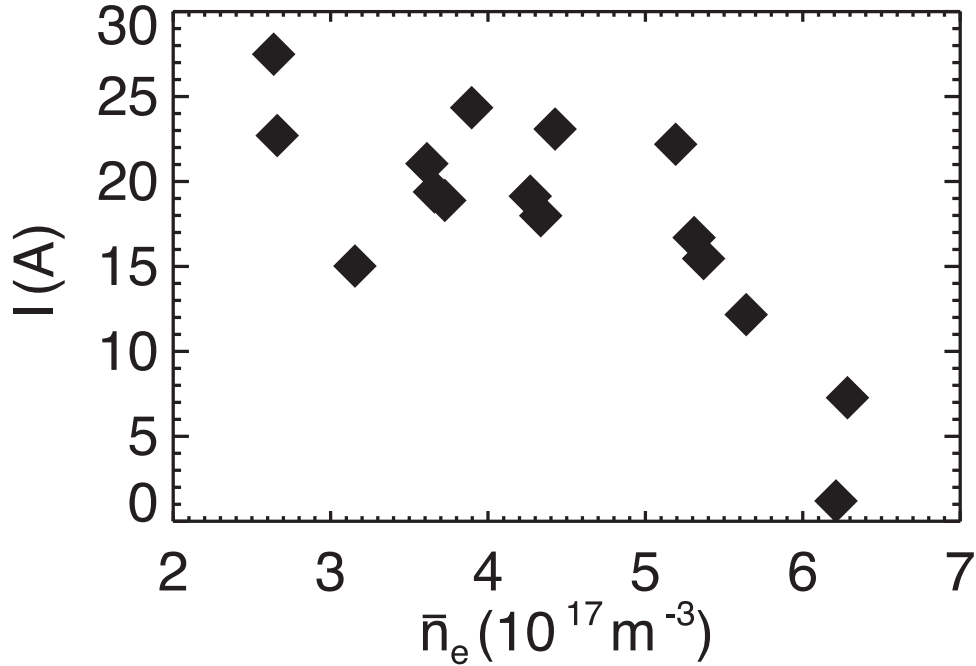


Figure 6.15: Toroidal net current as a function of the line averaged density. The current was obtained with an external Rogowski coil during a series of non-resonant helium discharges. (Adapted from Ref. [176].)

explain. A preferential direction is possible due to the complicated geometry of the plasma in front of the 2.45 GHz antenna and the wide angular spectrum of the antenna itself. As compared with the low-field case, in the high-field case the plasma volume enclosed by cutoffs is larger. Hence, the microwave can only propagate in the remaining small region between plasma boundary and vacuum vessel wall. In this region, the microwave can be in principle absorbed by a high-energy superthermal electron population, similar to experiments on the TJ-IU [177]. This absorption could then result in a toroidal net current [178]. These high fields can accelerate electrons to high energies which could be responsible for the toroidal net current. In a first series of experiments, it was found that the toroidal current breaks down as soon as a Langmuir probe approaches the positions of the cutoffs. This finding is in agreement with the hypothesis that the current is generated at the plasma boundary.

6.2.5 Discussion of possible heating mechanisms

In Sec. 6.2.1 it was shown that it is possible to sustain a discharge at high magnetic field with 2.45 GHz only, for which there are no resonances in the vacuum vessel. A minimum line averaged density close to the O-mode cutoff density was found to be necessary to start this discharge. If the line averaged density approaches the L-cutoff density, another pronounced density increase is observed. Since the interferometer

density values correspond to line averaged densities, the peak density in the plasma center is about a factor of 2 higher. Therefore, the respective positions of the two cutoffs are located at the plasma boundary. This dependence on the density points to a possible heating mechanism: As soon as the plasma density exceeds the densities of the O- and X-mode cutoff, the injected microwave can no longer propagate across the full poloidal cross section. It is guided in the coaxial volume between cutoff and vessel wall around the torus. In this resonator geometry, high wave electric fields are possible in which efficient heating and plasma generation can occur. This assumption is supported by the fact that the power deposition profile, obtained from fast power modulation experiments, was found to be peaked at the plasma boundary.

Only in the non-resonant regime, a toroidal net current of the order of 20 A and a small amount of ionizing radiation with energies of about 10 keV were found. The X-rays are likely to be generated by a fraction of high energy electrons. These electrons could be responsible for at least a fraction of the toroidal current by direct acceleration of a small percentage of the electrons to high energies by the incident microwave.

To clarify the physics behind the non-resonant heating regime, information on the X-ray spectrum seems to be mandatory. The hardware necessary to obtain these data is planned to be available at TJ-K around autumn 2010.

Chapter 7

Summary

The objective of this thesis was to study the physics of microwave heating of a plasma confined in a toroidal magnetic field like the one in the stellarator TJ-K. Three different heating scenarios can be distinguished: (i) resonant heating at low and (ii) high magnetic field with microwaves at 2.45 and 8 GHz, respectively, and (iii) non-resonant heating with 2.45 GHz at the high magnetic field.

To better understand the interaction of the microwave with the plasma, the full-wave code IPF-FDMC has been developed. A ray tracing code cannot be applied here, since the geometrical optics assumption breaks down when the wavelength of the microwave is comparable to the size of the plasma as is the case for TJ-K. The code IPF-FDMC is capable of resolving both the mode conversion processes of an O-mode into an X-mode and of an X-mode into an electrostatic electron Bernstein wave (EBW). New insights have been gained by treating these processes with the code. The temporal and spatial development of the intricate conversion processes were visualized in great detail. Thus, it could be demonstrated that the mode conversion process and the concomitant transfer of wave energy require both a finite spatial width and a finite time interval. For the X-B conversion, the necessary time to develop was found to be several hundreds of oscillation periods. The electrostatic nature of the EBW was also illustrated with the code.

The EBW is of great importance for the heating of overdense plasmas, since it can propagate beyond the cutoffs of the electromagnetic waves and can be efficiently absorbed at the electron cyclotron resonance near the plasma center. Simulations of the O-X-B mode conversion heating scenario were carried out not only for TJ-K, but also for the TJ-II stellarator in Madrid and for the RFX-mod reversed field pinch in Padua. Parameter scans were performed for these devices in order to find the configuration for maximum mode conversion efficiency, underlining the fact that the code is able to contribute to the optimization of heating in large fusion devices.

For scenario (i) in TJ-K, resonant heating with 2.45 GHz at low magnetic field, the plasma breakdown was measured with a multiple Langmuir probe array and it was found to take place at the electron cyclotron resonance layer. However, due to the low electron temperatures, the absorption is insufficient to provide effective

plasma heating. As the plasma density increases, the absorption is found at the upper-hybrid resonance (UHR) layer. Centrally peaked density profiles and hollow electron temperatures profiles are achieved with values in the range of $n_e \leq 7 \cdot 10^{17} \text{ m}^{-3}$ and $T_e \leq 20 \text{ eV}$, respectively. The shape of the temperature profiles is consistent with heating at the UHR, located near the plasma boundary.

In order to obtain the heating efficiency, a global particle and power balance analysis was carried out. Discharges at higher densities were found to be less efficiently heated than those at low density. This further confirms the UHR as being responsible for plasma heating: with increasing density the resonance moves further outwards into regions of open magnetic field lines. In this case, heating becomes less efficient because due to fast transport parallel to the magnetic field lines, a fraction of the power is lost directly to the vacuum vessel.

With the full-wave code, the importance of the vacuum vessel geometry for obtaining efficient microwave absorption was demonstrated for the first time: The inclusion of the vessel walls leads to a considerable increase in power absorption from 12 to 80 %. The increase is due to multiple reflections of the microwave between the vessel wall and the plasma boundary, which results in multiple traverses of the microwave across the UHR. An enhancement in the wave electric field was found around the UHR in the simulations and was experimentally confirmed by measurements with a monopole antenna. Power modulation experiments further localized the UHR as the position where heating takes place.

During the investigation of the heating process, a significant phenomenon was found, namely a parametric decay instability, indicating that part of the incident wave decays at the UHR. This results in broad spectra around the heating frequency and in the low-frequency region of the decay wave. Possible candidates involved in the three-wave coupling process are the upper-hybrid wave and the lower-hybrid or ion acoustic wave, which can both contribute to ion heating.

In the heating scenario (ii), resonant heating with 8 GHz at high magnetic field, a phased array antenna was used to sweep the injection angle of the microwave beam by varying its frequency. The intention of this setup was to directly influence the O–X conversion efficiency, since this process is predicted to depend strongly on the angle between the wave vector and the magnetic field. However, no noticeable effect was observed. Two reasons can be responsible for this result: *First*, the antenna emits a Gaussian beam with a relatively small beam waist. If the beam is not absorbed (or reflected) directly at the first encounter with the conversion layer, the small size of the waist results in a strong divergence at subsequent encounters. *Second*, the low density implies a low single pass absorption and a resulting spread of the microwave power. After a few reflections between the plasma and the vessel wall it will not be possible to distinguish between the wave field for oblique and perpendicular incidence. With the full-wave code, a single pass conversion efficiency of 17 % was found for injection at the optimum angle. Such an efficiency of a few percent is too small to be clearly identified in the experiment. An improvement of the conditions for O–X–B mode conversion requires higher plasma density. This

should be possible with a microwave source with higher power expected to operate in summer 2010.

Scenario (iii) describes the non-resonant heating found at high magnetic field when the microwave at 2.45 GHz is injected into the plasma. A threshold value of the density above the cutoff density of the microwave was shown to be necessary to start non-resonant heating. Furthermore, a critical value of B_0 exists below which the plasma cannot be sustained. This effect is interpreted as being connected with the so-called R-cutoff which, for decreasing magnetic field, moves from outside the vacuum vessel to a position directly in front of the microwave antenna.

Only in the non-resonant discharges, ionizing radiation with an energy in the range above 10 keV was found. Toroidal net currents of up to 20 A were measured, which are more than one order of magnitude higher than in the other scenarios. A small fraction of energetic electrons would be able to generate the X-rays and carry the plasma current. The question of the physical mechanism producing the fast electrons remains for future studies.

During power modulation experiments the power deposition was found to be located around the L-cutoff, situated at the plasma boundary. A possible explanation of the heating mechanism is the propagation of the incident microwave in an annular region: As compared to the other scenarios, here, the plasma volume enclosed by cutoffs is larger. The plasma is completely shielded by cutoffs which prevents the 2.45 GHz from penetrating into the plasma core. Hence, the wave can only exist in the small layer between the plasma boundary and the vacuum vessel wall. This geometry constitutes a coaxial resonator for the microwave in which high wave electric fields can build up. Thus, plasma heating must take place in this annular region, confirmed by the power modulation experiments.

Summarizing, with the full-wave code IPF-FDMC, a powerful tool has been developed that is capable of simulating and optimizing heating scenarios in small and large devices for fusion research. In TJ-K, heating of overdense plasmas at low magnetic field was found to take place at the upper-hybrid resonance, accompanied by a parametric decay instability. Efficient heating in this scenario was explained by the inclusion of the vacuum vessel which leads to multiple reflections and, hence, traverses across the UHR. No clear evidence for heating by the EBW was found. At the high magnetic field, the main part of the injected power is again dissipated around the UHR. A new operational regime was discovered, whose heating mechanism is at present not fully understood. The outstanding property of this regime is efficient heating in the absence of any resonance. Since no upper limit for the magnetic field strength was found, it needs to be investigated, if this scenario can be applied to large fusion devices.

Appendix A

The 8 GHz microwave system

A.1 The different operational modes

Figure A.1 illustrates the configuration of the different operational modes of the 8 GHz heating system. They are set by appropriate switching of the waveguide switches (labeled as $S1$, $S2$, $S3$). In Fig. A.1a, only TWT-A #1 is operated, whereas in the operation mode illustrated in Fig. A.1b, TWT-A #2 is operated, only. In both modes, the maximum output power is limited to 600 W, respectively. The setup for combined operation is shown in Fig. A.1c. The output of both TWT-A is combined by a magic tee [179]. Phase matching must be ensured by using a phase shifter on the low-power side (before the microwave is amplified by the TWT-A) to minimize the power going through the exit on the left-hand side of the magic tee. This arm is the so-called *E-arm*, into which power is coupled only, if the two incoming signals are not in phase. If they are in phase, all power is coupled to the so-called *H-arm*, which is the exit on the right-hand side in the block diagram. The power coupling to the E-arm is monitored on the front panel of the 8 GHz heating system at a display labeled as *balance*, the power coupling to the H-arm and, hence, the power incident into TJ-K is monitored at a display labeled as *power meter*.

The path of the propagating wave is marked by a thick yellow line in each of the plots. At the connector *sample out*, the ingoing power is monitored with a diode (hp 420A crystal detector) and acquired via the default data acquisition system, called *tjk-monitor*. The output of the diode as function of the input power is shown in Fig. A.2 for the case without and with an additional attenuator at the input. The reflected power is monitored with a power meter (hp 435B Power Meter) connected to the appropriate directional coupler.

A.2 The vacuum window

In Fig. 6.9, full-wave calculations for the 8 GHz heating scenario were presented. The vacuum window, acting as focussing lens for the microwave beam, was also

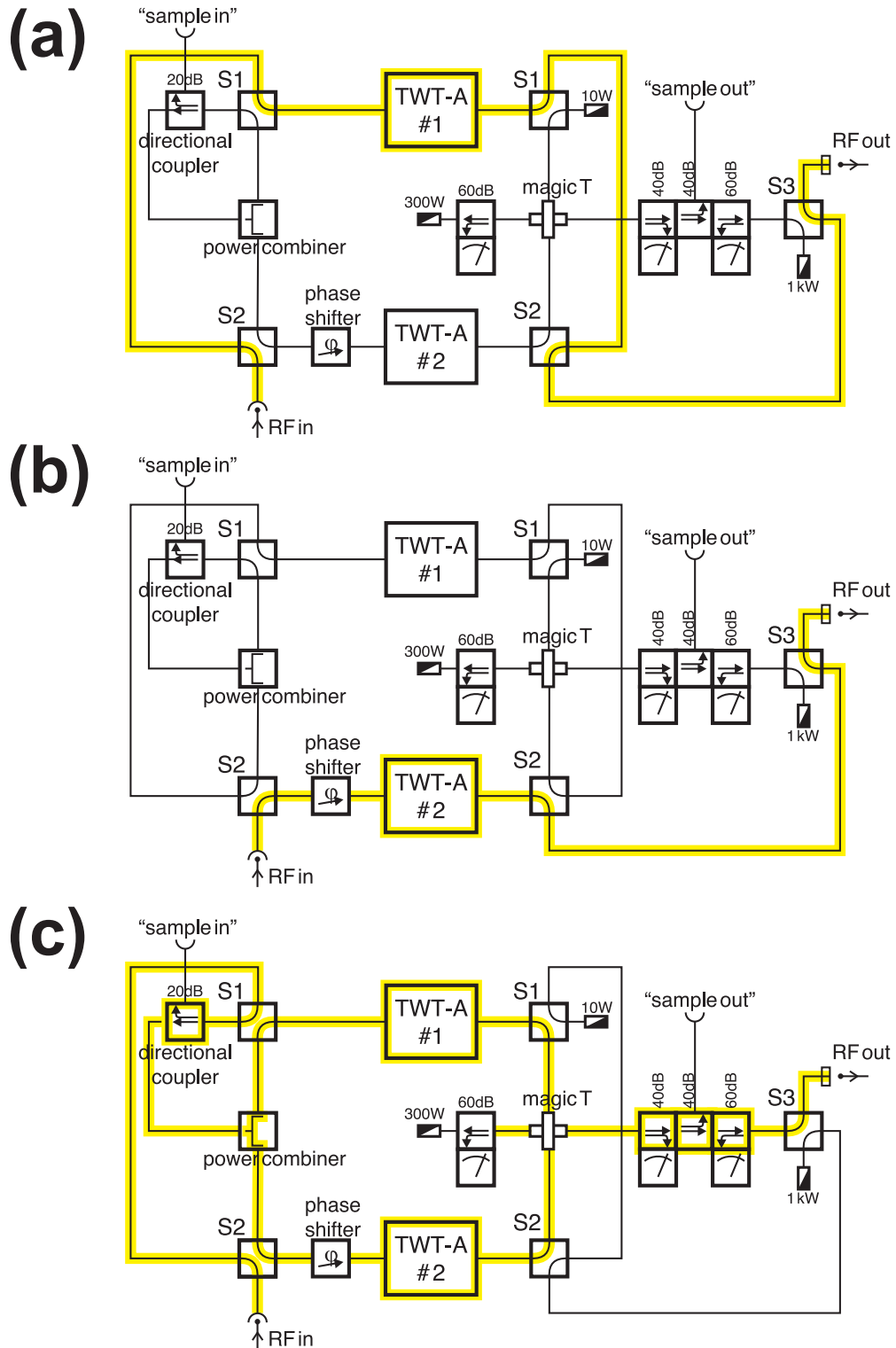


Figure A.1: Block diagram of the 8 GHz heating system. The different modes of operation are illustrated: (a) Traveling wave tube amplifier (TWT-A) #1 is used only, (b) TWT-A #2 is used only, (c) TWT-A #1 and #2 are used both.

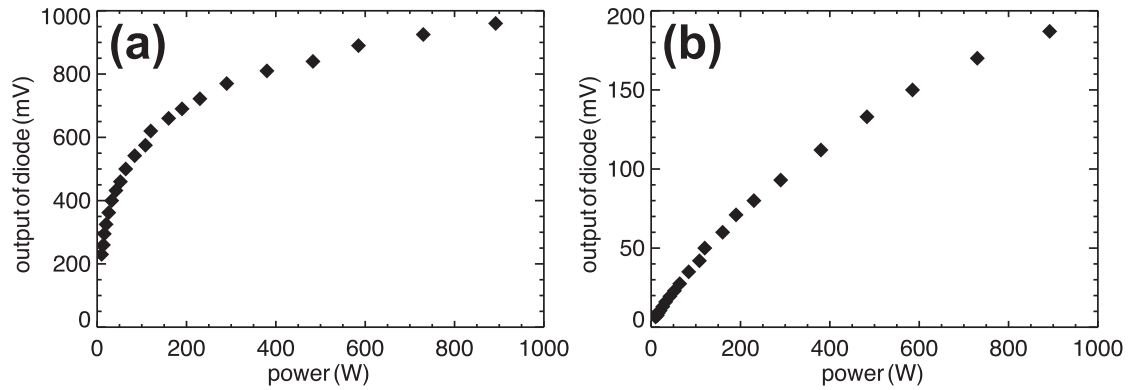


Figure A.2: Calibration measurement of the diode connected to sample out (see Fig. A.1) and used as default power monitor. (a) Direct connected to the directional coupler and (b) with an additional 20 dB attenuator at the input.

included in the calculations. This is realized by including it as a dielectric with $\epsilon_r = 2.56$. No absorption for the dielectric is included, which is justified by the negligible losses of electromagnetic waves at 2.45 GHz in plexiglas.

A complicated interference pattern of the wave electric field was found in Fig. 6.9, not only in the interaction region of the wave with the plasma, but also in the microwave lens. Figure A.3 shows the same calculations, but for propagation in vacuum, i. e. the density and the background magnetic field were both set to zero here. Especially for the case with the vacuum vessel included, one can see that the resulting wave pattern is quite complicated, even in the absence of plasma.

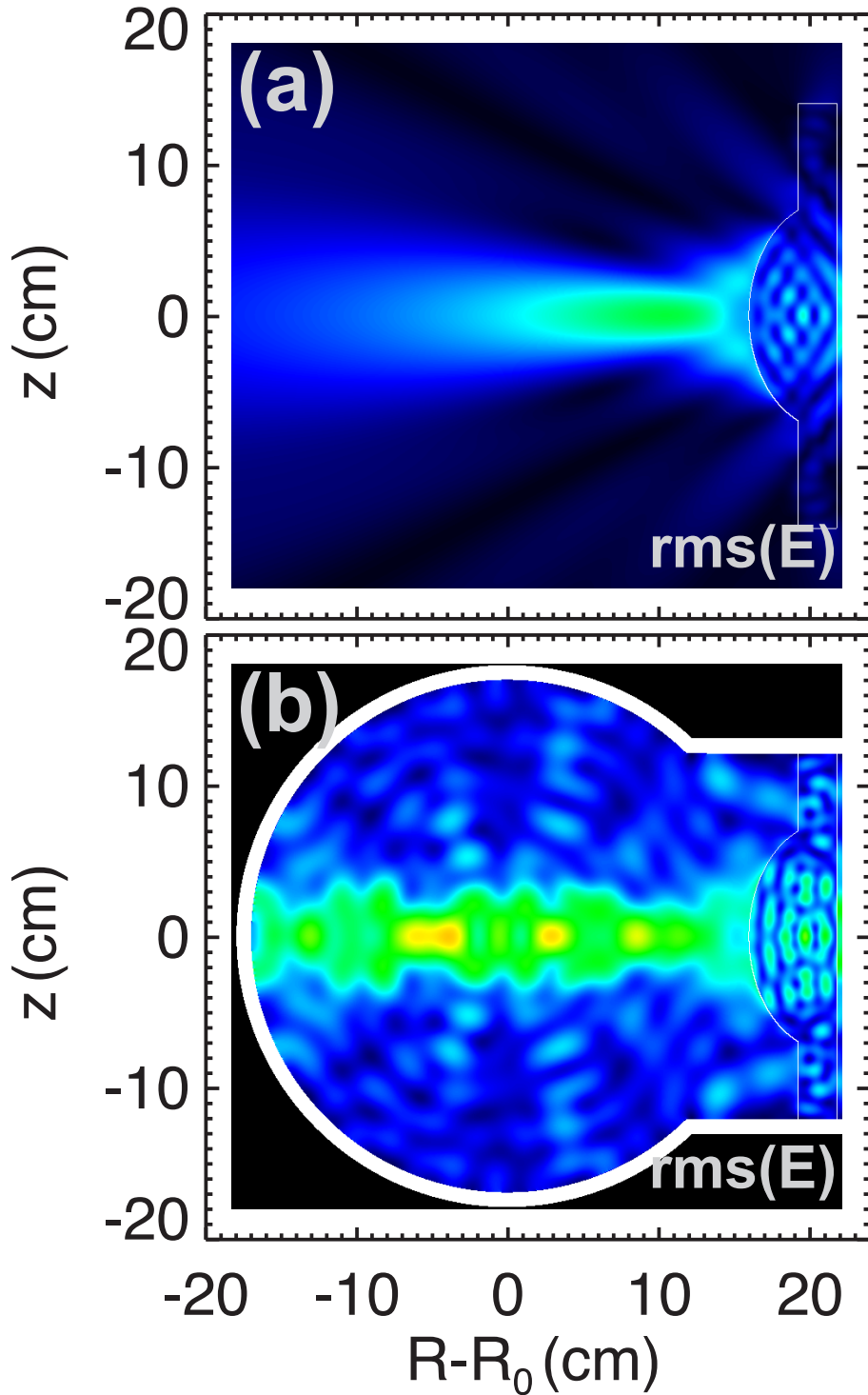









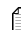








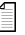


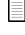














Figure A.3: Simulation of the 8 GHz heating scenario in the poloidal cross section where the array antenna is located, when injecting the beam into vacuum with no plasma and no background magnetic field. Shown is the rms-value of the wave electric field for (a) the case without and (b) with the vacuum vessel walls of TJ-K included in the calculation.





Bibliography












- [1] J. D. Cobine and D. A. Wilbur, *J. Appl. Phys.* **22**, 835 (1951). 
- [2] M. Bornatici, R. Cano, O. De Barbieri, and F. Engelmann, *Nucl. Fusion* **23**, 1153 (1983).
- [3] *Microwave Excited Plasmas*, edited by M. Moisan and J. Pelletier (Elsevier Science, Amsterdam, 1992).
- [4] J. Wesson, *Tokamaks* (Oxford University Press, New York, 1987).
- [5] L. Spitzer, *Phys. Fluids* **1**, 253 (1958). 
- [6] V. Erckmann and U. Gasparino, *Plasma Phys. Control. Fusion* **36**, 1869 (1994). 
- [7] R. Prater, *Phys. Plasmas* **11**, 2349 (2004). 
- [8] K. Sakamoto *et al.*, *Nature Phys.* **3**, 411 (2007). 
- [9] M. Shimada *et al.*, *Nucl. Fusion* **47**, S1 (2007). 
- [10] V. Erckmann *et al.*, *Fusion Science and Technology* **52**, 291 (2007).
- [11] N. Krause *et al.*, *Rev. Sci. Instrum.* **73**, 3474 (2002). 
- [12] U. Stroth *et al.*, *Phys. Plasmas* **11**, 2558 (2004). 
- [13] M. Ramisch *et al.*, *Phys. Plasmas* **12**, 032504 (2005). 
- [14] T. Happel *et al.*, *Phys. Rev. Lett.* **102**, 255001 (2009). 
- [15] P. Manz, M. Ramisch, and U. Stroth, *Phys. Rev. Lett.* **103**, 165004 (2009). 
- [16] H. P. Laqua, *Plasma Phys. Control. Fusion* **49**, R1 (2007). 
- [17] H. Barkhausen, *Phys. Z.* **20**, 401 (1919).
- [18] D. R. Hartree, *Mathematical Proceedings of the Cambridge Philosophical Society* **27**, 143 (1931). 














- [19] E. V. Appleton, J. Inst. Elec. Engrs. **71**, 642 (1932).
- [20] L. R. O. Storey, Phil. Trans. R. Soc. Lond. A **246**, 113 (1953). 
- [21] T. H. Stix, *The Theory of Plasma Waves* (McGRAW-HILL, New York, 1962).
- [22] T. H. Stix, *Waves in plasmas* (American Institute of Physics, New York, 1992).
- [23] W. P. Allis, S. J. Buchsbaum, and A. Bers, *Waves in Anisotropic Plasmas* (M.I.T. Press, Cambridge, 1963).
- [24] E. Åström, Arkiv Fysik **2**, 443 (1951).
- [25] I. B. Bernstein, Phys. Rev. **109**, 10 (1958). 
- [26] F. W. Crawford, G. S. Kino, and H. H. Weiss, Phys. Rev. Lett. **13**, 229 (1964). 
- [27] J. Preinhaelter and V. Kopecký, J. Plasma Phys. **10**, 1 (1973).
- [28] H. P. Laqua *et al.*, Phys. Rev. Lett. **78**, 3467 (1997). 
- [29] H. P. Laqua, H. J. Hartfuß, and W7-AS Team, Phys. Rev. Lett. **81**, 2060 (1998). 
- [30] N. Meyer-Vernet, S. Hoang, and M. Moncuquet, J. Geophys. Res. **98**, 163 (1993). 
- [31] F. W. Crawford, R. S. Harp, and T. D. Mantei, J. Geophys. Res. **72**, 57 (1967). 
- [32] F. F. Chen, *Introduction to Plasma Physics and Controlled Fusion, Volume 1: Plasma Physics* (Plenum Press, New York, 1984).
- [33] I. N. Bronstein, K. A. Semendjajew, G. Musiol, and H. Mühlig, *Taschenbuch der Mathematik* (Verlag Harri Deutsch, Frankfurt am Main, 2000).
- [34] F. Volpe, Ph.D. thesis, Ernst-Moritz-Arndt-Universität Greifswald, Greifswald, 2003. 
- [35] S. Puri, F. Leuterer, and M. Tutter, J. Plasma Phys. **9**, 89 (1973). 
- [36] A. Mueck *et al.*, Phys. Rev. Lett. **98**, 175004 (2007). 
- [37] H. Weitzner and D. B. Batchelor, Phys. Fluids **22**, 1355 (1979). 
- [38] F. R. Hansen, J. P. Lynov, and P. Michelsen, Plasma Phys. Control. Fusion **27**, 1077 (1985). 
- [39] E. Mjølhus, J. Plasma Phys. **30**, 179 (1983). 












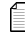
- [40] F. R. Hansen, J. P. Lynov, C. Maroli, and V. Petrillo, *J. Plasma Phys.* **39**, 319 (1988). [↗](#)
- [41] H. Igami, H. Tanaka, and T. Maekawa, *Plasma Phys. Control. Fusion* **48**, 573 (2006). [↗](#)
- [42] K. G. Budden, *Radio Waves in the Ionosphere* (Cambridge University Press, Cambridge, 1961).
- [43] A. K. Ram and S. D. Schultz, *Phys. Plasmas* **7**, 4084 (2000). [↗](#)
- [44] A. Köhn *et al.*, *Plasma Phys. Control. Fusion* **50**, 085018 (2008). [↗](#)
- [45] R. Bilato *et al.*, *Nucl. Fusion* **49**, 075020 (2009). [↗](#)
- [46] P. M. Bellan, *Fundamentals of Plasma Physics* (Cambridge University Press, Cambridge, 2006).
- [47] T. J. M. Boyd and J. J. Sanderson, *The Physics of Plasmas* (Cambridge University Press, Cambridge, 2003).
- [48] A. Taflov and H. S. C., *Computational Electrodynamics: the Finite-Difference Time-Domain Method* (Artech House Publishers, Boston, 2000).
- [49] K. S. Yee, *IEEE Trans. on Antennas and Propagation* **14**, 302 (1966). [↗](#)
- [50] K. L. Shlager and J. B. Schneider, *IEEE Antennas and Propagation Magazine* **37**, 39 (1995). [↗](#)
- [51] J. H. Irby, S. Horne, I. H. Hutchinson, and P. C. Stek, *Plasma Phys. Control. Fusion* **35**, 601 (1993). [↗](#)
- [52] J. L. Young, *Radio Science* **29**, 1513 (1994).
- [53] E. Holzhauer and E. Blanco, *Nucl. Fusion* **46**, S824 (2006). [↗](#)
- [54] J. Schirmer *et al.*, *Plasma Phys. Control. Fusion* **49**, 1019 (2007). [↗](#)
- [55] Y. Lin *et al.*, *Rev. Sci. Instrum.* **72**, 344 (2001). [↗](#)
- [56] M. Ignatenko *et al.*, *Nucl. Fusion* **46**, S760 (2006). [↗](#)
- [57] I. H. Hutchinson, *Principles of plasma diagnostics* (Cambridge University Press, Cambridge, 1987), p. 50.
- [58] J.-P. Berenger, *Journal of Computational Physics* **114**, 185 (1994). [↗](#)
- [59] W. C. Chew and W. H. Weedon, *Microwave Opt. Tech. Lett.* **7**, 599 (1994). [↗](#)
















- [60] N. A. Gondarenko, P. N. Guzdar, S. L. Ossakow, and P. A. Bernhardt, *Journal of Computational Physics* **194**, 481 (2004). 
- [61] R. Chandra *et al.*, *Parallel Programming in OpenMP* (Morgan Kaufmann Publishers, San Francisco, 2001).
- [62] B. Chapman, G. Jost, and R. v. d. Pas, *Using OpenMP: Portable Shared Memory Parallel Programming (Scientific and Engineering Computation)* (MIT Press, Cambridge, 2008).
- [63] A. Taflove, *Wave Motion* **10**, 547 (1988). 
- [64] A. Taflove and M. E. Brodwin, *IEEE Trans. Microwave Theory Tech.* **MTT-23**, 623 (1975).
- [65] M. Brambilla, *Plasma Phys. Control. Fusion* **31**, 723 (1989). 
- [66] A. K. Ram, A. Bers, S. D. Schultz, and V. Fuchs, *Phys. Plasmas* **3**, 1976 (1996). 
- [67] C. Lechte, *IEEE Trans. Plasma Sci.* **37**, 1099 (2009). 
- [68] C. Alejaldre *et al.*, *Fusion Technology* **17**, 131 (1990).
- [69] H. Igami, M. Uchida, H. Tanaka, and T. Maekawa, *Plasma Phys. Control. Fusion* **46**, 261 (2004). 
- [70] V. L. Ginzburg, in *Propagation of Electromagnetic Waves in Plasmas*, edited by W. L. Sadowski and D. M. Gallik (Gordon and Breach, Science Publishers, Inc., New York, 1961).
- [71] A. E. Siegman, *An Introduction to Lasers and Masers* (McGRAW-HILL, New York, 1971).
- [72] A. Köhn, E. Holzhauser, and U. Stroth, *IEEE Trans. Plasma Sci.* **36**, 1220 (2008). 
- [73] A. Köhn *et al.*, in *RADIO FREQUENCY POWER IN PLASMAS: Proceedings of the 18th Topical Conference* (AIP Conf. Proc., Ghent, 2009), p. 469. 
- [74] C. Alejaldre *et al.*, *Plasma Physics and Controlled Fusion Research (Proc. 14th IAEA Int. Conf., Würzburg, 1992)*, IAEA, Vienna (IAEA, Vienna, 1992), p. 665.
- [75] E. Ascasíbar *et al.*, *Plasma Physics and Controlled Fusion Research (Proc. 15th IAEA Int. Conf., Seville, 1994)*, IAEA, Vienna (IAEA, Vienna, 1994), p. 749.





- [76] E. Ascasíbar *et al.*, Fusion Technology **27**, 198 (1995).
- [77] E. Ascasíbar *et al.*, Nucl. Fusion **37**, 851 (1997). 
- [78] T. C. Luce, C. C. Petty, and J. G. Cordey, Plasma Phys. Control. Fusion **50**, 043001 (2008). 
- [79] C. C. Petty, Phys. Plasmas **15**, 080501 (2008). 
- [80] C. Alejaldre *et al.*, Technical report, Madrid (unpublished).
- [81] C. Gourdon, *Programme optimisé de calculs numérique dans les configurations magnétique toroidales* (CEN, Fontenay aux Roses, 1970).
- [82] R. Westphal, Diploma thesis, Christian-Albrechts-Universität, Kiel, 2001.
- [83] P. Abdul, Master's thesis, Institut für Plasmaforschung der Universität Stuttgart, Stuttgart, 2009.
- [84] E. Pehl, *Mikrowellentechnik. Band 2: Antennen und aktive Bauteile* (Dr. Alfred Hüthig Verlag, Heidelberg, 1984).
- [85] H.-G. Unger, *Hochfrequenztechnik in Funk und Radar* (Teubner, Stuttgart, 1984).
- [86] A. J. Baden Fuller, *Mikrowellen. Lehrbuch für Studenten der Elektrotechnik und Physik höherer Semester.* (Vieweg, Braunschweig, 1974).
- [87] *Taschenbuch der Hochfrequenztechnik*, edited by H. H. Meinke and F.-W. Gundlach (Springer-Verlag, Berlin, 1986).
- [88] H. Höhnle, Diploma thesis, Institut für Plasmaforschung der Universität Stuttgart, Stuttgart, 2008.
- [89] A. Köhn *et al.*, in *PLASMA 2007: The International Conference on Research and Application of Plasmas* (AIP Conf. Proc., Greifswald, 2008), p. 43. 
- [90] *Microwave Antenna Theory and Design*, edited by S. Silver and H.-M. James (Peter Peregrinus Ltd, London, 1984).
- [91] J. Brown, in *Microwave Lenses*, edited by B. L. Worsnop (Methuen & Co. Ltd., London, 1953).
- [92] S. B. Cohn, in *Antenna Engineering Handbook*, edited by H. Jasik (McGraw-Hill, New York, 1961).
- [93] B. Carlowitz, *Kunststofftabellen* (Carl Hanser Verlag München Wien, München, 1995).

- [94] M. I. Petelin and W. Kasparek, *Int. Journal of Electronics* **71**, 871 (1991). 
- [95] I. Langmuir, *Science* **58**, 290 (1923). 
- [96] H. M. Mott-Smith and I. Langmuir, *Phys. Rev.* **28**, 727 (1926). 
- [97] F. F. Chen, in *Plasma Diagnostic Techniques*, edited by R. H. Huddleston and S. L. Leonard (Academic Press Inc., New York, 1965), Chap. 4, p. 113.
- [98] S. Pfau and M. Tichý, in *Low Temperature Plasmas - Volume 1*, edited by R. Hippler, H. Kersten, M. Schmidt, and K. H. Schoenbach (WILEY -VCH, Weinheim, 2008), p. 175.
- [99] M. Ramisch, Ph.D. thesis, Christian-Albrechts-Universität, Kiel, 2005. 
- [100] J. E. Allen, *Physica Scripta* **45**, 497 (1992). 
- [101] J. G. Laframboise, *Theory of Spherical and Cylindrical Langmuir Probes in a Collisionless Plasma*, 1966.
- [102] U. Stroth, *Einführung in die Plasmaphysik, Vorlesungsskript* (Institut für Plasmaforschung, Universität Stuttgart, Stuttgart, 2007).
- [103] T. Happel, Diploma thesis, Christian-Albrechts-Universität, Kiel, 2005.
- [104] W. H. Press, B. P. Flannery, S. A. Teukolsky, and W. T. Vetterling, *Numerical Recipes* (Cambridge University Press, Cambridge, 1992).
- [105] G. Janzen, *Kurze Antennen* (Franckh'sche Verlagshandlung, Stuttgart, 1986).
- [106] G. Janzen, *Monopolantennen und Vertikalantennen* (G. Janzen, Kempten, 1999).
- [107] U. T. Wolters, Ph.D. thesis, Ruhr-Universität Bochum, Bochum, 2001. 
- [108] V. K. Yadav and D. Bora, *Phys. Plasmas* **11**, 3409 (2004). 
- [109] J. Stöber, Diploma thesis, Christian-Albrechts-Universität, Kiel, 2001.
- [110] R. A. Stern and J. A. Johnson, *Phys. Rev. Lett.* **34**, 1548 (1975). 
- [111] S. Enge *et al.*, in *Proceedings of the 14th International Congress on Plasma Physics (ICPP2008)* (J. Plasma Fusion Res. SERIES, Fukuoka, 2009), p. 928. 
- [112] S. Enge *et al.*, in *49th Annual Meeting of the Division of Plasma Physics* (APS physics, Orlando, Florida, 2007), Vol. 52. 
- [113] S. Enge *et al.*, in *36th EPS Conference on Plasma Phys.* (ECA 33E, P-5.145, Sofia, 2009). 

- [114] S. Klenge, Diploma thesis, Institut für Plasmaforschung der Universität Stuttgart, Stuttgart, 1998.
- [115] G. Birkenmeier *et al.*, IEEE Trans. Plasma Sci. **36**, 1092 (2008). 
- [116] G. Birkenmeier, Diploma thesis, Institut für Plasmaforschung der Universität Stuttgart, Stuttgart, 2008.
- [117] S.-I. Itoh, J. Phys. Soc. Jpn. **59**, 3431 (1990). 
- [118] A. A. Ware, Phys. Rev. Lett. **25**, 916 (1970). 
- [119] K. Rahbarnia, Diploma thesis, Christian-Albrechts-Universität, Kiel, 2003.
- [120] S. J. Diem *et al.*, Phys. Rev. Lett. **103**, 015002 (2009). 
- [121] A. Köhn, Diploma thesis, Christian-Albrechts-Universität, Kiel, 2005.
- [122] C. Lechte, J. Stöber, and U. Stroth, Phys. Plasmas **9**, 2839 (2002). 
- [123] A. Köhn *et al.*, Plasma Phys. Control. Fusion **52**, 035003 (2010). 
- [124] *Annual Report 2009*, edited by B. Plaum and U. Stroth (Institut für Plasmaforschung, Universität Stuttgart, Stuttgart, 2009), p. 14. 
- [125] D. G. Swanson, *Theory of mode conversion and tunneling in inhomogeneous plasmas* (John Wiley & Sons, INC., New York, 1998).
- [126] M. Dressel, O. Klein, D. S., and G. Grüner, Ferroelectrics **176**, 285 (1996). 
- [127] J.-Y. Hsu and C. P. Moeller, in *Proc. of the 7th Topical Conference on Applications of Radio-Frequency Power to Plasmas, Kissimmee, Florida* (AIP Conf. Proc., New York, 1987), p. 13.
- [128] R. I. Pinsker *et al.*, Plasma Phys. Control. Fusion **47**, 335 (2004). 
- [129] R. B. White and F. F. Chen, Plasma Phys. **16**, 565 (1974). 
- [130] Y. Y. Podoba *et al.*, Phys. Rev. Lett. **98**, 255003 (2007). 
- [131] R. Ikeda *et al.*, Phys. Plasmas **15**, 072505 (2008). 
- [132] A. T. Lin and C.-C. Lin, Phys. Rev. Lett. **47**, 98 (1981). 
- [133] V. A. Flyagin, A. V. Gaponov, M. I. Petelin, and V. K. Yulpatov, IEEE Trans. Microwave Theory Tech. **MTT-25**, 514 (1977).
- [134] M. Porkoláb, Nucl. Fusion **12**, 329 (1972).

- [135] M. Porkoláb, V. Arunasalam, N. C. Luhmann, and J. P. M. Schmitt, *Nucl. Fusion* **16**, 269 (1976).
- [136] K. H. Spatschek, *Fortschritte der Physik* **24**, 687 (1976). 
- [137] W. L. Kruer, *The physics of laser plasma interactions* (Addison-Wesley Publishing Co., United States, 1988).
- [138] J. Nuckolls, L. Wood, A. Thiessen, and G. Zimmerman, *Nature* **239**, 139 (1972). 
- [139] H. L. Zhou, J. Huang, and S. P. Kuo, *Phys. Plasmas* **1**, 3044 (1994).
- [140] A. V. Gurevich, H. Carlson, A. V. Lukyanov, and K. P. Zybin, *Phys. Lett. A* **231**, 97 (1997). 
- [141] M. Porkoláb, *Phys. Fluids* **17**, 1432 (1974). 
- [142] S. C. Sharma, *J. Plasma Physics* **58**, 277 (1997). 
- [143] K. Baumgärtel, *Contr. to Plasma Physics* **17**, 187 (1977). 
- [144] R. P. H. Chang, M. Porkoláb, and B. Grek, *Phys. Rev. Lett.* **28**, 206 (1972). 
- [145] B. Grek and M. Porkoláb, *Phys. Rev. Lett.* **30**, 836 (1973). 
- [146] E. Albers, K. Krause, and H. Schlüter, *Plasma Physics* **20**, 361 (1978). 
- [147] F. S. McDermott *et al.*, *Phys. Fluids* **25**, 1488 (1982). 
- [148] V. Erckmann *et al.*, *Plasma Physics and Controlled Fusion Research (Proc. 10th IAEA Int. Conf., London, 1984)*, IAEA, Vienna (IAEA, Vienna, 1985), p. 419.
- [149] C. Labaune *et al.*, *Eur. Phys. J. D* **44**, 283 (2007). 
- [150] R. Cesario *et al.*, in *35th EPS Conference on Plasma Phys.* (ECA 32D, P-2.106, Hersonissos, 2008). 
- [151] J. O. Hall, G. Stenberg, A. I. Eriksson, and M. André, *Annales Geophysicae* **27**, 1027 (2009).
- [152] V. Damgov, in *Nonlinear and parametric phenomena: Theory and applications in radiophysical and mechanical systems*, edited by L. O. Chua (World Scientific Publishing Co. Pte. Ltd., Singapore, 2004).
- [153] P. K. Kaw, W. L. Kruer, C. S. Liu, and K. Nishikawa, in *Advances in Plasma Physics Volume 6*, edited by A. Simon and W. B. Thompson (Interscience, New York, 1976).

- [154] D. G. Swanson, *Plasma Waves* (Academic Press, Inc., London, 1989).
- [155] J. M. Manley and H. E. Rowe, Proc. IRE **44**, 904 (1956). 
- [156] H. E. Rowe, Proc. IRE **46**, 850 (1958). 
- [157] E. Suvorov *et al.*, Nucl. Fusion **38**, 661 (1998). 
- [158] S. Enge *et al.*, Phys. Rev. Lett. (2010), submitted.
- [159] M. Cengher, J. K. Anderson, V. Svidzinski, and C. B. Forest, Nucl. Fusion **46**, 521 (2006). 
- [160] P. Diez, Diploma thesis, Institut für Plasmaforschung der Universität Stuttgart, Stuttgart, 2009.
- [161] V. N. Budnikov, V. E. Golant, and A. A. Obuchov, Phys. Lett. A **31**, 76 (1970). 
- [162] J. Musil and F. Záček, Czech. J. Phys. **22**, 133 (1972). 
- [163] W. Staib, Ph.D. thesis, Institut für Plasmaforschung der Universität Stuttgart, Stuttgart, 1975.
- [164] G. Janzen and E. Räuchle, Phys. Lett. A **83**, 15 (1981). 
- [165] J. Musil, F. Záček, and P. Schmiedberger, Plasma Physics **16**, 735 (1974). 
- [166] H. P. Laqua *et al.*, in *RADIO FREQUENCY POWER IN PLASMAS: Proceedings of the 18th Topical Conference* (AIP Conf. Proc., Ghent, 2009), p. 441. 
- [167] H. P. Laqua *et al.*, in *36th EPS Conference on Plasma Phys.* (ECA 33E, O-4.047, Sofia, 2009). 
- [168] A. Köhn *et al.*, in *36th EPS Conference on Plasma Phys.* (ECA 33E, P-5.146, Sofia, 2009). 
- [169] V. Erckmann, U. Gasparino, and H. Maaßberg, Plasma Phys. Control. Fusion **34**, 1917 (1992). 
- [170] M. Murakami *et al.*, Phys. Rev. Lett. **66**, 707 (1991). 
- [171] J. D. Treffert and J. L. Shohet, Phys. Rev. Lett. **53**, 2409 (1984). 
- [172] B. C. Zhang, B. D. Blackwell, G. G. Borg, and V. Petrzilka, Phys. Plasmas **4**, 3986 (1997).
- [173] P. N. Murgatroyd *et al.*, Meas. Sci. Technol. **2**, 1218 (1991). 

-
- [174] S. Tumanski, *Meas. Sci. Technol.* **18**, R31 (2007). 
- [175] A. Köhn *et al.*, in *49th Annual Meeting of the Division of Plasma Physics* (APS physics, Orlando, Florida, 2007), Vol. 52. 
- [176] S. Merli *et al.*, in *DPG Frühjahrstagung der Sektion AMOP* (Deutsche Physikalische Gesellschaft e.V., Hannover, 2010).
- [177] F. Medina, L. Rodríguez-Rodrigo, M. A. Ochando, and F. Castejón, *Plasma Phys. Control. Fusion* **40**, 1897 (1998). 
- [178] N. J. Fisch and A. H. Boozer, *Phys. Rev. Lett.* **45**, 720 (1980). 
- [179] T. Moreno, *Microwave transmission design data* (Artech House, Norwood, 1989).

Danksagung

Ich möchte an dieser Stelle all denen danken, die mir während meiner Promotion auf die eine oder andere Art und Weise geholfen haben, nicht nur bei der Erstellung dieser Arbeit, sondern auch dabei die Zeit meiner Promotion interessant und unterhaltsam zu gestalten:

Prof. Dr. Ulrich Stroth für die Möglichkeit, diese Arbeit in seiner Gruppe erstellen zu können. Ich danke ihm für sein Vertrauen und seine Unterstützung während der gesamten Zeit der Promotion. Weiterhin möchte ich mich für die Möglichkeit bedanken auf zahlreichen internationalen Tagungen einen Einblick in das faszinierende Feld der Fusionsforschung zu bekommen. Ich denke, es spricht für sich, dass in seiner Arbeitsgruppe eine sehr freundschaftliche und produktive Atmosphäre herrscht.

Dr. Eberhard Holzhauer für die ausgezeichnete Betreuung und Begleitung dieser Arbeit. Er war mein erster Ansprechpartner bei Fragen aller Art. Unsere Diskussionen, die sich oft über mehrere Stunden hinzogen, waren immer sehr produktiv und anregend. Ohne ihn wäre dieser Arbeit nicht in der vorliegenden Form möglich gewesen.

Dr. Mirko Ramisch als Experimentleiter des TJ-K. Seine Routinen zur Experimentsteuerung und Datenerfassung ermöglichen einen nahezu reibungslosen Experimentieralltag. Auch danke ich ihm für die Entwicklung des Programmes MCC, ohne das die full-wave Simulationen etwas weniger experimentnah gewesen wären.

Dr. Peter Manz für die lustige gemeinsame Zeit am IPF, vor allem auf den zusammen besuchten Tagungen, deren Nächte oft herrlich kurz waren!

Sebastian Enge für die allmorgentliche Kaffee- und Gesprächsrunde und das gemeinsame Planen von FLIP-S.

Peter Diez und *Stephen Agimelen* für die zahlreichen Experimente zur nicht-resonanten Heizung, die wir zusammen geplant und durchgeführt haben. Vor allem Peter ist es zu verdanken, dass wir bei diesem Thema ein gutes Stück voran gekommen sind.

Hendrik Höhnle und *Gregor Birkenmeier* für die gemeinsamen Messkampagnen, deren Daten sich teilweise in dieser Arbeit wiederfinden. Zu dritt haben wir die nicht-resonante Heizung entdeckt, deren Untersuchung weiterhin spannend bleibt.

Bernhard Roth für seinen Einfallsreichtum beim Konstruieren diverser Gerätschaften für TJ-K und FLIP-S.

Der gesamten Arbeitsgruppe *Plasmadynamik und -diagnostik*, insbesondere noch *Bernhard Nold*, *Prof. Dr. Lars Stollenwerk*, *Stefan Merli*, *Kirsi Weber*, *Farah Aziz*, *Martin Rzittka*, *Dr. Kian Rahbarnia* und *Dr. Navid Mahdizadeh* für die nette Atmosphäre in und außerhalb des Instituts.

Dr. Walter Kasperek und *Dr. Burkhard Plaum* aus der Arbeitsgruppe *Fusionorientierte Plasmaphysik*, dafür dass sie einem Physiker immer sehr geduldig Fragen aller Art über Mikrowellenkomponenten beantwortet haben. Burkhard danke ich zusätzlich für seine C-Bibliotheken, die eine graphische Darstellung der Simula-

tionsergebnisse erheblich vereinfacht haben.

Dr. Andreas Schulz stellvertretend für die Gruppe *Plasmatechnologie* für die Bereitstellung von Hardware aller Art.

Peter Salzmann als Leiter der mechnischen Werkstatt und *Karl-Heinz Schlüter* als Leiter der E-Werkstatt für die schnelle und gewissenhafte Anfertigung von kleinen und größeren Gerätschaften aller Art.

Ingeborg Wagner und *Ruth Edelmann-Amrhein* für ihr Organisationstalent und ihre Hilfsbereitschaft.

Roland Munk dafür, dass er sich immer um das physische und psychische Wohlergehen des gesamten Instituts kümmert.

Dr. Alvaro Cappa for introducing me into the stellarator TJ-II and for all the patience he had during the time we wrote our paper about the O–X–B heating scheme at TJ-II.

Dr. Roberto Bilato and *Prof. Dr. Francesco Volpe* for giving me the possibility to contribute to the O–X–B feasibility study for the RFX-mod reversed field pinch device.

Dr. Heinrich Laqua, *Dr. Yuriy Podoba* und *Torsten Stange* vom Max-Planck-Institut für Plasmaphysik für viele spannende und anregende Diskussionen.

Meinen Eltern *Heike & Matthias Köhn*, meinen Schwestern *Vivian* and *Tanja Köhn*, meiner Oma *Melitta Lohse* für die anhaltende Unterstützung und den Rückhalt während der letzten Jahre.

Tanja Seemann, dafür dass du immer für mich da warst in den letzten Jahren. Dein Lächeln am Ende eines Tages macht alle Sorgen vergessen und macht so jeden Tag zu einem guten Tag.

Curriculum Vitae

Personal data

name	Alf Köhn
date and place of birth	29.11.1980, Preetz, Germany
family status	unmarried
nationality	German

School education

1987–1991	elementary school: Hermann-Ehlers-Schule, Preetz
1991–2000	secondary school: Friedrich-Schiller-Gymnasium, Preetz
June 2000	final exam (Abitur) with main courses mathematics and physics

Scientific education

Oct 2000–Dec 2005	study of physics at Christian-Albrechts-Universität, Kiel
Dec 2004–Dec 2005	preparation of the diploma thesis entitled <i>Mikrowellenheizung von überdichten Plasmen in TJ-K</i> in the group of Prof. Dr. U. Stroth
Jan 2006	diploma in physics
since Mar 2006	Ph. D. graduation at Universität Stuttgart with subject <i>Heating plasmas in the stellarator TJ-K</i> in the group of Prof. Dr. U. Stroth

Eidesstattliche Versicherung

Hiermit erkläre ich an Eides Statt, dass ich diese Arbeit ausschließlich unter Anleitung meiner wissenschaftlichen Lehrer und unter Verwendung der angegebenen Hilfsmittel angefertigt habe. Sie hat weder ganz noch zum Teil an einer anderen Stelle im Rahmen eines Prüfungsverfahrens vorgelegen.

Stuttgart, den

Alf Köhn